北京大学

博士研究生学位论文

题目：在CMS实验上测量粲夸克偶素产生截面的研究

姓　　名：杨宗长

学　　号：10404831

院　　系：物理学院

专　　业：粒子物理与原子核物理

研究方向：高能物理实验

导师姓名：钱思进 教授

二〇〇九年四月

版权声明

Study of a J/ψ Cross Section Measurement with Early Data at CMS

Thesis by

Zongchang Yang

School of Physics, Peking University

Peking University

Beijing, China

Thesis submitted for the degree of

doctor of philosophy

Prof. Dr. Sijin Qian (Supervisor)

Prof. Dr. Lorenzo Foa

Dr. Fabrizio Palla

April 2009

在CMS实验上测量粲夸克偶素产生截面的研究

杨宗长　粒子物理与原子核物理

导师姓名：　钱思进 教授

摘　要

在强子对撞机上重夸克偶素的产生机制仍未被很好的理解。传统的重夸克偶素的产生是建立在色单态(CSM)模型上的。然而美国费米国家实验室的质子-反质子对撞机Tevatron上的CDF实验测得的粲夸克偶素的产生截面和色单态模型的理论计算结果存在巨大差异。为此人们提出了基于非相对论量子色动力学(NRQCD)因子化的色八重态机制（COM），可以很好地解释夸克偶素的产生截面。但是，COM中预期的大横动量粲夸克偶素是横向极化的，这与CDF实验的观测结果不符合。因此，在LHC能区测量粲夸克偶素的产生截面和极化参数，可以对已有的理论模型进行检验。

LHC是建在欧洲核子中心(CERN)的对撞能量为14TeV 的世界上最大的质子-质子对撞机，其对撞能量是Tevatron的七倍，亮度高两个数量级。CMS是建造于其上的两个大型通用探测器之一，具有很好的子接受度和动量分辨率,适合通过双子衰变道研究粲夸克偶素。本论文建立了一套完整的在CMS探测器上测量粲夸克偶素的产生截面的模拟分析方法。因为粲夸克偶素的产生截面比较大，所以此研究只需要LHC运行2到3个月的数据即可初步完成，预计将是CMS实验基于真实对撞数据发表的最早的物理分析文章之一。利用B强子的飞行时间，我们可以区分prompt和non-prompt粲夸克偶素，从而分别计算两种成分的产生截面。本论文研究了在早期探测器没有很好的校准的情况下带来的影响，同时也讨论了其它所有可能的系统误差。在CMS探测器获取积分亮度为3 pb^{-1}的数据时，大约能重建

出七万个粲夸克偶素事例，可测量的横动量范围为5到40 GeV/c。测量结果的精确度大约为15%。

关键词：粲夸克偶素，产生截面，Color Singlet Model，NRQCD，Color Octet Mechanism, CMS

Study of a J/ψ Cross Section Measurement with with First Data at CMS

Zongchang Yang (High Energy Physics)

Supervised by **(Prof. Sijin Qian)**

Abstract

This thesis presents the methods and plans for measuring the differential p_T $J/\psi \rightarrow \mu^+\mu^-$ production cross section, using data to be collected in the first LHC run by the CMS detector. Making use of the large B-hadron lifetime, we show how to separate the promptly produced J/ψ's from those coming from B-hadron decays. Since the J/ψ production cross section is expected to be large, the analysis should be viable with relatively small data sets, that will become available early in the startup of the LHC. We also address effects of a non-perfect detector alignment, as well as systematic uncertainties.

About 70 thousand J/ψ decays are reconstructed for an integrated luminosity of 3 pb^{-1}in 14 TeV collisions, in the range of $p_T^{J/\psi}$ between 5 and 40 GeV/c. The precision of the result is limited by systematic uncertainties, and is at the 15 % level.

Keywords: CMS, J/ψ, cross section, NRQCD, Color Singlet Model, Color Octet Mechanism

Acknowledgments

First of all, I am most grateful to my supervisor, Prof. Sijin Qian for his guidance, support and attention to detail over the 5 years. He is remarkable in his continual patience, kind insight, and helpful suggestions in tackling problems in my research. Her enthusiasm, curiosity and suggestions in high energy research is truly inspirational.

I sincerely thank Prof. Lorenzo Foa and Dr. Fabrizio Palla, who supervised me when I studied in INFN Pisa. I would also like to thank Aafke Kraan for her great help on this topic. The $J/\psi \to \mu^+\mu^-$ analysis would not have been possible without their collaboration and help. It's fun and productive when I work with them at Pisa.

I wish to express my gratitude to Prof. Yajun Mao and Prof. Yong Ban for their many fruitful discussions, help and expertise on this analysis. I really enjoyed our group meetings hold by Prof. Yajun Mao.

Many thanks to Prof. Urs Langenegger and Prof. Jim Olsen, coordinators of the CMS B-Physics group, for the numerous discussions and their continuous support.

Thanks also should be given to Prof. Roberto Dell'Orso, Prof. Roberto Tenchini, Prof. Rino Castaldi, Franco Ligabue, Giovanni Petrucciani, Paolo Azzurri and the other members at INFN Pisa. Thank you for the healthiest of working environments.

I thank all my friends at Peking University and INFN Pisa: Lie Liu, Shuang

Guo, Zhen Hu, Yutie Liang, Bo Zhu, Ran Han and all the other HEP group members. Their friendship makes life at PKU more enjoyable.

Finally, I thank my parents and brother for their infinite patience, kindness and love during these years in everything I do, without which none of this would be possible, and to whom this thesis is dedicated.

Contents

List of Figures

List of Tables

Chapter 1

Introduction

Although the J/ψ meson has been discovered more than 30 years ago, the underlying production mechanism at hadron colliders is still not well understood. The next generation particle accelerator, the Large Hadron Collider (LHC) at CERN, will open new opportunities for quarkonia physics. The LHC is designed to collide protons with a center-of-mass energy of 14 TeV. The predicted cross section for charmonium production increases by a factor of about 100 compared to the one at the Tevatron. When the LHC starts its operation in late 2009, it will produce large number of charm quarks even in low luminosity runs during the first few years of running. The number of produced quarkonium states such as J/ψ , important for many physics studies, will also be large.

The importance of studying the decays of the charmonium to muon pair for CMS is first, being narrow resonances, they can be used as tools for alignment and calibration of the trigger, tracking and muon systems. Secondly, understanding the details of the prompt charmonium production is a challenging task and a good testbed for various QCD calculations, spanning both perturbative and non-perturbative regimes through the creation of heavy quarks in the hard process and their subsequent evolution into physical bound states. Third, the prompt J/ψ is the main background for studies of the B mesons with charmonium decay modes.

In this thesis, charmonium production are studied in preparation for a cross section measurement, using data to be collected in the first LHC run by the CMS detector. The study is focusing on the decays of the charmonium to muon pair. The second chapter gives a brief introduction to the Standard Model of Particle Physics and detail the motivations for studying charmonium, first from a historical standpoint and then in the context of recent theoretical predictions and experimental results. An overview of the experimental setup of the CMS experiment and the LHC is given in Chapter 3. The forth chapter documents some of the Monte Carlo tuning and simulations I performed for quarkonium production in CMS and describes the used simulated event data.

Chapter 5 describes the CMS trigger system and the trigger scheme that will be used for J/ψ selection. Following this, Chapter 6 discusses the reconstruction of these events once they have passed through the CMS detector simulation, including details of muon and J/ψ reconstruction performance and efficiencies studies.

After reconstruction and event selection are performed, the measurement of the inclusive J/ψ differential cross section is explained in Chapter 7, as well as the separation between prompt and non-prompt components. Making use of the large B-hadron lifetime, the contribution of prompt J/ψ production can be separated from those from B-hadron decays.

Chapter 8 discusses the effects of the detector with miscalibrations and misalignments on the level we expect shortly after start-up, including the J/ψ mass and vertex resolution in different misalignment scenarios.

Studies of various systematic uncertainties are presented in Chapter 9, including theoretical uncertainties, limited knowledge of the detector response and efficiencies, and the corresponding Monte-Carlo modelings.

Chapter 10 summaries the yields, the total efficiency, the fitted B-fraction, and the systematic uncertainty in each p_T bin we expect to see in early data. We provide a brief prediction of the J/ψ differential cross-section measurement at an integrated luminosity of 3 pb^{-1} .

Conclusions are given in Chapter 11.

Chapter 2

Theoretical motivations

The first part of this chapter gives a brief summary of the Standard Model of Particle Physics. Later on, the focus is shifted to the charmonium, $c\bar{c}$ bound state. An introduction to the production mechanism of prompt charmonium in hadron collisions is given. The last part summarized the existed measurements on charmonium with many different detectors and compared with theoretical models.

2.1 The Standard Model

Particle physics studies the basic components of matter, their properties as well as the forces controlling them. So far, four basic forces are known: the strong, the electromagnetic, the weak, and the gravitational force. Each of them is described by a single theory, specifically chromodynamics, electrodynamics, flavourdynamics, and Einstein' s general theory of relativity. A rough overview of the strength of the forces is given in Tab. 2.1.

The Standard Model (SM) is an effective field theory which describes the strong, weak, and electromagnetic fundamental forces interacting between structureless or fundamental particles. It uses the theoretical framework of quantum field theory, and is therefore consistent with both quantum mechanics and special relativity. Gravity is by far the weakest of the four forces, and is not described within the

force	range	theory	action on	mediator
strong	10^{-13} cm	chromodynamics	quarks	gluons
electromagnetic	Infinity	electrodynamics	charged particles	photon
weak	10^{-16} cm	flavourdynamics	quarks, leptons	W and Z
gravity	Infinity	gravitation	all	graviton

Table 2.1: Range, theory, and mediating particle of the four fundamental forces [1].

Standard Model. There are three kinds of particles in the SM: the fermions with spin=$\frac{1}{2}$, the gauge bosons with spin=1, and the Higgs boson with spin=0.

The Standard Model combines the theory of quantum chromodynamics (which describes the strong interactions) with the theory of the electroweak interaction (which describes the weak and electromagnetic interactions.) Each of these theories are gauge field theories, meaning that they describe fermions coupled to bosons, with the bosons mediating the forces between fermions. Quantum field theory formalism uses the Lagrangian operator to completely describe the system of particles and their interactions. The Lagrangian of each set of bosons is invariant under a transformation called a gauge transformation, and each gauge transformation can be described by a unitary group called a "gauge group". Thus, these mediating bosons are often referred to as "gauge bosons". The gauge group of the strong interaction is $SU(3)$, and the gauge group of the electroweak interaction is $SU(2) \times U(1)$. Therefore, the Standard Model is often referred to as $SU(3) \times SU(2) \times U(1)$.

The fermions of the Standard Model are divided into two categories: quarks and leptons, depending on their interactions. There are six quarks (up, down, charm, strange, top and bottom) that participate in quantum chromodynamics processes, as well as six leptons (electron, muon, tau and their corresponding neutrinos) that not affected by the strong interaction. All of them carry weak isospin, leading to an interaction via the weak force. In addition to these particles a respective antiparticle exists with the same mass and opposite electric charge. Within the Standard Model the quarks and leptons are arranged in three generations in the order of increasing particle masses, as shown in Tab. 2.2. The first-generation particles constitute the fundamental particles of the known stable matter. The particles of generations II and III, replica of the fundamental particles with higher masses, were discovered due to collisions at high energy.

Generation	name	symbol	el. charge [e]	Mass [MeV/c^2]
1st generation	up quark	u	$\frac{2}{3}$	(1.5 - 3.0)
	down quark	d	$-\frac{1}{3}$	(3.5 - 6.0)
	electron	e	-1	0.511
	electron neutrino	ν_e	0	$< 2 \cdot 10^{-6}$
2nd generation	strange quark	s	$-\frac{1}{3}$	104^{+26}_{-34}
	charm quark	c	$\frac{2}{3}$	$(1.27^{+0.07}_{-0.11}) \cdot 10^3$
	muon	μ	-1	106
	muon neutrino	ν_μ	0	¡0.190
3rd generation	bottom quark	b	$-\frac{1}{3}$	$(4.20^{+0.17}_{-0.07}) \cdot 10^3$
	top quark	t	$\frac{2}{3}$	$(171.2 \pm 2.1) \cdot 10^3$
	tau	τ	-1	1777
	tau neutrino	ν_τ	0	¡18.2

Table 2.2: Three generations of leptons and quarks in the Standard Model and their masses [2]. The electric charge is given in unites of the positron charge, the mass in units of MeV/c^2.

The gauge bosons and some of their properties are list in Tab. 2.3. The gluons, mediating the strong interaction between color charged particles, are massless and carry color charges, so named because it binds or "glues" the quarks together to form nucleons. As there are eight independent color states, eight types of gluon exist. Due to their own color charge they can interact among each other. The gauge boson of the electromagnetic force is the massless and neutral photon. It only interacts with electrically charged particles, so it does not interact with itself. In contrast to these gauge bosons, the ones mediating the weak force, the W and the Z bosons, are massive. The W bosons additionally carry an electric charge.

name	force	symbol	el. charge [e]	Mass [GeV/c^2]
gluon	strong	g	0	0
photon	electromagnet	γ	0	0
W boson	weak	$W^{\pm}$	±1	80.398 ± 0.025
Z boson	weak	Z^0	0	91.1876 ± 0.0021

Table 2.3: Properties of the guage bosons [2]. The electric charge is given in unites of the positron charge, the mass in units of GeV/c^2.

2.2 Quantum Chromodynamics and Hadron Production

2.2.1 Strong Interaction and Quantum Chromodynamics

Quantum Chromodynamics (QCD) is the gauge field theory based on the $SU(3)$ gauge group, which describes the strong interactions of colored quarks and gluons, and is one of the components of the Standard Model. In strong interaction, "color" plays the role of charge. Whereas there one kind of electric charge in electromagnetic interaction (positive or negative), there are three kind of color charges in strong interaction, red, green and blue. Each quark has one of the three colors and anti quark has anti color charge. The color charge is conserved like electric charge is conserved. Strong interaction works only between quarks, but not with leptons since leptons do not carry color. Strong interaction bind quarks into hadrons, such as proton or pion. Also, force between nucleons is strong force, and strong interaction is responsible for binding protons and neutrons into a nucleus.

In weakly bound systems (hydrogen, for example) the components may be separated if sufficient energy is added, for example in the form of a collision. However, in QCD bound systems, it is generally understood that the binding force is too strong for this to occur, regardless of the amount of energy added. If a hadron is struck hard, the constituent quarks do not simply come free. Rather, additional $q\bar{q}$ pairs are generated from the color field, and recombine to form more hadrons. This process of generating $q\bar{q}$ pairs in energetic strong interactions is central to models of hadron production.

The strong coupling constant α_s parameterized the strength of the quark-gluon and gluon-gluon couplings, and it is analogous to the electromagnetic coupling constant α. The value of α_s depends on the transverse momentum of the process being studied, a characteristic known as "running coupling constant". At low energies, $E < 1$ GeV, the coupling is so strong that perturbation theory breaks down . At higher energies α_s decreases, becoming small enough for perturbation theory to be applied reliably. This decrease in α_s implies that in the limit of very high energies, quarks behave as free particles, a property known as asymptotic freedom. In general, perturbative QCD successfully describes hard processes in high energy collisions produced at modern particle colliders.

However, the understanding of strong dynamics at low energies remains a major challenge for particle physics. With perturbation theory unavailable, a variety of theoretical models must be applied to different situations. For example, the original quark model is very useful in classifying hadrons and understanding their quantum numbers. However, it does not include any dynamics and therefore is not able to predict quantities such as masses or scattering cross sections. Meanwhile, several models exist to deal with the process of hadronization, the evolution of a single energetic quark or gluon into a jet of hadrons. These models can be tested in the study of jet production at collider experiments.

2.2.2 The charmonium families

Heavy quarkonium production in hadronic collisions provides an ideal testing ground for our understanding of QCD. It involves both perturbative and non-perturbative processes. The production of the heavy quark pair occurs at short distances and can be calculated perturbatively due to the large scale of the quark masses, whereas the non-pertubative QCD effects that bind the heavy quark-antiquark pair into quarkonium can only be factorized into a wave function. The charmonia states of $c\bar{c}$ are the well-understood hadrons. These are to some extent non-relativistic systems, and so are analogous to electromagnetically bound systems like hydrogen or positronium. Charmonia may thus be modeled as a quark and an anti-quark moving in a central potential, leaving the form of the potential to be fitted to data [3]. The spectra (Fig. 2.1) of the $c\bar{c}$ bound system as well as Tab. 2.4 summarizes the characteristics of the observed states as of today. In this context, "bound" refers to states with mass below the open-flavor threshold ($2m_D$ for charmonia). In general, states above this threshold decay rapidly to $D\bar{D}$ and are not so amenable to study as the bound states.

Meson	$n^{2S+1}L_J$	J^{PC}	Mass (GeV)	$\Gamma_{\mu\mu}$ (keV)
η_c	$1\ ^1S_0$	0^{-+}	2.980	N/A
J/ψ	$1\ ^3S_1$	1^{--}	3.097	5.40
χ_{c0}, χ_{c1}, χ_{c2}	$1\ ^3P_{0,1,2}$	0^{++},1^{++},2^{++}	3.415,3.511,3.556	N/A
h_c	$1\ ^1P_0$	1^{+-}	3.523	N/A
$\eta_c(2S)$	$2\ ^1S_0$	0^{-+}	3.594	N/A
ψ'	$2\ ^3S_1$	1^{--}	3.686	2.12

Table 2.4: Properties of charmonia (cf.Ref. [2]).

At the J/ψ mass, it is estimated that $\alpha_s(M_{J/\psi}) \approx 0.25$ [4]. These values can be used to estimate the quark velocities in the potential model [12], yielding $\nu_s^2 \approx 0.3$. The non-relativistic approximation even if not very accurate for charmonia, is useful nonetheless. The production of heavy quarks in high-energy particle collisions is an active field of research. Perturbative QCD can be used to make predictions of inclusive heavy flavor production, i.e. charm, bottom and top production [6].

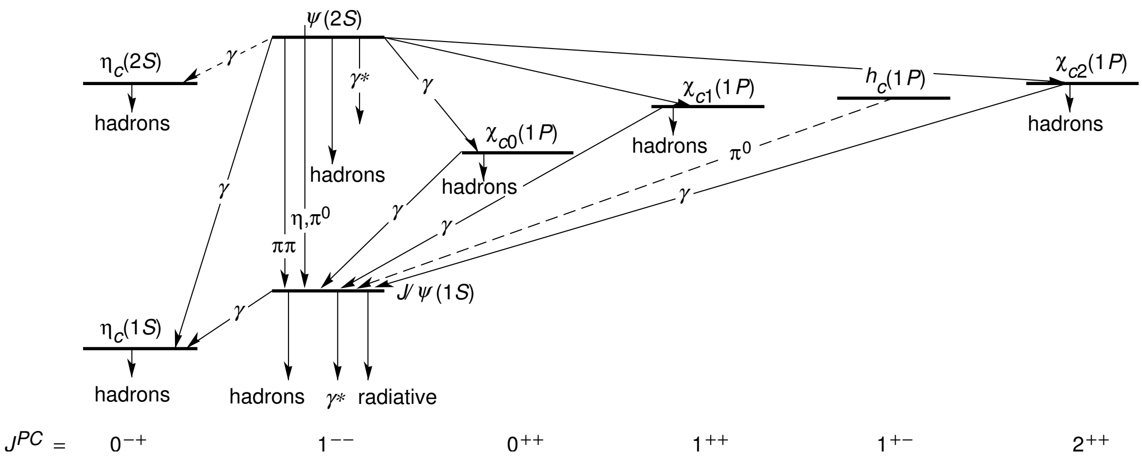

Figure 2.1: Spectrum and transitions of the charmonium family (from Ref. [2].

Provided the colliding beam particles have sufficient energy, heavy quarks may be produced in a variety of collisions, for example at $e+e-$, ep and pp colliders. The highest energies are attained in pp collisions, where heavy quark pairs are produced by $q\bar{q}$ and gg interactions between the components of the proton. At high energies, due to asymptotic freedom the incoming hadrons behave approximately as beams of independent quarks and gluons. The momentum distributions of the quarks and gluons within a hadron are characterized by a set of measured parton distribution functions, which depend on the energy scale of the production process. The inclusive heavy quark production cross section thus depends on the parton distribution functions and the amplitudes for $q\bar{q}$ and gg collisions to produce heavy quarks. The study of quarkonium production in high-energy collisions is useful because it involves QCD processes at different energy scales. First, the heavy quark-anti-quark pair is produced in an energetic collision (at distance $r \sim 1/M_{Q^2}$), then the pair binds together into a quarkonium state ($r \sim 1/\alpha_s(M)M$). If the energy scales of these two steps differ sufficiently, the cross section for the production of a quarkonium meson H may factor into two parts First, the cross section for inclusive production of the heavy quark pair $Q\bar{Q}$, which can be calculated perturbatively ($r \ll 1/\Lambda_{QCD}$), and second is the probability for the $Q\bar{Q}$ pair to evolve into the bound state H, which must be modeled. The technique of separating a production process into two stages is formally known as factorization and is central to QCD calculations of high-energy collisions. The validity of the factorization of the quarkonium production cross section depends on the energy scales and interactions involved in the two steps, and can be tested experimentally.

Three types of models have been used to describe quarkonium formation: the color-singlet model; the color-evaporation model with a follow-up soft color interaction model; and the color-octet model. In the color-singlet model, the quarkonium meson retains the quantum numbers of the produced $\mathrm{c\bar{c}}$ pair, and thus each J^{PC} state can only be directly produced via the corresponding hard scattering color-singlet sub-processes. In the color-evaporation model, the directly produced quarkonium meson is not constrained to the same J^{PC} state as the $\mathrm{c\bar{c}}$ pair produced in the hard scatter because of the emission of soft gluons during the meson's formation. The color-octet mechanism extends the color-singlet approach by taking into account the production of $\mathrm{c\bar{c}}$ pairs in a color-octet configuration. The color-octet state evolves into a color-singlet state via emission of soft gluons.

2.3 Charmonium Production

There are three processes that dominate the production of charmonium states in high energy hadron collisions. The first is called *direct production*, in which the a $c\bar{c}$ pair is produced in the particle collision, and the two quarks combined producing a colorless J/ψ meson. The second is in the decay of a prompt produced heavier charmonium state, for example the production of a J/ψ meson in the decay of prompt χ_c or $\psi(2S)$ meson, and is known as feeddown. The third process is the production of a bottom quark fragmenting into a B hadron, which can subsequently decay into ψ and other hadrons. This production is further referred as $non-prompt\ production$ or B *production*. This third production is distinguished from the first two by the relatively long lifetime of B-hadrons, about 1.5 ps. The decay vertex of a B-hadron is usually far enough from the primary interaction point of the colliding beams to be identified as a displaced secondary vertex. The first two types of charmonium production occur at the primary interaction point and are known as *prompt production*. Tab. 2.5 summarizes the different processes.

1^{st} step	2^{nd} step	3^{rd} step	Type
$p\bar{p} \rightarrow c\bar{c} + X$	$c\bar{c} \rightarrow J/\psi$	–	Prompt prod. directly
	$c\bar{c} \rightarrow \chi_c$	$\chi_c \rightarrow J/\psi + \gamma$	Prompt prod. by decay ofχ_c
	$c\bar{c} \rightarrow \psi'$	$\psi' \rightarrow J/\psi + X$	Prompt prod. by decay of ψ'
$p\bar{p} \rightarrow \bar{b}c + X$ $\bar{b}c \rightarrow \bar{c}c + \ell^- + \bar{\nu}_\ell$ etc ...	$c\bar{c} \rightarrow J/\psi$ $c\bar{c} \rightarrow \chi_c$	– $\chi_c \rightarrow J/\psi + \gamma$	Non-prompt production

Table 2.5: Different processes involved in J/ψ production accompanied by quantities used in the following discussion.

In the following, the three main models for inelastic Charmonium production will be presented in their historical order.In all models, the production of the c$\bar{\text{c}}$ pair is treated separately from its evolution into a bound state (factorization); factorization is considered to be legitimate because the production of the c$\bar{\text{c}}$ pair proceeds on a short time scale of order $1/m_c$, while the formation of the bound state is a non-perturbative long distance process on a time scale longer than $1/\Lambda_{QCD}$.

2.3.1 The Color Evaporation Model

The Color Evaporation Model (CEM), also referred to as the "local duality approach", has been developed in the late seventies by Fritzcsh et al. [7, 8] and was revived in 1996 by Amundson et al. [9, 10]. In this approach, the sum of the cross sections of all $c\bar{c}$ bound states is given by the integral of the cross section for $c\bar{c}$ production, $\sigma_{c\bar{c}}$, from the lower threshold $2m_c$ up to the threshold for the production of a pair of heavy-light mesons, $2m_D$:

$$\sigma_{onium} = \frac{1}{9}\int_{2m_c}^{2m_D} dm \frac{d\sigma_{c\bar{c}}}{dm} \tag{2.1}$$

where $\sigma_{c\bar{c}}$ is calculated in perturbation theory. The factor 1/9 represents the statistical probability for the quark pair to be asymptotically in the color singlet state. This transition is thought to proceed via multiple soft - gluon interactions, implying a statistical treatment of color. Due to the multiple soft-gluon exchanges, Charmonium produced via the color evaporation mechanism is predicted to be unpolarized [10], which is a very distinct feature compared to other models for inelastic Charmonium production.

To obtain the cross section for a specific Charmonium state such as J/ψ, the factor ρ_ψ is introduced:

$$\sigma_\psi = \rho_\psi \times \sigma_{onium} \tag{2.2}$$

The factor ρ_ψ is of the order of $1/N_{onium}$, where N_{onium} is the number of Charmonium states with mass between $2m_c$ and $2m_D$. Since ρ_ψ can depend on the specific state, the production process, the centre of mass energy, the transverse momentum of the charmonium, m_c and the gluon density, absolute predictions in the Color Evaporation Model are difficult. A comparison to the recent experimental data is given in [58]. Although qualitative agreement with the data is observed, the Color Evaporation Model receives rather little interest in the literature due to its weak predictive power.

2.3.2 The Color Singlet Model

The Color Singlet Model (CSM) [11], developed since 1980, was the first to provide quantitative predictions for charmonium production in a wide variety of environments: in hadron collisions, photoproduction and e^+e^- collisions. The J/ψ production is thought to proceed in two steps: in the first step, a $c\bar{c}$ pair with the same quantum numbers - spin, angular momentum and C-parity - as charmonium state is produced in a color singlet state; the second step contains the binding of the $c\bar{c}$ into charmonium state. The cross section can then be factorized into a short distance matrix element describing the cc production in a region of size $1/m_c$, and a long distance factor that describes the non-perturbative dynamics of the bound state formation. Equation 2.3 shows the form that the inclusive J/ψ cross section takes in the Color Singlet Model:

$$d\sigma(J/\psi + X) = d\hat{\sigma}(c\bar{c}(1,^1S_1 + X)|R_\psi(0)|^2, \tag{2.3}$$

where $R_\psi(0)$ is the J/ψ wave function at the origin, and the notation "1" is used to denote that $c\bar{c}$ pair is in color singlet state.

The short distance part $d\hat{\sigma}$ can be calculated using a perturbative expansion in $\alpha_s(m_c)$, while the long distance part is related to the decay width Γ_{ll} of the charmonium:

$$\Gamma(J/\psi \to l^+l^-) \simeq \frac{4\alpha^2}{9m_c^2}|R_\psi(0)|^2 \text{ (leading order)}. \tag{2.4}$$

In high-energy hadronic collisions, the leading order process in α_s^3 is expected to dominate at lower p_T. Fig. 2.2(a) is an example of a gluon fusion process, in which the quarkonium is produced in the collision of two incoming partons. The second main contribution at the lower p_T comes from the subprocess shown in Fig. 2.2(b), where the $c\bar{c}$ states with various quantum numbers contribute to J/ψ production, through $\chi_{cJ} \to J/\psi + \gamma$ decays.

Two effects can significatively enhance the predicted cross section for the

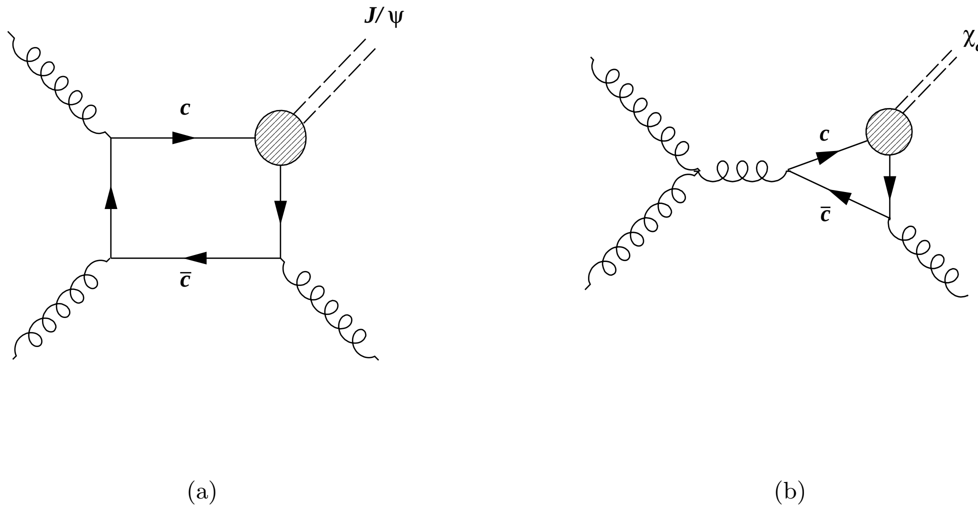

Figure 2.2: Examples of diagrams for Color Singlet $^3S_1$ and ^3P_J charmonium production. The leading order diagram is shown in (a) and occurs at order α_s^3; it is a two-gluon fusion process. χ_{cJ} production process, shown in (b), is the second main contribution at the lower p_T region.

prompt charmonium production at high p_T. One is the parton fragmentation contribution which represents a dominant source of prompt quarkonia at high energies [12, 13]. Fig. 2.3 shows a Feynman diagram involved in ψ production via gluon fragmentation which is $\mathcal{O}(\alpha_s^5)$. Given that the leading order diagram, Fig. 2.3(a), is the contribution from this diagram to the total ψ cross section should be significantly suppressed. Nevertheless, if the ψ has a sufficiently large transverse momentum $p_T \gg M_\psi$, then the diagram will be dominated by configurations where the gluon has $Q^2 \sim M_\psi^2 \ll E_{gluon}^2$. In this case the gluon is nearly real, and diagram is enhanced by a factor of p_T/M_ψ. When p_T becomes large enough this diagram starts dominating over the leading order diagrams. Because this process produces a (nearly) on-shell gluon which fragments into a ψ, it is referred to as gluon fragmentation production. The same mechanism also contributes to productions of chi_c mesons. Actually, for the chi_c, one less gluon needs to be emitted, so the process is $\mathcal{O}(\alpha_s^4)$. A ψ can also be produced by a fragmentation process where a charm quark fragments, as shown in Fig. 2.3(b), although this is not as essential, because the production of a charm quark is substantially suppressed in comparison with the gluon production.

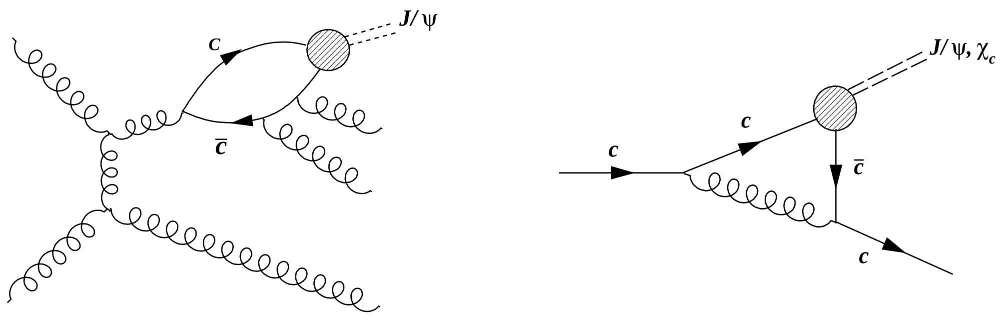

(a) (b)

Figure 2.3: Gluon (left) and charm (right) fragmentation production of ψ in the color singlet model.

2.3.3 NRQCD and the Color Octet Mechanism

The approach discussed here was first applied for the prediction of decay rates of P-wave charmonium states in the early nighties by Bodwin et al. [14], and later developed into a complete theory [15]. It is known as the Non-relativistic QCD (NRQCD) factorization formalism. NRQCD [16] is an effective field theory [17, 18], which treats quarkonium as an approximately non-relativistic system. In this framework, charmonium production is described as two-step process: $c\bar{c}$ pair production at perturbative level and the subsequent evolution to colorless vector meson through soft gluon emission at the non-perturbative domain. This argument is advocated by the fact that the $c\bar{c}$ pair is produced at distance $1/m_c$, m_c standing for heavy quark mass, which is much smaller than $1/\Lambda_{QCD}$, the typical QCD scale for bound-state system. According to the color octet formulation [20, ?], the wave function of an S-wave quarkonium state in terms of Fock state decompositions is given by

$$\begin{aligned}|\psi_Q\rangle =&\mathcal{O}(1)|\mathrm{Q}\bar{\mathrm{Q}}[^3S_1^{(1)}]\rangle + \mathcal{O}(v)|\mathrm{Q}\bar{\mathrm{Q}}[^3P_J^{(8)}]g\rangle + \mathcal{O}(v^2)|\mathrm{Q}\bar{\mathrm{Q}}[^1S_0^{(8)}]g\rangle + \\ &\mathcal{O}(v^2)|\mathrm{Q}\bar{\mathrm{Q}}[^3S_1^{(8)}]gg\rangle + ...\end{aligned} \tag{2.5}$$

where v is a typical relative velocity of constituent quarks in quarkonium state. Here, the usual spectroscopic notation, $^{2S+1}L_j$, is used, and the color state is indicated by (1) for singlet and (8) for the octet. The production cross section for charmonium states, e.g. $A + B \rightarrow J/\psi + X$, can be expressed as

$$d\sigma(J/\psi + X) = \sum_n d\hat{\sigma}(A + B \rightarrow \mathrm{Q}\bar{\mathrm{Q}}[n] + X) \cdot \langle \mathcal{O}_n^{J/\psi} \rangle, \tag{2.6}$$

where n denotes an on-shell $c\bar{c}$ pair in a definite color, spin and angular momentum state. Since the cc pair is often produced as a color octet state in this model, the model is named the Color Octet Mechanism (COM).

As in case of CSM, the entire process cannot be calculated using perturbative theory. However, a non-perturbative part ca be factored out. This part is a well-defined matrix elements, which could be calculated using lattice QCD, or extracted from experimental measurements. It can be argued that the matrix elements is independent of the kinematics ill the perturbative part, which results ill au unknown normalization, but does not affect the spectrum. An important property of the matrix elements, which greatly increases the predictive power of NRQCD, is the fact that they are universal, i.e. process independent. Thus, a matrix element measured at one experiment can be used to make predictions for another experiment, or compared with the matrix element measured at that experiment. Finally, naive power counting provides a order of magnitude estimate for the matrix element. In terms of Feynman graphs, what happens is that one or more of gluons radiated from the $c\bar{c}$ pair is removed from the perturbative portion, and added to the non-perturbative portion, as shown in Fig. 2.4. The gluon can become extremely soft, greatly enhancing the contribution of the diagram. In fact, a typical approximation is to assume that the gluon carries no energy, only the excess color.

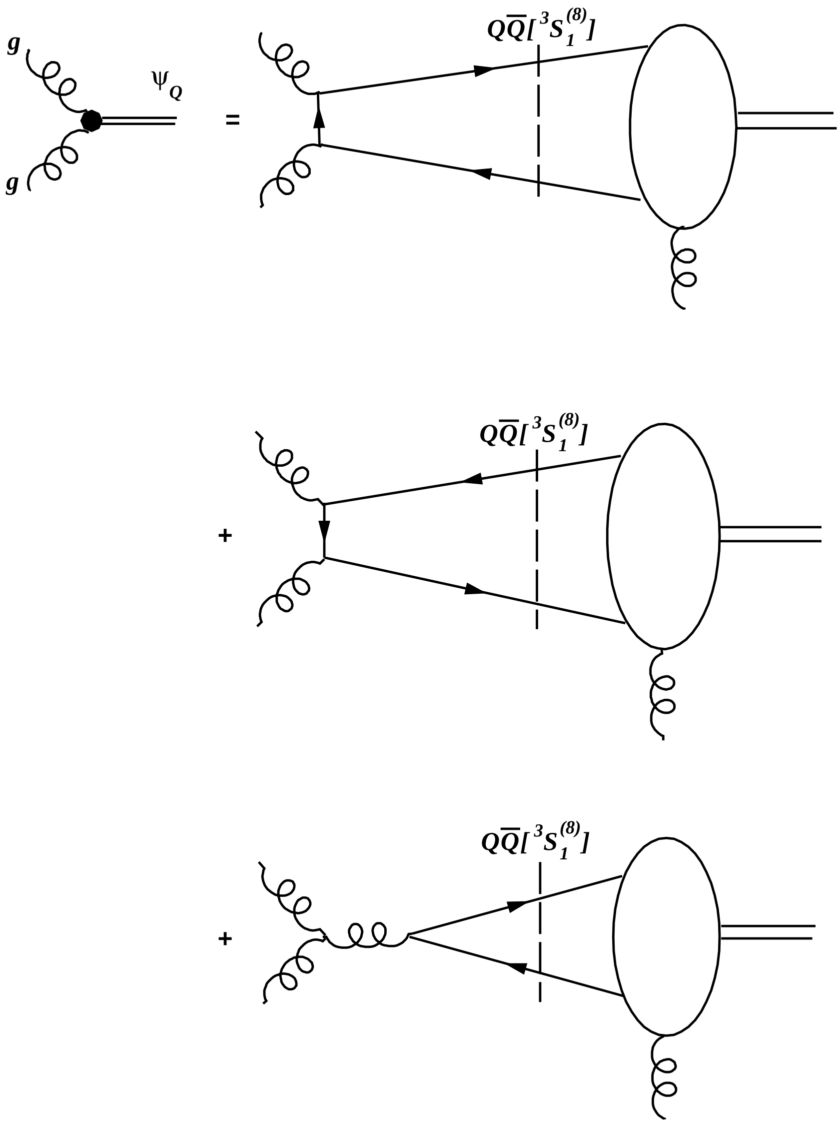

Figure 2.4: Color-octet diagrams which mediate $gg \rightarrow \psi_q$ production at $\mathcal{O}(\alpha_s^2)$. The sum of these graphs vanishes when both incoming gluons are on-shell.

2.3.4 B production

The non-prompt J/ψ production is from the decay of B hadrons. The initial interaction produces a b quark. which fragments into a B hadron that subsequently decays into a ψ and other particles. At next-to-leading order, the diagrams for

b quark production can be grouped into three classes, shown in Fig. 2.5. Each of these processes has distinct characteristics. The first diagram represents the process of gluon fusion. The $b\bar{b}$ pair produced by this reaction is separated by 180° in azimuthal angle, and results in two well separated jets. Gluon splitting (second diagram) tends to produce b quarks which are close together, as the mass of the virtual gluon tends to be small. As a result, the decay products of the two quarks may appear to come from a single parent, especially after fragmentation effects and experimental resolution are included. The third class, flavor excitation, is often the result of the gluon scattering off one of the virtual b quarks that form the cloud around the valence quarks. In this case, the other b proceeds close to the initial proton or anti-proton direction.

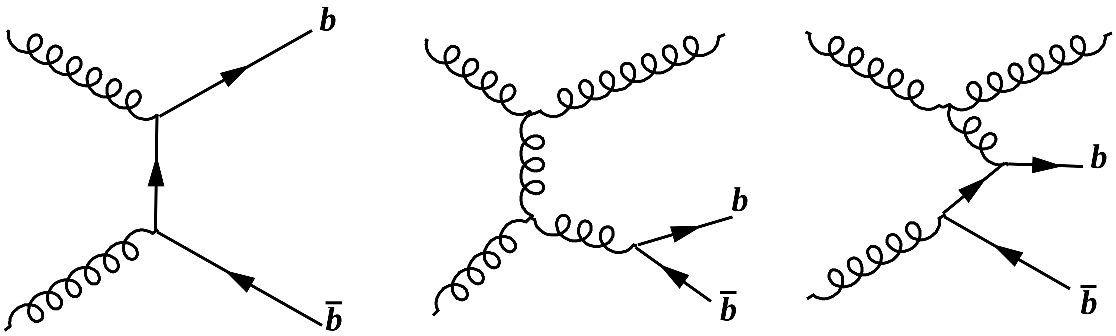

Figure 2.5: Feynman diagrams for b production from gluon fusion (left), gluon slitting (center) and flavor excitation (right).

After the b quark fragments into a B hadron, it can decay to a ψ or chi_c through diagrams such as Fig. 2.6. This decay is suppressed relative to the decay $B \rightarrow D+X$ for several reasons. First, the W must decay into $\bar{c}s$, while for the $B \rightarrow D + X$ decay, all possible W decay modes are allowed. This reduces the rate by about a factor of three. Additionally, the $\bar{c}$ must have the same color as the c quark, as the fragmentation of the color octet $c\bar{c}$ state into charmonium is suppressed. This leads to another factor of three. Finally, the c and $\bar{c}$ quarks must have similar momenta, so that they can form a bound state. This results in the relatively small branching ratios of $\mathcal{B}(B \to J/\psi X) = 1.16 \pm 0.10\%$ and $\mathcal{B}(B \to \psi' X) = 0.48 \pm 0.24\%$ [2]. While these branching ratios are small, it is a experimental fact that the two muons from b decay provide a excellent experimental trigger, so the process $B \to \psi X$ is tremendously useful from a practical standpoint.

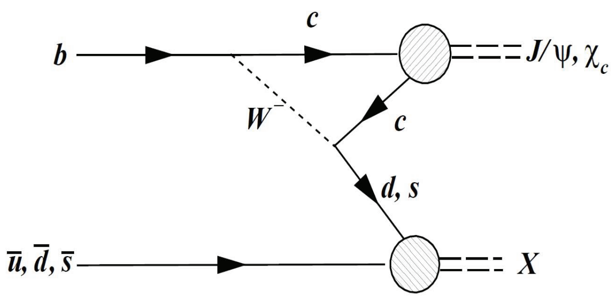

Figure 2.6: Typical diagrams of b meson decay to charmonium states.

2.4 Summary of the Charmonium Measurements

The models discussed above for quarkonium formation lead to different expectations for the production rates and polarization of the quarkonium states. A prior, the same sets of parameters should apply to a variety of processes involving quarkonium production, including the production in the hadron collisions at Tevatron Collider in Fermilab, in hadron-nucleon collisions at fixed target experiments, inelastic charmonium production at HERA at DESY, associated production of a $J/\psi + \gamma$, and the measurements of quarkonium polarization.

Quarkonium production at the Tevatron

Initially, prompt production of charmonium in hadron collider was assumed to be described in the Color Singlet Model. This approach had the benefit that all non-perturbative aspects could be absorbed into the wave function of the quarkonium state. This model enjoyed some success until 1997. In Run I of the Tevatron, the Collider Detector at Fermilab collaboration (CDF) the prompt cross-sections for the production of several charmonium states in $p\bar{p}$ collisions at a centre-of-mass energy of 1.8 TeV [21, 22]. The CDF data for production of direct J/ψ, prompt $\psi(2S)$, and prompt J/ψ from decay of χ_c are shown in Fig. 2.7. In the CDF analysis, prompt J/ψ's that do not come from decays of $\psi(2S)$ or χ_c were assumed to be produced directly. Discrepancies between the CSM and data were also observed in Υ production measurements [24, 25].

These discrepancies were largely resolved by the introduction of the Color Octet Mechanism of quarkonium production [26]. This model allows contributions from the production of $\mathrm{Q\bar{Q}}$ pairs in a color octet state, whose normalization are determined by color-octet matrix elements. Tab. 2.6 shows the values of the charmonium matrix elements that are obtained in the fit of Ref. [26, 27]. The color-singlet matrix elements are taken from the potential-model calculation of Refs. [28, 29]. The color-octet matrix elements have been extracted from the CDF data with:

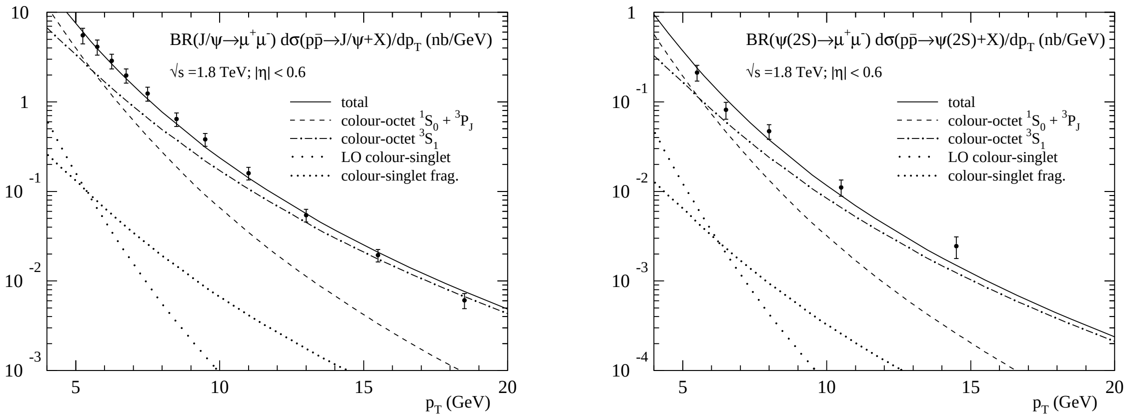

(a) (b)

Figure 2.7: Differential cross sections for the production of direct J/ψ(a) (left) and $\psi(2S)$ (right) at the Tevatron as a function of p_T. The data points are CDF Run 1 measurements [21]. The dotted curves are the CSM contributions. The solid curves are the NRQCD factorization fits, and the other curves are individual color-octet contributions to the fits. These figures have been extracted from Ref. [26].

CTEQ5L parton distribution functions [30], reorganization and factorization scales $\mu = (p_T^2 + 4m_c^2)^{1/2}$ and $m_c = 1.5$ GeV/c^2. The Altarelli-Parisi evolution has been included for the $\langle \mathcal{O}_8^{\chi_c}(^3S_1)\rangle$ fragmentation contribution. See Ref. [29] for further details. The extraction of the various color-octet matrix elements relies on the differences in their p_T dependencies. Smaller experimental error bars could help to resolve the different p_T dependencies with greater precision.

H	$\langle \mathcal{O}_1^H\rangle$	$\langle \mathcal{O}_8^H(^3S_1)\rangle$	$M_{3.5}^H$
J/ψ	1.16 GeV^3	$(1.19 \pm 0.14) \times 10^{-2}$ GeV^3	$(4.54 \pm 1.11) \times 10^{-2}$ GeV^3
$\psi(2S)$	0.76 GeV^3	$(0.50 \pm 0.06) \times 10^{-2}$ GeV^3	$(1.89 \pm 0.46) \times 10^{-2}$ GeV^3
χ_{c0}	0.11 GeV^5	$(0.31 \pm 0.04) \times 10^{-2}$ GeV^3	

Table 2.6: NRQCD production matrix elements for charmonium states obtained from the transverse momentum distributions at the Tevatron [26].

However, the COM polarization predictions are in disagreement with experimental data: production via a color-octet state predicts a significant transverse polarization of ψ's and Υ 's, which have not been observed experimentally in J/ψ or ψ $(2S)$ production at the Tevatron or fixed target experiments. Fig. 2.8 shows that the recent Tevatron polarization measurement is inconsistent with the COM prediction [32, 33].

A overview of the status of the production of J/ψ, ψ' and υ in high-energy hadron collisions is given by J. P. Lansberg [48].

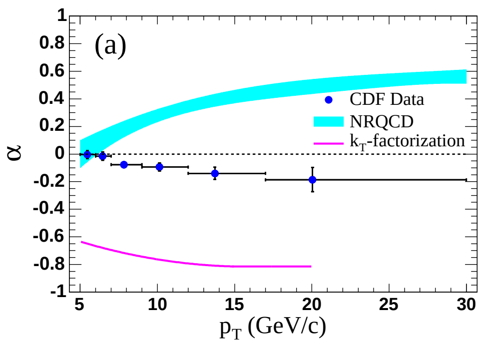

(a)

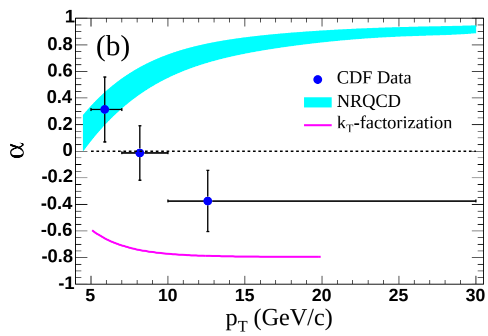

(b)

Figure 2.8: Prompt polarizations as functions of p_T: (a) J/ψ and (b) $\psi(2S)$. The band (line) is the prediction from NRQCD [27] (the k_T-factorization model [34]).

The CSM in its own has been revived recently, when it was shown that next-to-leading-order (NLO) and next-to-leading-order (NNLO) QCD contributions [37, 38, 39, 40] as well as s-channel cut contributions [41, 42] arising from relativistic corrections could lead to an enhancement of the production cross section of the CSM, while predicting a polarization closer to the data. Fig 2.9 present the higher order calculations, which offer very promising agreement with Tevatron data on bottomonium production and polarization, while still has gaps from the charmonium results. It is also worth noting that currently the theoretical uncertainties on the polarization still dominate over those from experiment so no clear statement can yet be made regarding the Tevatron results.

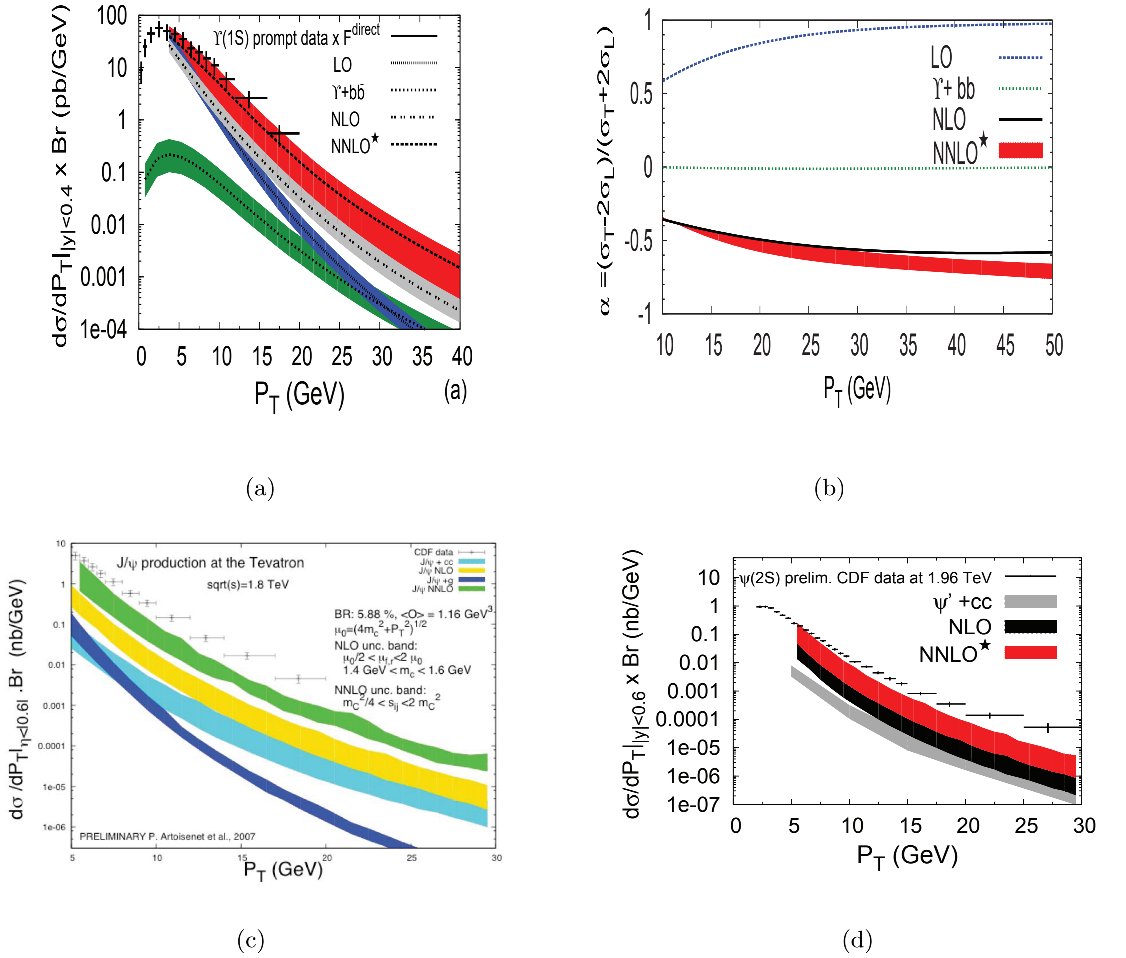

Figure 2.9: (a) Cross section and (b) polarization for $\Upsilon(1S)$ production as a function of p_T at CDF at $\sqrt{s} = 1.8$ TeV, with overlaid results of color singlet model calculations (and error bands) up to NNLO. (From Ref. [40]). J/ψ (c) and $\psi(2S)$ (d) result still have gaps.

Quarkonium production in fixed-target experiments

The Fermilab E866/NuSea Collaboration measured a J/ψ polarization in proton-copper collisions at ps = 38:9 GeV with an average polarization of $0.069 \pm 0.004 \pm 0.080$ [35], which agrees with previous fixed target findings of very small polarization, but with substantially better accuracy. The measurement is lower than predictions based on the COM, which range from 0.35 to 0.65. A much larger transverse polarization for $\Upsilon(2S)$ and $\Upsilon(3S)$ than for $\Upsilon(1S)$ was also observed in the bottomonium production in the p-Cu collisions at $\sqrt{s} = 38.9$ GeV by the E866 experiment [36] (see Fig. 2.10).

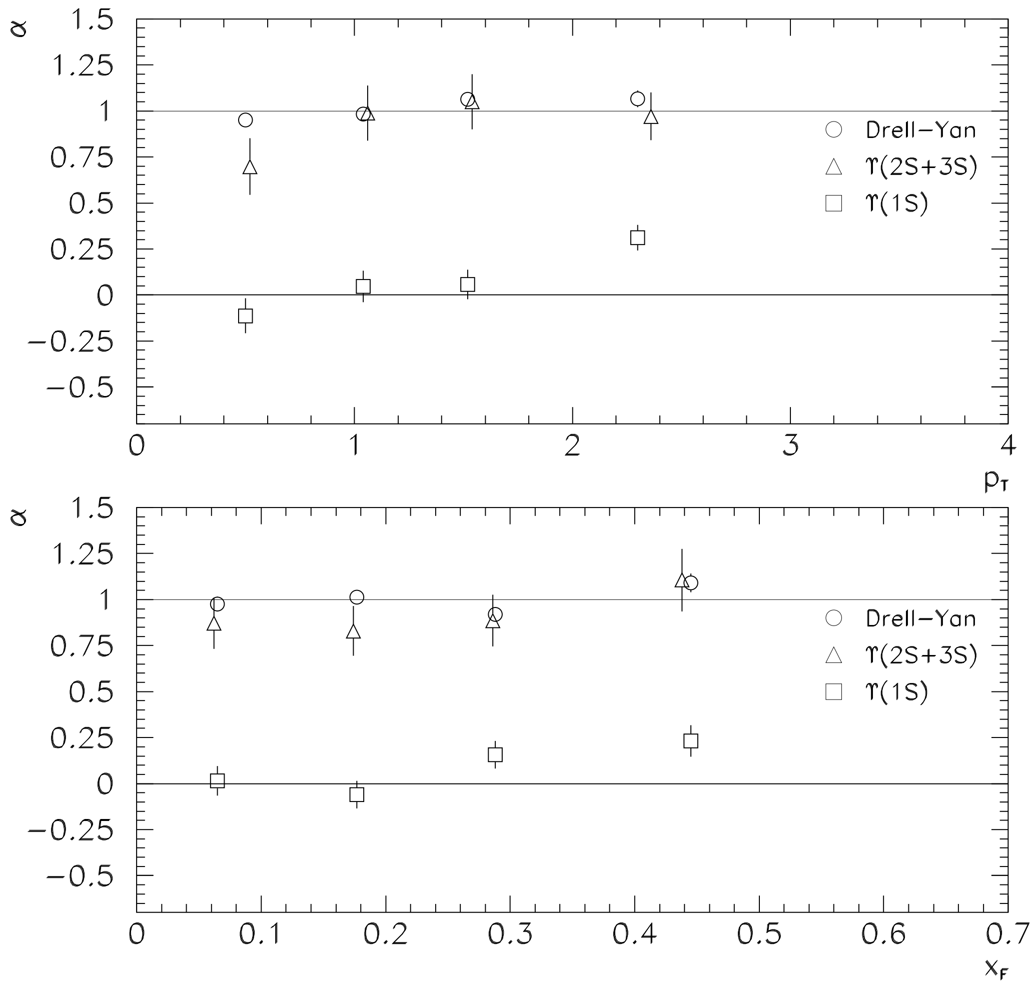

Figure 2.10: Polarization of Υ mesons and Drell–Yan pairs as a function of p_T and x_F in p–Cu collisions in the E866 experiment. From Ref. [36].

Quarkonium production at HERA

Theoretical calculations based on the NRQCD factorization approach also improved the agreement between the rate of inelastic J/ψ photoproduction observed in ep collisions and predictions [31]. Fig. 2.11 shows the measurements of the prompt

J/ψ cross-section by the H1 collaboration [45] and the ZEUS collaboration [46], compared with the theoretical predictions given in Ref. [26].

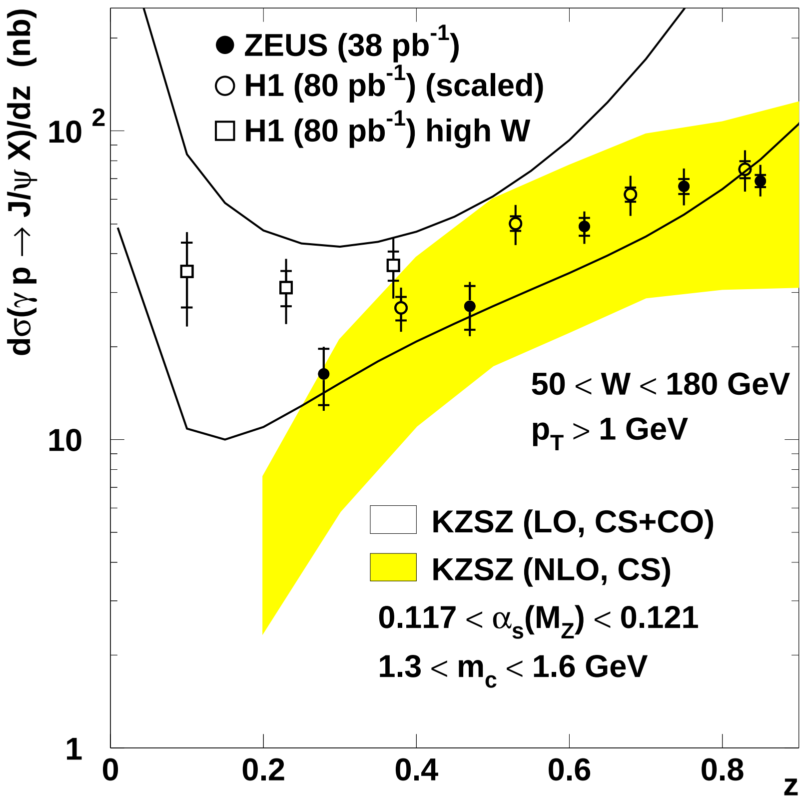

Figure 2.11: The rate for inelastic J/ψ photoproduction at HERA as a function of z. The open band represents the LO NRQCD factorization prediction [26]. The solid band represents the NLO colour-singlet contribution [44, 26]. The data points are from the H1 [45] and ZEUS [46] measurements.

A comprehensive overview [43] of heavy quarkonium physics is presented by Quarkonium Working Group (QWG) [47]. Tab. 2.7 (from Ref. [43]) contains the most recent summary of the ongoing experiments studying quarkonium production. A subjective scorecard for the experimental results comparing with theoretical models is shown in Fig. 2.12. Whereas the CSM fails to describe the charmonium production at the Tevatron, it is more successful in describing the J/ψ production at the ep machines (HERA). An absence of the J/ψ polarization, observed at both the

Tevatron and the fixed target energies is a setback for the Color Octet Model.

Experiments	**Colliding Particles**		**$\sqrt{s}$ / nucl. [GeV]**	**Runs**	**Recorded Data**
FOCUS/E831	γ	BeO	18	96–97	
SELEX/E781	Σ^-, π^-	C,Cu	33	96–97	15B int's
NuSea/E866	p	Cu	38	96–97	9M J/ψ
Hera-B	p	C,Al,Ti,W	41	00,02–03	308K J/ψ
HERA Run I	$e^\pm$	p	300,318	93–00	130 pb^{-1}
HERA Run II	$e^\pm$	p	318	03–04	$\sim$70 pb^{-1}
Tevatron Run I	p	$\bar{p}$	1800	92–96	125 pb^{-1}
Tevatron Run II	p	$\bar{p}$	1960	02–04	$\sim$400 pb^{-1}
LEP (I and II)	e^+	e^-	90–210	89–00	3.6M bb
BES (I and II)	e^+	e^-	2–5	89–03	7.8M+58M J/ψ

Table 2.7: Summary of recent experiments for heavy quarkonium production from Ref. [43].

In view of the puzzling situation, and given the large yields of quarkonia which will be produced at the LHC, the early data collected by CMS present an excellent opportunity to study quarkonia. Thanks to the higher collision energy and luminosity, the studies of quarkonia with CMS will probe higher momentum values than feasible at CDF and DZero, extending the test of different production mechanisms; CMS also offers a better pseudorapidity coverage, giving the possibility to study many other dependencies. The precise tracking permits us to disentangle the prompt J/ψ production from that coming from B-hadron decays, and therefore allows us to determine the B-hadron cross section with a relatively small integrated luminosity.

Examples of studies aimed at understanding the quarkonium production mech-

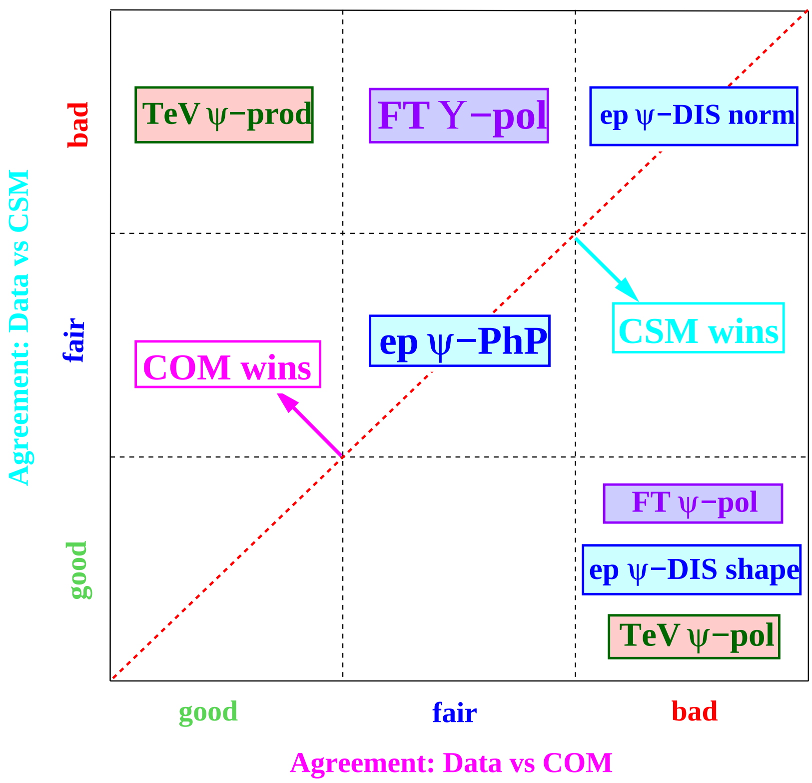

Figure 2.12: Subjective comparison of experimental results with theoretical models (from Ref. [49]).

anism are the differential cross section and the polarization measurements. In addition, it should be possible to extract additional information by looking for observations that take into account the kinematics of particles produced in association with prompt J/ψ's [50]. To obtain a complete picture, J/ψ, $\psi(2S)$, Υ $(1S)$, Υ $(2S)$ and Υ $(3S)$ should all be investigated. Studying bottomonia, in fact, provides a cleaner environment for testing the theoretical predictions for prompt quarkonia, as there is no contamination from non-prompt Υ 's. Also, the heaviness of Υ makes it better described by NRQCD since it moves slower, i.e. more non-relativistic. On the other hand, the cross section of Υ being an order of magnitude smaller, it will take longer time to accumulate the necessary statistics. Moreover, it should be pointed out that for an unambiguous understanding of quarkonium production, direct production should be studied as well, for example χ_c production could be studied by radiative decays into J/ψ's.

Chapter 3

The CMS experiment at LHC

This chapter gives a introduction to the Large Hadron Collider (LHC) built by the European Organization for Nuclear Research (CERN), which was created in 1954 by a convention of 12 European states. Today, CERN is composed of 20 member states and 8 observer states. CERN was founded with an aim of building a laboratory having the most advanced scientists and technical resources. The accelerators and the detectors are the tools necessary for the physicists to study the basic components of our universe. The laboratory is located at the French-Swiss border near Geneva. One of the experiments being operated at the LHC is the Compact Muon Solenoid (CMS), whose configuration and properties are described in the main part of this chapter.

3.1 The Large Hadron Collider at CERN

A particle accelerator and a detector together form the basis of a high energy physics experiment. Two kinds of experiments can typically be conducted: the collision of particles with a fixed target or the head-on collision with a similar beam of opposite direction. The type of particle accelerate, and the energy which they attain, determine what areas of particle physics can be studied.

In December 1994, the approval of the Large Hadron Collider (LHC) project [51]

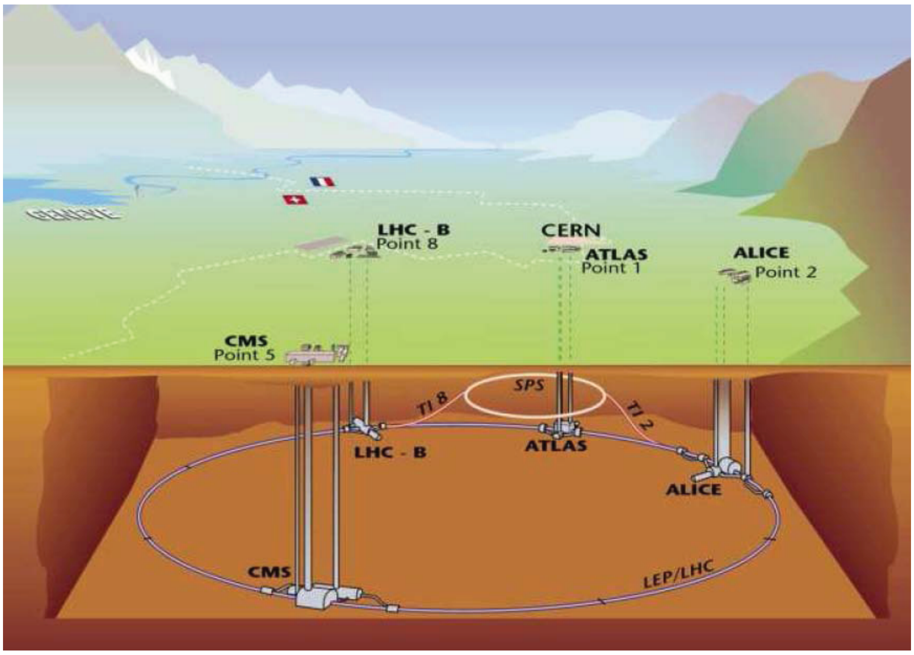

Figure 3.1: The Large Hadron Collider at CERN.

was given by the CERN Council. It is designed to provide proton-proton collisions with unprecedented luminosity $\mathcal{L} = 10^{34} cm^{-2}s^{-1}$ and a centre-of-mass energy of 14 TeV, where theoretical predictions hint at a rich field of new physics. In addition to p-p operation, the LHC will be able to collide heavy nuclei (Pb-Pb) with with an energy of 2.8 TeV per nucleon and a peak luminosity of $\mathcal{L} = 10^{27} cm^{-2}s^{-1}$.

Protons are chosen as accelerated particles to reduce the energy loss due to synchrotron radiation, which is proportional to the fourth power of E/m. Compared to electrons, the energy loss is reduced by a factor of $\mathcal{O} = 10^{12}$. To achieve the design luminosity for proton-proton collisions, two beams, each with 2808 bunches, are filled in the LHC ring. Each bunch consists of 1.15×10^{11} protons. The bunches are separated by a gap of 25 ns. Other bunch spacing schemes are in consideration for the early stage. To keep the particles on track, the LHC uses 1232 superconductive dipole magnets for the beam guidance that provide a field of about 8.3 T, which is the limit of currently available technologies. The temperature of these dipoles is kept below 1.9 K by a liquid helium cooling system. The machine parameters for proton-proton operation are summarized in Tab. 3.1.

Circumference	26658 m
Centre-of-mass energy	7 TeV
Dipole field at 7 TeV	8.33 T
Radius of curvature	2812 m
Design luminosity	$10^{34} cm^{-2} s^{-1}$
Protons per bunch	1.15×10^{11}
Number of bunches	2808
Collision rate	40.08 MHz
DC beam current	0.58 A
Stored energy per beam	362 MJ
Stored energy in magnet	11 GJ
Operating temperature	1.9 K

Table 3.1: Some of the LHC design parameters for proton-proton operation [4].

A schematic overview of the accelerator complex is given in Fig. 3.2. The acceleration is performed in several stages. The proton injection starts at the duo-plasmatron, which is the proton source. A linear accelerator (LINAC) boosts the protons to an energy of 750 KeV using Radio Frequency Quadruples. In case of the LHC a 30 μs pulse is ejected into the Proton Synchrotron Booster (PSB) which increases the energy to 1.4 GeV. Then the protons will be accelerated up to 450 GeV by the Super Proton Synchrotron (SPS), and they will finally be injected into the LHC. In the LHC ring, build in the former 26.7 km circumference LEP tunnel, the acceleration continues until the protons reach their final energy of 7 TeV. More details about the LHC machine can be found at [52, 53].

At the four interaction points (where the counter rotating beams are brought to collision) five experiments have been set up (Fig.3.2). ATLAS [54] and CMS [55] are two complementary multipurpose experiments, designed for the same physics

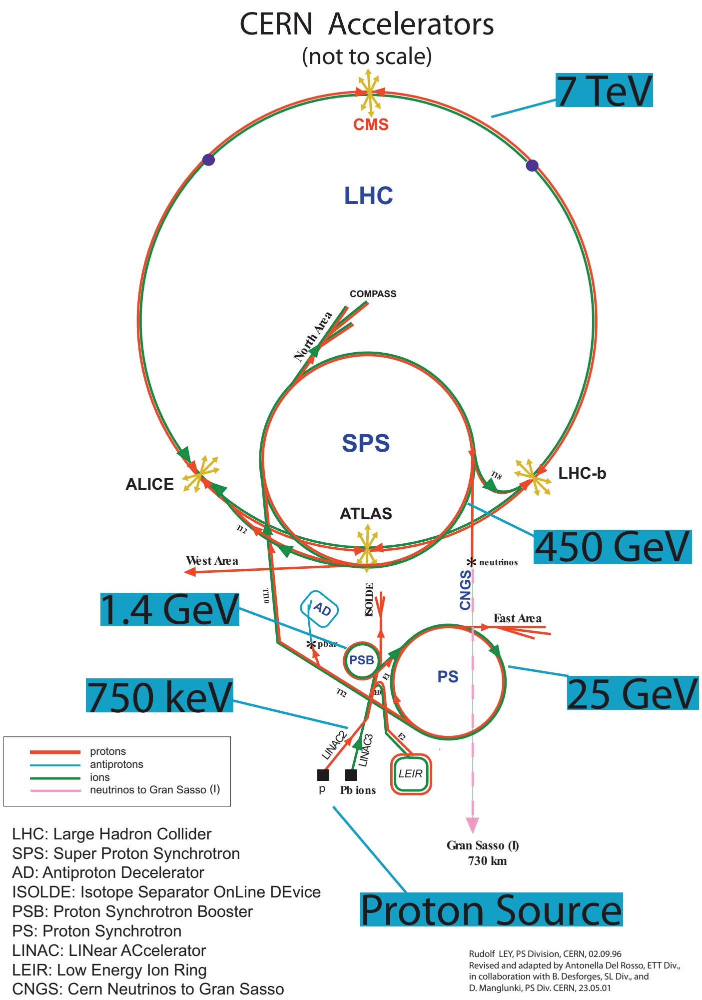

Figure 3.2: A schematic view on the acceleration complex at CERN.

program. This redundancy increases not only the accumulated cross sections in the combined research, but more importantly, since both experiments are realized in complementary technologies, provides a natural way of checking the findings of each experiment. Another two detectors devoted specific topics: ALICE [56] to heavy ions and LHCb [57] to b-physics. ALICE, LHCb and TOTEM [58] are specialized experiments. The TOTEM experiment will measure the total *pp* cross-section with the luminosity-independent method and study elastic and diffractive scattering.

An (non-exhaustive) overview of the physics program at LHC is given below, while the CMS experiment is described in the next section.

3.2 Physics with the LHC

The LHC will provide proton-proton collisions at the highest centre-of-mass energy of 14 TeV and large luminosity to compensate for the low cross section of interesting processes. Cross sections of various Standard Model processes in $p\bar{p}$ and *pp* collisions as a function of energy are compared in Fig. 3.3, as well as the expected event rates at the LHC [59]. The Higgs cross section increases steeply with the centre-of-mass energy, while the total cross section (i.e. the background) remains almost constant. This leads to use the highest possible centre-of-mass energy.

In high-energy inelastic proton-proton collisions the interaction involves the partons inside the proton. Therefore the accurate knowledge of the Parton Distribution Functions (PDF) of quarks, anti-quarks and gluons is mandatory for the interpretation of the data. The region of the fractional parton momentum x and the momentum transfer Q^2 interesting for LHC physics is shown in Fig. 3.4, comparing to the area investigated by fixed target experiments and at the electron-proton collider HERA [59]. The fact that the two partons interact with unknown energies has two fundamental consequences. First of all the total energy of an event is unknown, because the proton remnants, that carry a sizeable fraction of the proton energy, are scattered at small angles and are predominantly lost in the beam pipe, escaping detection. Moreover, the centre of mass may be boosted along the beam direction. Experimentally, it is therefore not possible to define the total and missing energy of the event, but only the total and missing transverse energies.

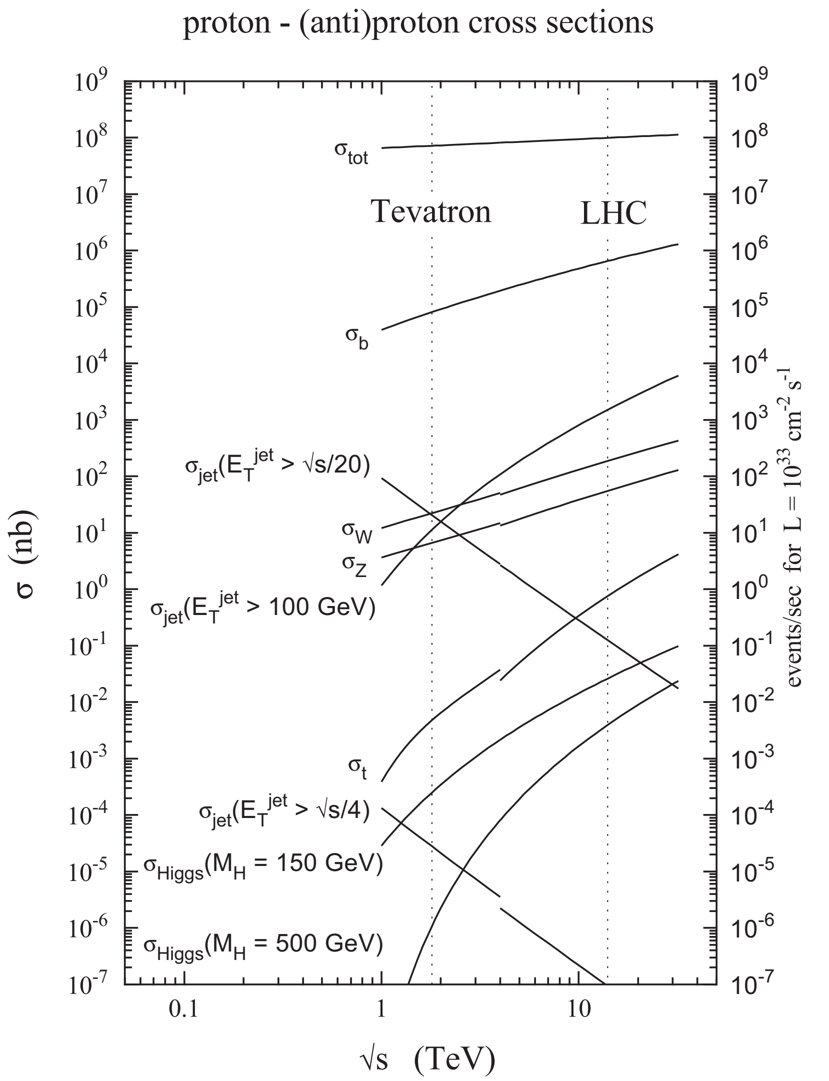

Figure 3.3: Expected cross sections and event rates of several processes as a function of the centre-of-mass energy of hadron collisions [59]. Discontinuities are due to the difference between $p\bar{p}$ for Tevatron and pp for LHC.

Standard Model Physics With the large cross sections in Fig. 3.3, for most measurements of standard model physics the statistical uncertainty will be very small. High statistics control samples will allow a good understanding of the detector response, thus reducing the systematic uncertainty. Several precision electroweak

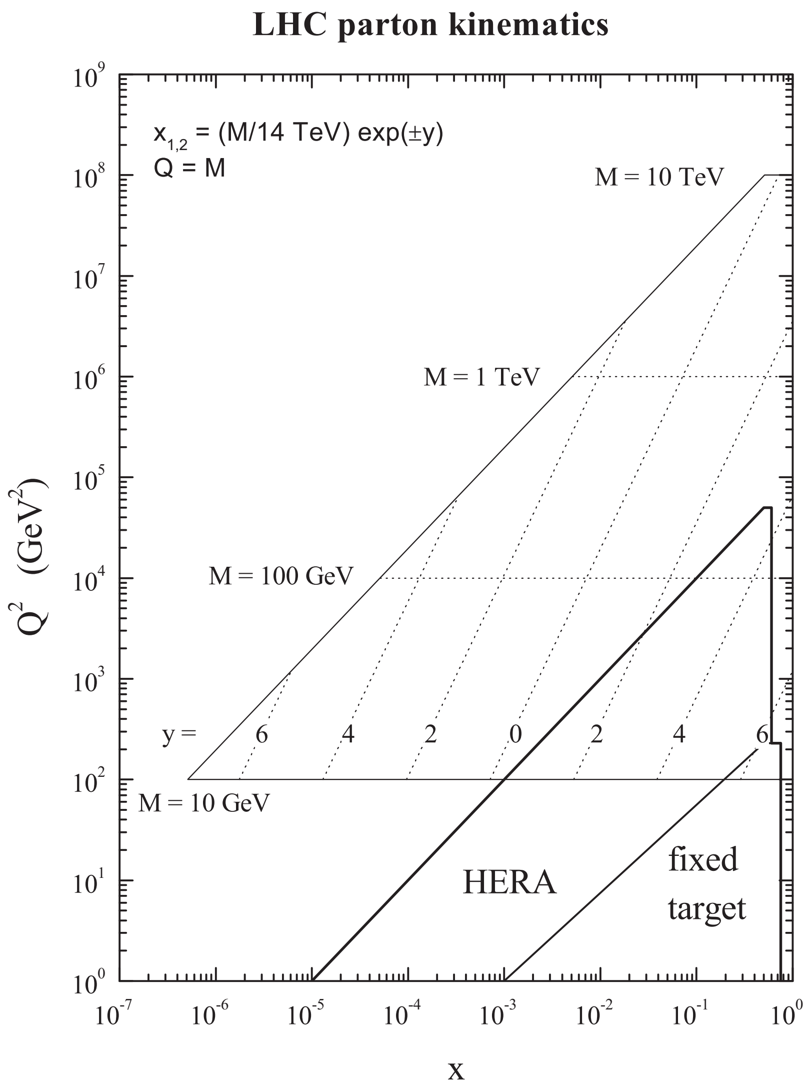

Figure 3.4: Values of x and Q^2 probed in the production of an object of mass M and rapidity y at the LHC, $\sqrt{s} = 14TeV$ [59].

measurements will be possible with the LHC, including:

- W/Z production cross section;
- Measurement of the W/Z and Top Mass;
- Drell-Yan production of lepton pairs;

- B meson physics and CP Violation;
- Diffraction physics.

Higgs Search The Higgs boson has been directly searched for at the LEP experiments and a Higgs mass below 114 GeV is excluded at the 95% confidence level. Also an indirect search has been performed, in which the consistency between the precise measurements of the electroweak sector of the SM and a given Higgs mass is tested. The result is shown in Fig. 3.5 and it can be concluded that a SM Higgs boson mass should be below 182 GeV 95% confidence level [60], if the direct search at LEP is included. If Higgs bosons are produced at the LHC, the branching ratios of the decay modes of the SM Higgs boson will depend on the Higgs mass (see Fig. 3.6(a)). The production cross sections at the LHC for the various production mechanisms as a function of mass is shown in Fig. 3.6(b).

SUSY Search If R-parity is conserved, then the produced supersymmetric partner particles (SUSY) cannot decay completely to SM particles. If lightest and hence stable SUSYs is neutral, it will leave the detector undetected, similar to the SM neutrinos, leading to large missing transverse energies. This clear signature in combination with the large expected cross sections for SUSY processes would typically lead, already with few fb^{-1} of data, to indications of R-parity conserving SUSY at the TeV level. The missing energy measurement requires good hermeticy of the hadron calorimeter.

The LHC will restart its operation in September 2009, and will soon enable us to analyze the highest energy collisions. The first physics run will be at centre-of-mass energy of 10 TeV with low luminosity phases, where the proton bunches will collide every 50 ns and each bunch consists of 5×10^{10} protons. The expected integrated luminosity of the 10 month run trough 2009-2010 is about 200 pb^{-1}.

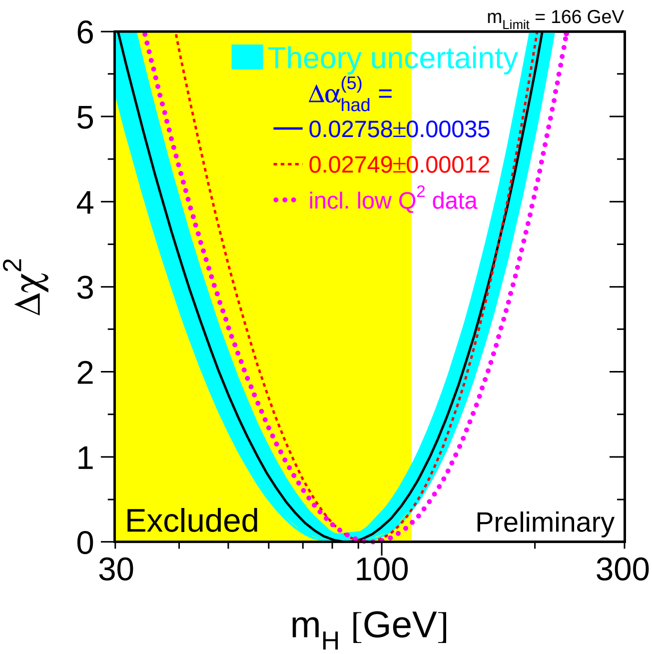

Figure 3.5: χ^2 of a SM fit to electroweak measurements as a function of the Higgs boson mass [60]. The yellow region is excluded by the direct search.

3.3 The Compact Muon Solenoid

The Compact Muon Solenoid (CMS) [62] is located in Point 5 of the LHC. It's a multi-purpose detector which will be able to investigate a wide range of potential new physics that might emerge at the LHC energy. The detector requirements for CMS to meet the goals of the LHC physics programme can be summarized as follows:

- Good muon identification and momentum resolution over a wide range of momenta and rapidity, good dimuon mass resolution ($\sim$ 1% at 100 GeV).
- Good momentum resolution and reconstruction efficiency for charged particles in the inner tracking system. Good triggering and offline tagging efficiencies for τ's and b-jets.

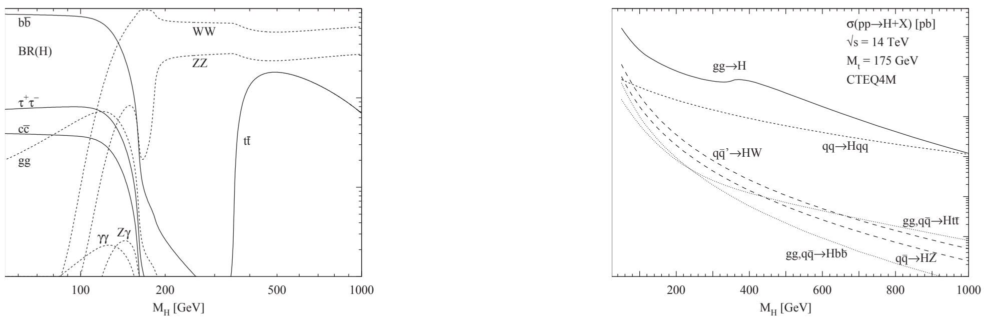

(a) (b)

Figure 3.6: Left: branching ratios of the dominant decay modes of the SM Higgs boson as a function of the Higgs mass. Right: production cross sections at the LHC for the various production mechanisms as a function of the Higgs mass. From Ref. [61].

- The electromagnetic calorimeter must have a high resolution for proper dielectron and diphoton mass resolution in a wide geometric coverage. Furthermore good π^0 rejection, and efficient photon and lepton isolation at high luminosities has to be provided.

- Good missing transverse energy and dijet mass resolution requires the hadronic calorimeter to have an almost 4π coverage and a fine lateral resolution.

The general layout of the CMS detector is presented in Fig. 3.7. The detector has the classical layered structure of central detectors in high energy physics: an inner tracker, an electromagnetic calorimeter, a hadronic calorimeter and a muon system (from the interaction point to the outermost layer). The overall dimensions are 22 m in length and 15 m in diameter with a total mass of 12500 t. A more detailed overview on the CMS experiment is given in the references [55, 63].

The coordinates system in CMS are as follows: The origin of the coordinate system is situated at the nominal interaction point. The z-axis along the beam

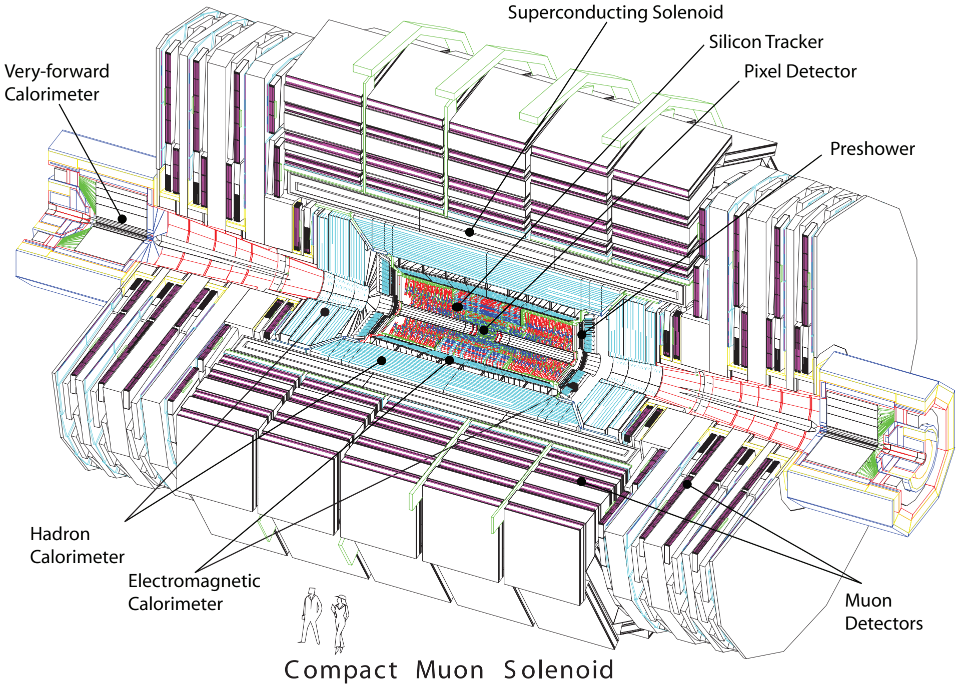

Figure 3.7: A perspective view of the CMS detector at at the Large Hadron Collider at CERN.

direction, the x-axis points radially inward to the centre of the LHC ring, and the y-axis directed upward, orthogonally to the z and x axes. The azimuthal angle ϕ is measured in the x-y-plane from the x-axis. The pseudorapidity η is defined as $\eta = -ln(tan(\theta/2))$ where θ s the polar angle with respect to the beam axis in the y-z-plane. The use of pseudorapidity instead of the polar angle is motivated by the fact that the difference in pseudorapidity between two particles is invariant under Lorentz boosts along the beam axis.

Tab. 3.2 summarized the characters of the CMS sub-detectors. The transverse cross section of the barrel part is presented in Fig. 3.8. The principle of detection of charged and neutral particles in the various sub-detectors is shown. All charged particles leave signals in the inner tracking system. Electrons and photons deposit their energy in the electromagnetic calorimeter. Charged Hadrons ($K^{\pm}$, $\pi^{\pm}$...) and neutrons deposit their energy in the hadronic calorimeter. Muon is a particle which passes through calorimeters without interacting much, but which leaves a track of its passage in the muon chambers. Neutrinos, barely interacting, will escape from all direct detections. While adding the transverse momenta of all the particles detected by the detector, one can determine the imbalance of energy in the transverse plane, so called the missing transverse energy E_T^{miss}.

Name	Type	Particle	$\|\eta$ coverage	Technology
Tracker	track	charged	[0 - 2.5]	
$*$ pixels			[0 - 2.5]	silicon pixels
$*$ strips			[0 - 2.5]	silicon strips
ECAL	calo	$e^{\pm}/\gamma/jets$	[0 - 3.0]	$PbWO_4$
$*$ EB			[0 - 1.479]	
$*$ EE			[1.479 - 3.0]	
$*$ ES			[1.653 - 2.06]	
HCAL	calo	jets	[0 - 3.0]	Cu + scint
$*$ HB			[0 - 1.4]	
$*$ HO			[0 - 1.26]	
$*$ HE			[1.3 - 3.0]	
Muon	track	$\mu^{\pm}$	[0 - 2.4]	
$*$ MB			[0 - 1.2]	DT + RPC
$*$ ME			[1.0 - 2.4]	CSC + RPC

Table 3.2: CMS detector.

3.3.1 The Magnet

The super-conducting magnet in CMS, which houses the tracker, the electromagnetic, and the hadronic calorimeter, is the biggest solenoidal superconducting magnet in the world [3,4,5,6]. The calculated CMS magnet filed map is shown in

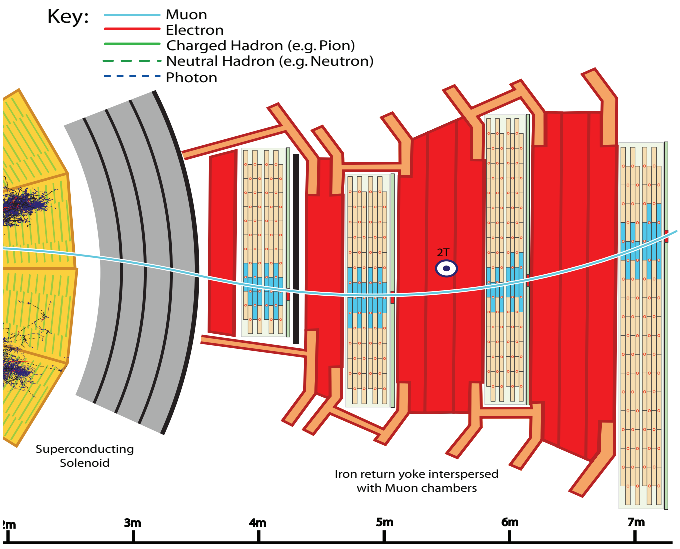

Figure 3.8: Transverse slice through CMS showing particles incident on the different sub-detectors.

Fig. 3.9. The magnet achieves a magnetic field of 3.8 T in the free bore of 6 m in diameter and 12.5 m in length. The energy stored in the magnet is about 2.6 GJ at full current. The superconductor is made of four layers NbTi. In case of a quench, when the magnet looses its super-conducting property, the energy is dumped to resistors within 200 s.

The magnet return yoke of the barrel has 12-fold rotational symmetry and is assembled of three sections along the z-axis; each is split into 4 layers (holding the muon chambers in the gaps). Most of the iron volume is saturated or nearly saturated, so the field in the yoke is just a few times lower than the field in the central volume. More detailed information can be found in reference [64].

3.3.2 Inner tracking system

The tracker shown in Fig. 3.10 is located closer the interaction point. Therefore, the tracker has to be operated in a region with a very high particle flux. Per bunch crossing 1000 charged particles will hit the tracker. Thus, a hit rate of 1 MHz/mm^2 is expected at a radius of 4 cm. Hence, The tracker must be able to operate without

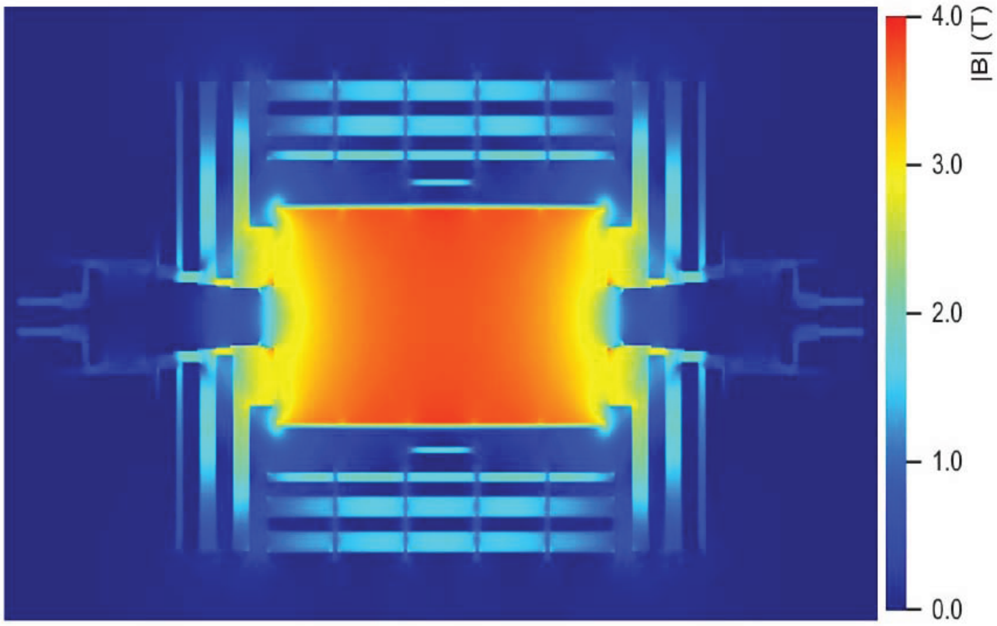

Figure 3.9: The calculated magnetic field in CMS for a central field of 3.8 T. The field is plotted for a cross-section of the CMS detector in the horizontal plane at the level of the beam line [talk].

degrading its performances in the hard radiation environment of LHC and it has to comply with severe material budget constraints, in order not to degrade the excellent energy resolution of the electromagnetic calorimeter.

It is designed to determine the interaction vertex, measure with good accuracy the momentum of the charged particles above 1 GeV/c, and identify the presence of secondary vertices for heavy flavour identification. The CMS collaboration has adopted silicon technology for the whole tracker. The tracker consists of two parts. The inner tracker is a silicon pixel detector with a total surface of 1 m^2 and 66 million pixels. It is surrounded by silicon strip sensors in the outer region covering a total area of 200 m^2. The CMS inner tracker system is the largest silicon detector ever build. The dimensions of the tracker in length and diameter are 5.8 m and 2.5 m. Thus, its acceptance is up to $|\eta| < 2.5$. The whole volume is pervaded by a homogeneous magnetic field about 4 T. More information can be found in reference [65, 66].

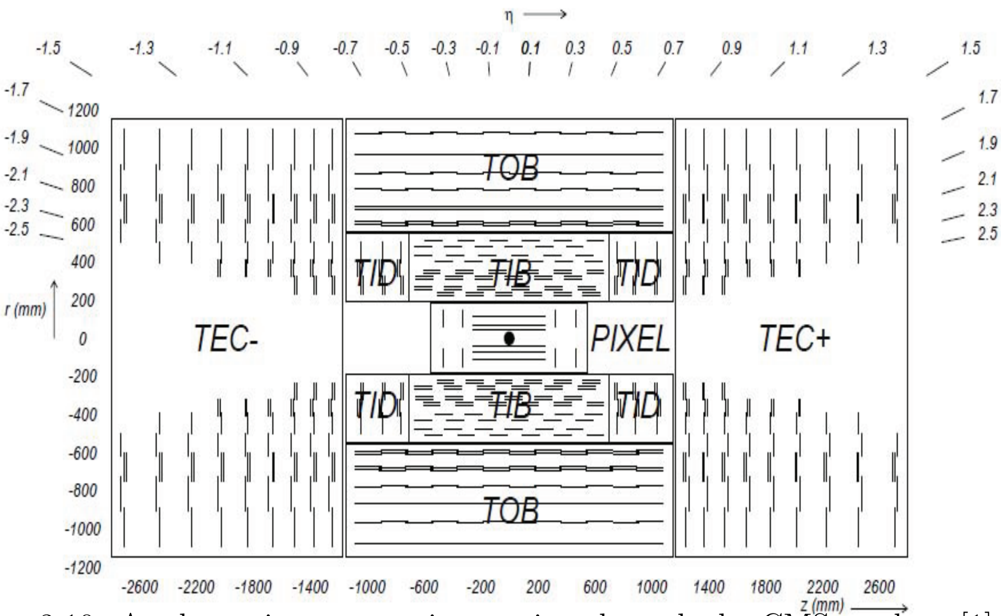

Figure 3.10: A schematic cross section section through the CMS tracker: [1] Pixel Barrel and End Caps, [2] Tracker Inner Barrel (TIB), [3] Tracker Inner Disks (TID), [4] Tracker Outer Barrel (TOB), [5] Tracker End Caps (TEC) [CMS].

Silicon Pixel Tracker

The pixel detector consists of three barrel layers and two end-cap disks at each side (Fig. 3.11). The barrel layers are located at radii of 4.4, 7.3 and 10.2 cm around the interaction point with a length of 53 cm. On each side of the barrel, extending from 6 to 15 cm in radius, two discs are placed at $|z|$ = 32.5 cm and 46.5 cm. Therefore, for every charged particle with $|\eta| < 2.5$ hitting the tracker, three high precision space points will be measured. The pixels have a cell size of $100 \times 150 \mu m^2$. The presence of high magnetic field causes a noticeable drift of the electrons (and a smaller drift for the holes) from the ionization point along the track with a Lorentz angle of about 32^o. This leads to a charge sharing between pixels which, using an analog readout, can be exploited to considerably improve the resolution, down to about 15 μm.

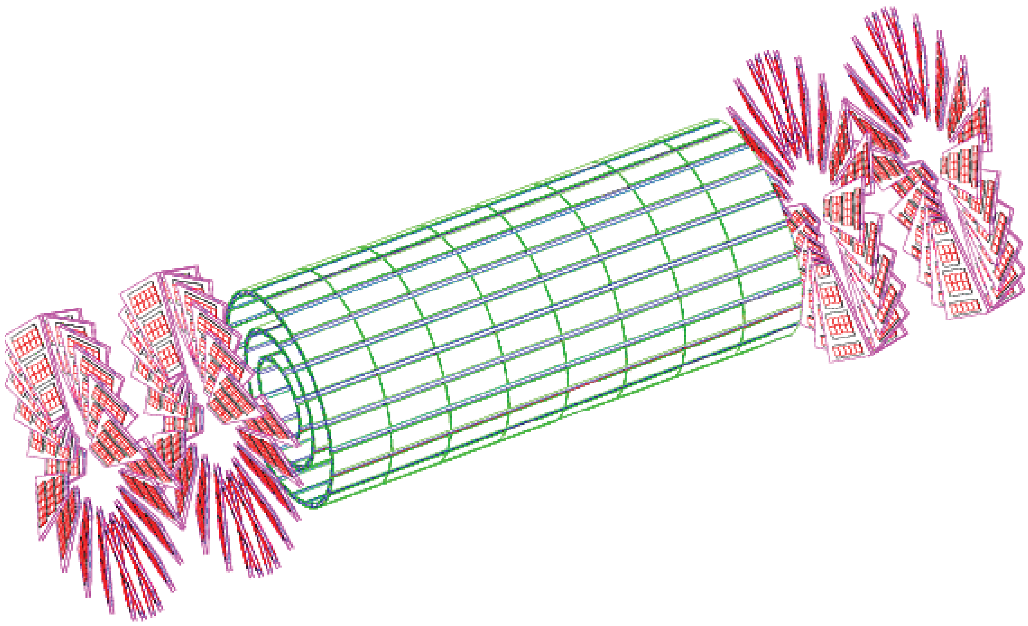

Figure 3.11: The inner pixel detector. The three barrel section and the two disks of the end-cap with blades disposed in a turbine-like shape are visible. The configuration shown here corresponds to the one for the high luminosity running. [CMS].

Silicon Strip Tracker

The Silicon Strip Tracker (SST) (see Fig. 3.10) surrounds the pixel tracker. The barrel and disk modules have the readout strips oriented along the z and radial directions respectively, allowing the readout of the $r\phi$ coordinate. The inner tracker is made of 4 barrel layers, the two innermost are double sided, and the end-caps count 3 disks each. The outer tracker consists of 6 layers in the barrel (the two innermost are double sided) while the end-caps are made of 9 layers (the first, the second and the fifth are double sided). On the whole the silicon trackers is made of about 10 millions of channels for an active area close to 198 m^2.

Since the hit density decreases with distance from the interaction point, it is possible to increase the strip length and pitch while keeping the occupancy at the level of 13%. The strip length varies from 9 cm to about 20 cm and the strip pitch is in the range of 80 μm to 205 μm. The larger cell sizes in the outer parts of the tracker help limit the number of needed readout channels to about 107 strips on 15148 detector modules, covering a tracking volume of approximately 25 m^3. A position resolution in the direction parallel to the strips is achieved in selected layers by mounting two strip modules back-to-back at a stereo angle of 100 mrad. The tracker layout guarantees at least 9 hits per track in the pseudorapidity region of $-2.3 < \eta < 2.3$, including at least 4 hits in stereo layers. The expected transverse momentum resolution for 100 GeV-muons is about 12% at $|\eta| < 1.6$ and better than 10% up to $|\eta| = 2.5$.

The silicon micro-strips are essentially p-n diode structures, consisting of an n-type substrate with a p^+-type layer facing the interaction point and an n^+-type backing plate. During operation, they are sufficiently reverse-biased so as to fully deplete them. When a charged particle passes through a micro-strip, electron-hole pairs generated in the depletion region are swept out and a current signal is produced.

Name	No. detectors	thickness (μm)	mean pitch (μm)
TIB	2724	320	81/118
TOB	5208	500	81/183
TID	816	320	97/128/143
TEC	2512	320	96/126/128/143
TEC(2)	3888	500	143/158/183
Total	15148		

Table 3.3: Detector types in the silicon tracker [63].

Tracker Alignment

The true position of the tracker modules is immanent for the high-precision spatial resolution measurements. Deviations are caused by assembly concision, deformations due to cooling and stress from the magnetic field. Therefore, three methods are used for the tracker alignment. The geometry was determined during assembly to an accuracy of 80 to 150 μm. An infrared laser system is used for continuous monitoring of the position of selected tracker modules. The final alignment is done with tracks from well known physics processes, e.g. cosmic muons, or di-muons from J/ψ, Υ and Z...

3.3.3 Electromagnetic Calorimeter

The electromagnetic calorimeter (ECAL) [67] situated around the tracking system, is supposed to make a precision energy measurement of electromagnetic interacting particles like electrons and photons. The main requirements are a good energy resolution and a fine granularity for a precise spatial resolution. Therefore, a hermetic homogeneous calorimeter out of lead tungstate ($PbWO_4$) crystals is used. The crucial properties of lead tungstate crystal are, besides a high density of 8.28 g/cm^3, a short radiation length of 0.89 cm and a small Molière radius of X_0=2.2 cm. When particles pass through the calorimeter, the crystals produce blue-green scintillation light in fast, short, well-defined photon showers. The scintillation time of these crystals is of the same order as the LHC bunch crossing time. 80% of the light is emitted within 25 ns. The amount of light is proportional to the energy deposit of the particle in the crystal, but the yield is relatively low so that highly sensitive photodetectors are necessary to measure and convert it to an electrical signal.

Fig. 3.12 is the geometric layout and Fig. 3.13 shows the longitudinal view of a quarter of the CMS detector, showing the location of the electromagnetic calorimeter.

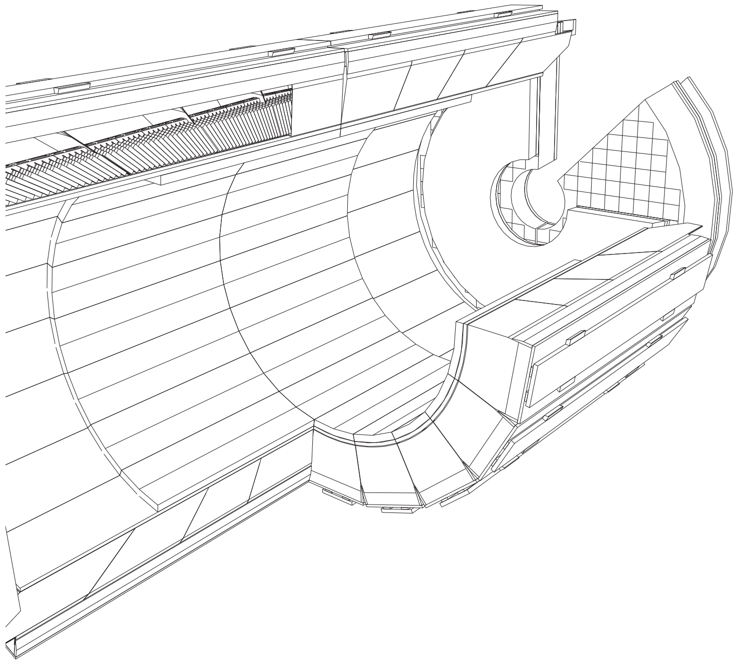

Figure 3.12: Layout of the CMS electromagnetic calorimeter showing the arrangement of crystal modules, supermodules and endcaps, with the preshower in front [67].

ECAL Barrel The barrel part of the ECAL (EB) is made up of 36 supermodules, weighs 67.4 t and covers the pseudorapidity range $|\eta| < 1.479$. The segmentation is 360-fold in ϕ and (2×85)-fold in η, resulting in a total of 61200 crystals. The crystal cross-section corresponds to approximately 0.0174×0.0174 in η-ϕ or 22×22 mm^2 at the front face of crystal, and 26×26 mm^2 at the rear face. The crystal length is 230 mm corresponding to 25.8 X_0.

ECAL Endcap The ECAL endcaps (EE) cover the pseudorapidity range from 1.479 to 3.00. One supermodule is formed out of 25 crystals. The face cross section here is 28.62×28.62 mm^2. Their length is 220 mm, which corresponds to a radiation length of 24.7 X_0. Due to the strong and varying magnetic field, the read-out must

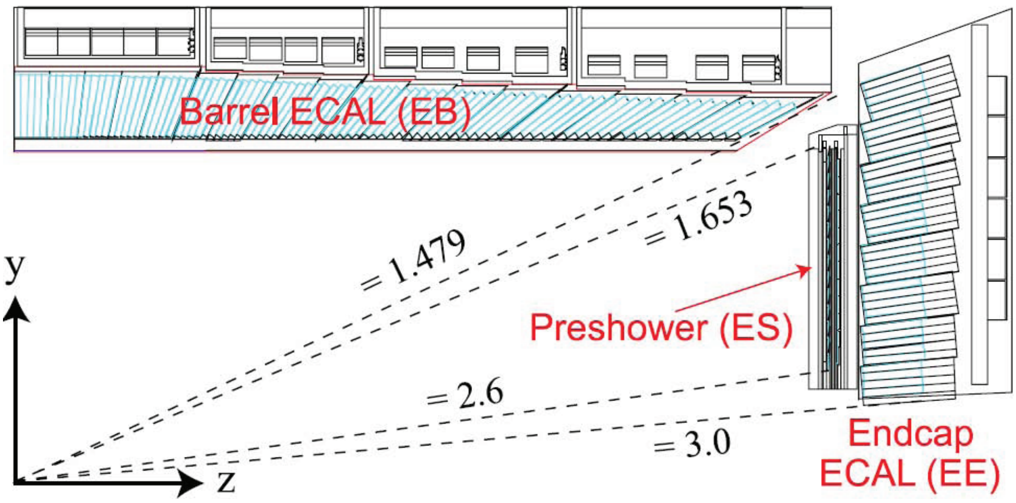

Figure 3.13: Longitudinal view of a quarter of the CMS detector, indicating the location of the electromagnetic calorimeter [67].

be different: Vacuum Photo Triodes (VPT) are used.

Preshower detector For a better spatial precision a preshower detector (ES) sits in front of the endcaps. The main aim is the identification of neutral pions, decaying into two closely-spaced low energy photons. As the preshower has a much finer granularity, it is possible to distinguish between those two low energy photons and single high energy ones. The preshower covers the ranges from $1.656 < |\eta| < 2.6$ and has a total thickness of 20 cm, which corresponds to a radiation length of 3 X_0. It is composed of two detector layers, each with lead radiators followed by silicon strip sensors.

The expected energy resolution of the ECAL barrel and the endcaps is given in Tab.3.4. The total resolution is affected by several contributions and can be calculated with

$$(\frac{\sigma}{E})^2 = (\frac{S}{\sqrt(E)})^2 + (\frac{N}{E})^2 + C^2 \tag{3.1}$$

where S is the stochastic fraction depends on event-to-event fluctuations in the lateral shower, photo-statistics, and fluctuations in the energy deposited in the preshower absorber. C is the constant term is caused by the non-uniformity of the light collection, errors on the inter-calibration among the modules, and leakage of energy from the back of the crystal. The noise term N is composed of electronic, digitization, and pileup noise.

Contribution	Barrel ($\eta = 0$)	Endcap ($\eta = 2$)
stochastic term S	2.7%	5.7%
constant C	0.55%	0.55%
noise (low luminosity) N	155 MeV	770 MeV
noise (high luminosity) N	210 MeV	915 MeV

Table 3.4: The energy resolution of the ECAL barrel and endcap [67].

3.3.4 Hadron calorimeter

The hadron calorimeter (HCAL) [68] situated around the ECAL, measures the energy of hadronic particle jets and determines the missing transverse energy. It also helps in the identification of electrons, photons and muons.

Fig. 3.14 gives a schematic overview on the HCAL. The dashed lines are at fixed η values. The hadron calorimeter barrel and endcaps sit behind the tracker and the electromagnetic calorimeter as seen from the interaction point. The hadron calorimeter barrel is radially restricted between the outer extent of the electromagnetic calorimeter (R = 1.77 m) and the inner extent of the magnet coil (R = 2.95 m). This constrains the total amount of material which can be put in to absorb the hadronic shower. Therefore, an outer hadron calorimeter or tail catcher is placed outside the solenoid complementing the barrel calorimeter. Beyond $|\eta| = 3$, the forward hadron calorimeters placed at 11.2 m from the interaction point extend the pseudorapidity coverage down to $|\eta| = 5.2$ using a Cherenkov-based, radiation-hard technology.

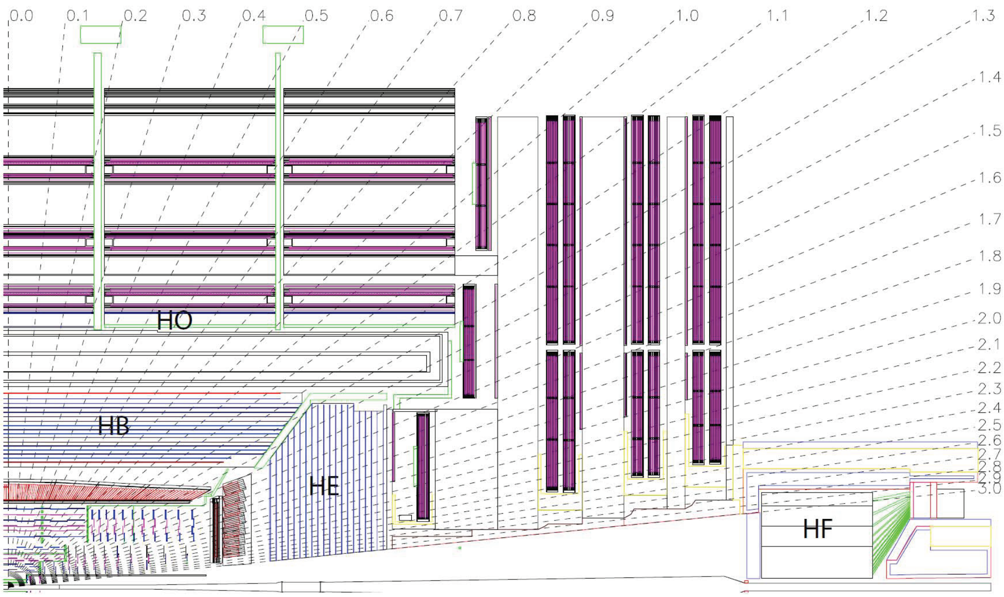

Figure 3.14: Longitudinal view of a quarter of the CMS detector, showing the location of the hadron calorimeter [68].

HCAL barrel The hadron calorimeter barrel (HB) consists in two halves, each subdivided into 18×20^{o} wedges in ϕ. The absorber is mostly brass (70 % Cu and 30 % Zi) with a thickness of at least 50.5 mm. Seventeen active plastic scintillating plates ($1 \times 9mm + 16 \times 3.7mm$) are interleaved between the absorbers, corresponding to $\Delta\eta \times \Delta\phi = 0.087 \times 0.087$. This leads to 2×32 HB towers. The HB energy resolution is $\sim 100\%/\sqrt{E}$ with detection planes parallel to the beam pipe.

HCAL endcaps The two hadronic endcap calorimeters (HE) have a petal structure perpendicular to the beam pipe, with some overlap with the HB. Its 18-fold segmentation provides a coverage ranging from 5^{o} to 20^{o} in ϕ, as η increases. Each HE is made of 19 scintillator planes with a thickness of 3.7 mm interspersed in 78 mm brass absorbers. HE has 2304 towers and its energy resolution is estimated to $\sim 150\%/\sqrt{E}$.

HCAL outer Covering almost the same region as the HB, the outer barrel calorimeter (HO) is located behind the solenoid. It is subdivided in z into 5 rings with a 2.54 m radius, and 12 sectors in ϕ. It is made of 1 or 2 layers of 10 mm scintillator planes, depending on the pseudorapidity, 2 layers for $|\eta| < 1.305$ and only 1 above 1.305. However, HO coverage is not complete in ϕ, due to the 12×75 mm holes for services.

HCAL forward For the construction of the Hadron Forward (HF) steel is selected as absorber. The collection of the energy is accomplished using quartz fibre emitting Cerenkov light, a technology which is preferred to plastic because of its greater radiation tolerance. Additionally, relatively faster phototubes are selected in the HF compartment instead of hybrid photodiodes, that collect the light in the HB and HE.

3.3.5 Muon System

As the very name of the experiment specifies it, the muon measurement is a central part of cms, due to its unique signature. It offers many possibilities for calibration and analysis. The Muon System relies on the combination of three types of gaseous detectors. Like other sub-detectors, the muon system (see Fig.3.15) is divided into a barrel geometry (MB) and two endcaps (ME), as depicted in Fig. 4.6. It covers 25, 000 m^2 with about 1, 000, 000 channels. While drift tubes (DT) are deployed only in the barrel region (low neutron induced background) and cathode strip chambers (CSC) in the endcaps (higher neutron induced background, large muon rates and intense transverse magnetic field), resistive plate chambers (RPC) complement the measurement in all the muon system thanks to their high rate ability and time resolution. More information is given in reference [69].

The muon system is capable of providing extremely pure muon sample with no loss and identifying narrow physics signal peaks over backgrounds. The muon system (combined with the tracker) can identify muons with high efficiency and

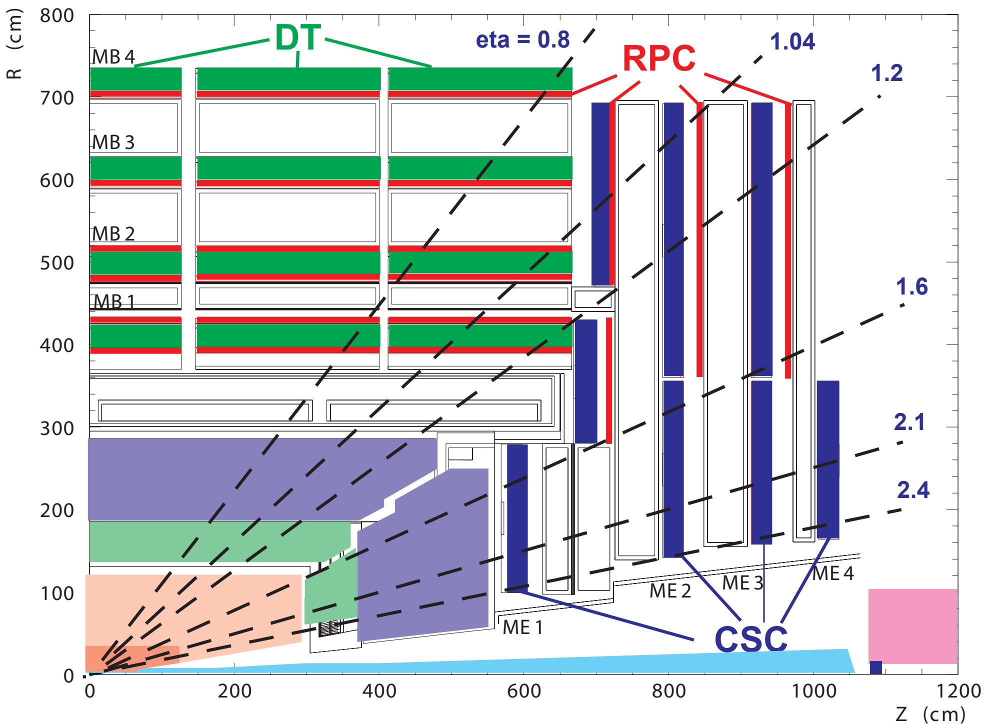

Figure 3.15: Longitudinal view of one quarter of the CMS muon system [63]. The RPC system is limited to $|\eta| < 1.6$ in the endcap, and for the CSC system only the inner ring of the ME4 chambers have been deployed.

with good momentum resolution in $|\eta| < 2.4$. The momentum resolution is limited by the bending angle measurement which depends on the accuracy of the tracking and multiple scattering. The resolution is directly proportional to the square root of the amount of material in the muon system in units of X_0 (radiation length) and inversely proportional to the magnetic field. For high p_T (~ 1 TeV) the momentum resolution is proportional to the spatial resolution of the muon chambers. Up to the last muon station the thickness of the absorber is 16 interaction lengths. Good muon identification is achieved by absorption of charged particles before the muon system in ECAL and HCAL, and in the muon system by the iron yoke. Moreover, the muon system is able to measure the charge of the muons up to about 1 TeV. The muon system can withstand the radiation environment, high rate interaction background of the LHC, and strong magnetic field in the iron yoke.

An important issue for the muon system is its alignment, both internally and with respect to the inner tracker. The misalignment originates in imperfect assembly, temperature instabilities or deformations related to the magnetic field. It is important to monitor the alignment, as the measurement of muons is based on the combination on data from muon chambers and from the tracker. While for high p_T muons the momentum measurement depends on the bending power of the magnet and is limited by the multiple scattering in the material in front of the first muon station, low p_T muons are observed with a much better resolution by the tracker.

3.3.5.1 Drift tube system

In the barrel region, where the particle rate is low and the magnetic field is well contained in the iron plates of the return yoke, drift chambers with standard rectangular drift cells are used.

The drift tubes cover the pseudorapidity region $|\eta| < 1.2$ and are organized into 4 stations interspersed among the layers of the flux return plates, named MB1, MB2, MB3 and MB4 as shown in Fig.3.16. The first and the fourth station are mounted on the inner and outer face of the yoke; the remaining two are installed in slots within the iron plates.

The first 3 stations each contain 8 chambers, in 2 groups of 4, which measure the muon coordinate in the $r - \phi$ bending plane, and 4 chambers which provide a measurement in the z direction, along the beam line. The fourth station does not contain the z-measuring planes. The 2 sets of 4 chambers in each station are separated as much as possible to achieve the best angular resolution. The drift cells of each chamber are offset by a half-cell width with respect to their neighbor to eliminate dead spots in the efficiency. This arrangement also provides a convenient way to measure the muon time with excellent time resolution, using simple meantime circuits, for efficient, standalone bunch crossing identification. The

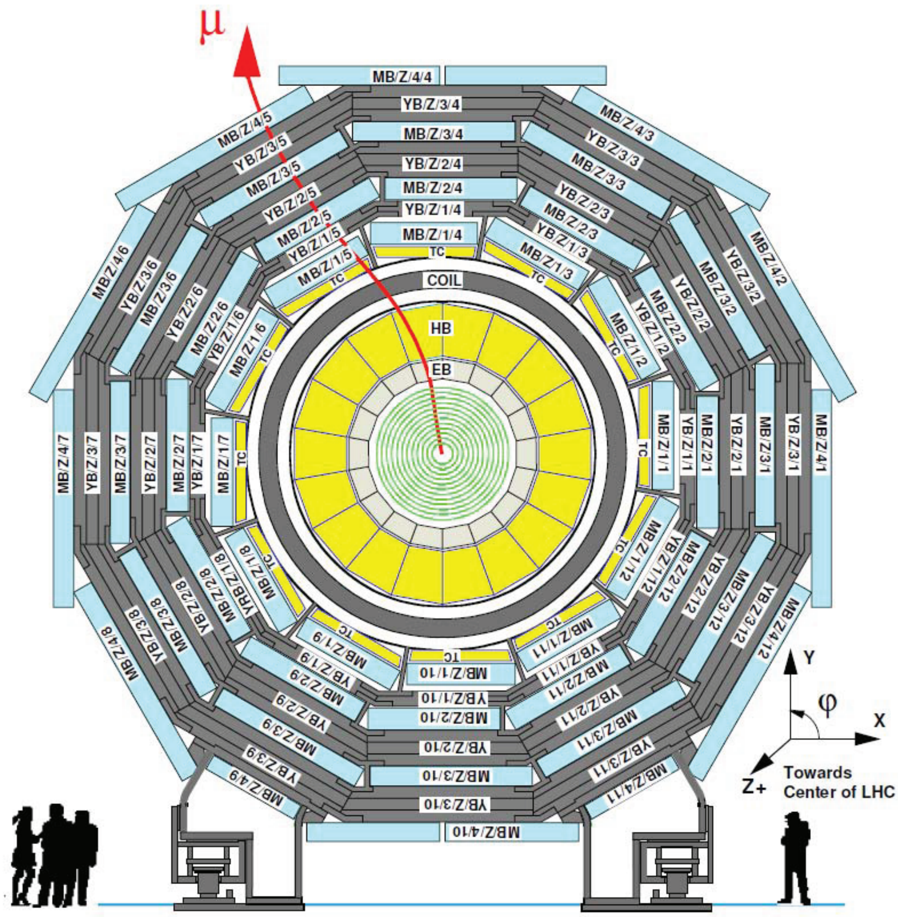

Figure 3.16: Transverse view of the CMS barrel muon detector [55].

number of chambers in each station and their orientation were chosen to provide good efficiency for linking together muon hits from different stations into a single muon track and for rejecting background hits.

3.3.5.2 Cathode strip chambers

In the 2 endcap regions of CMS, where the muon rates and background levels are high and the magnetic field is large and non-uniform, the muon system uses cathode strip chambers . CSC chambers are multi-wire proportional chambers with fast response time, fine segmentation, and radiation resistance, so that they can operate at high occupancy levels and in the presence of a large inhomogeneous magnetic field.

CSC chambers identify muons between $|\eta|$ values of 0.9 and 2.4, and are arranged in four stations placed between the iron disks of the yoke (cf. Fig.3.15). The innermost station consists of three concentric rings, the first (ME1/1) being closer to the interaction point than the other two. The other stations are composed by two disks only. The rings are formed by 18 or 36 trapezoidal chambers, which, with the exception of the outermost ring of ME1, are staggered with a small overlap in ϕ. Chambers are composed of six layers, each consisting of an array of anode wires between two cathode planes. The gap is 9.5 mm thick and is filled with a 30%/50%/20% mixture of $Ar/CO_2/CF_4$. One of the two cathode planes is segmented into strips orthogonal to the wires. The avalanche produced in the gap by a crossing charged particle induces a charge in several adjacent strips, an interpolation of the signals gives a precise spatial measurement. Strips are radial and measure the ϕ coordinate. The orthogonal coordinate (r) is measured by the wires which, to reduce the number of channels, are read out in groups of 5 to 16. The resolution is of the order of $\sim 0.5cm$, to be compared with $\sim 150\mu m$ of the strip measurement.

3.3.5.3 Resistive plate chambers

For improving the ability of muon system trigger and measuring the correct beam crossing time when the LHC reaches full luminosity, a complementary, dedicated trigger system consisting of resistive plate chambers (RPC) was added in both the barrel and endcap regions.

The RPCs provide a fast, independent, and highly-segmented trigger with a sharp p_T threshold over a large portion of the rapidity range ($|\eta| < 1.6$) of the muon system. The RPCs are double-gap chambers, operated in avalanche mode to ensure good operation at high rates. They produce a fast response, with good time resolution but coarser position resolution than the DTs or CSCs. They also help to

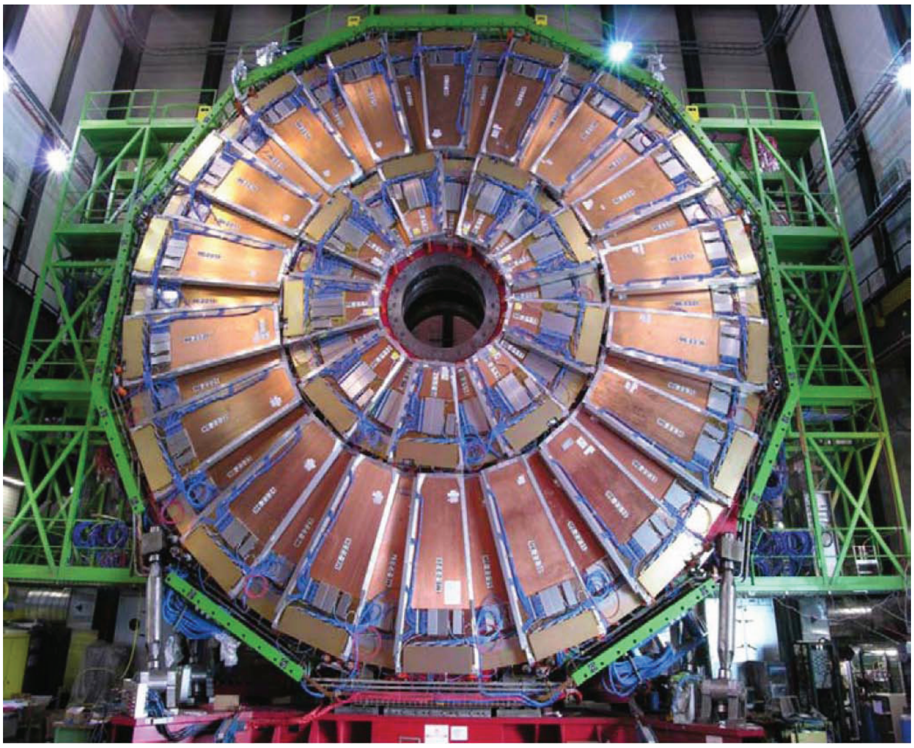

Figure 3.17: The ME2 station of the cathode strip chambers [55].

resolve ambiguities in attempting to make tracks from multiple hits in a chamber.

A total of 6 layers of RPCs are embedded in the barrel muon system, 2 in each of the first 2 stations, and 1 in each of the last 2 stations. The redundancy in the first 2 stations allows the trigger algorithm to work even for low-p_T tracks that may stop before reaching the outer 2 stations. In the endcap region, there is a plane of RPCs in each of the first 3 stations in order for the trigger to use the coincidences between stations to reduce background, to improve the time resolution for bunch crossing identification, and to achieve a good p_T resolution.

3.3.5.4 Performance

In total, muons are measured up to four times. Once in the inner tracking system and tree times in the three parts of the muon system. This leads to an overall good muon reconstruction, which is essential for many physics processes in

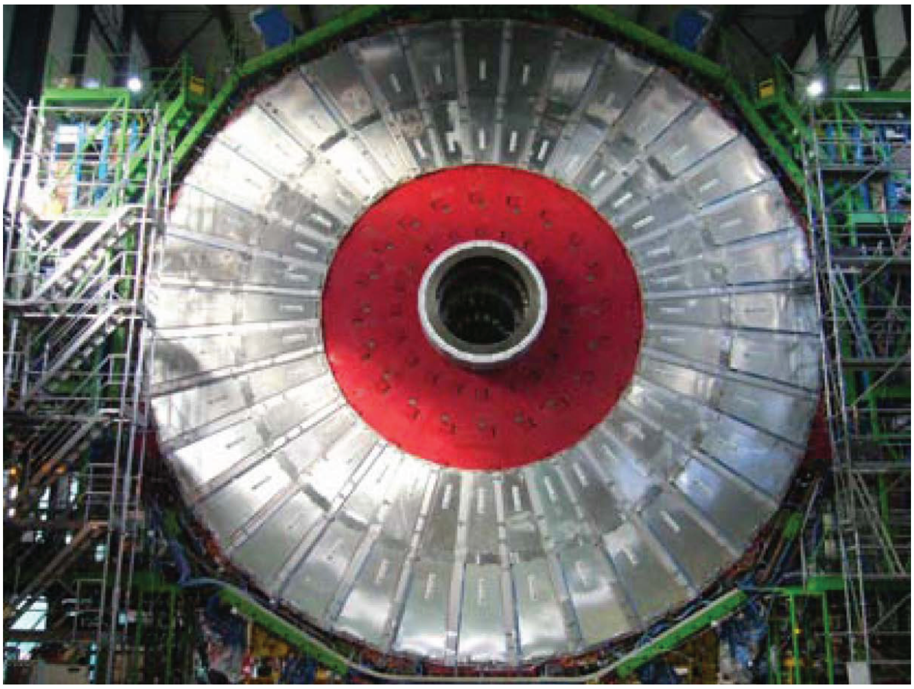

Figure 3.18: The RE2 station of resistive plate chambers on the back side of the YE-1 yoke [55].

the LHC programme.

The muon detector elements cover the full pseudorapidity interval $|\eta| < 2.4$ with no acceptance gaps. Offline reconstruction efficiency of simulated single-muon samples is typically $95 - 99\%$ except in the regions around $|\eta| = 0.25$ and $|\eta| = 0.8$ (the regions between 2 DT wheels) and $|\eta| < 1.2$ (the transition region between the DT and CSC systems), where the efficiency drops.

Due to multiple-scattering in the detector material before the first muon station, the offline muon momentum resolution of the standalone muon system is about 9% for small values of η and p for transverse momenta up to 200 GeV [63]. At 1 TeV the standalone momentum resolution varies between 15% and 40%, depending on η. A global momentum fit using also the inner tracker improves the momentum resolution by an order of magnitude at low momenta. At high momenta (1 TeV) both detector parts together yield a momentum resolution of about 5%. Note that the muon system and the inner tracker provide independent muon momentum measurements; this redundancy enhances fault finding and permits cross-checking between the systems.

A crucial characteristic of the DT and CSC subsystems is that they can each trigger on the p_T of muons with good efficiency and high background rejection, independent of the rest of the detector. The Level-1 trigger p_T resolution is about 15% in the barrel and 25% in the endcap.

3.3.6 Trigger and Data Acquisition system

As discussed in Section 5.1, the LHC is designed to operate at a very high event rate and collision energy, there is neither the space nor detector readout bandwidth available to store all of the data produced. The readout rate is particularly limited by data storage space. Each event in CMS produces approximately 1 MB of processed data and the total data volume produced by the CMS detector is 100 TB per second. This huge amount is too large to be handled by current storage and network solutions and therefore has to be trimmed to more reasonable values through a sophisticated cascaded trigger system. The main challenge is therefore the selection of interesting events among the huge amount of background which has to be reduced to a manageable amount. The event rate which can be recorded for offline processing and analysis is at the order of 150 Hz.

In order to reach this, the CMS trigger and data acquisition system (TriDAQ) [70] comprises two stages of event selection [8, 55, 10]. Fig. 3.19 depicts the architecture of the CMS DAQ and trigger system.

The Level-1 (L1) trigger [70] is primarily hardware-based processing system in order to handle the enormous data volume from the detector and provide a trigger decision in a very short (and guaranteed) time period of $3.2\mu s$. The goal of the system is to reduce the data volume by an average factor of 400 (i.e. to 100kHz).

The Higher Level Trigger (HLT) [71] reduces the rate by a further factor of 1,000 and is dominated by the use of computer farm using a multi-stage iterative approach to reconstruction with a limiting cut-off in allowed processing time. At this level basic tracker information is used, and initial selection based on possible underlying physics events is made. The data produced at this level of filtering is then recorded to disk at approximately 100Hz.

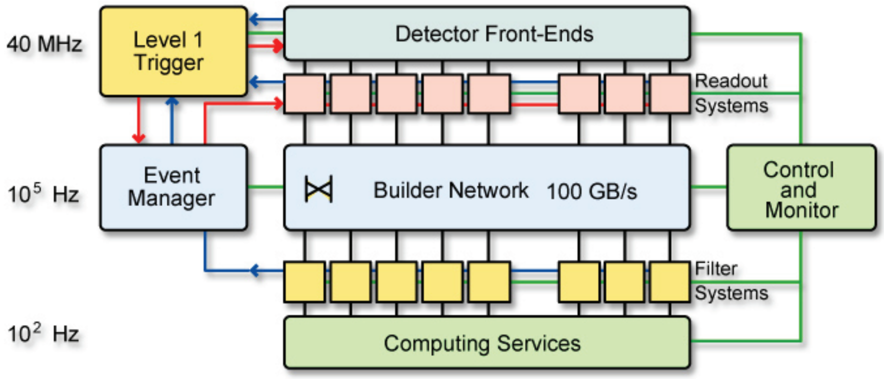

Figure 3.19: Architecture of CMS trigger and data acquisition system [70].

It is a common misconception that a trigger identifies "interesting" events in the background and select them for further processing. This would by definition imply that one already knew what to look for; in fact the purpose of a trigger is to discard data that are understood with our current physical understanding and retain data relating to events that cannot be immediately identified. Of course at the same time one must ensure that the trigger has the capability to distinguish signatures of possible new physics and store them for further study, such as the anticipated Higgs boson. Essentially in CMS this reduces to a selection on the transverse energy,missing transverse energy and types of particle detected. In doing this one is placing as few constraints as possible on the physics available to the end-user (ignoring low energy physics for which the LHC was clearly not designed). This is often described as inclusive triggering and is particularly important for the first trigger stage. In addition to the requirement of efficient event selection, the trigger must also operate with minimal deadtime (a period after a trigger during which data cannot be taken), allowing one to maintain a high efficiency for the recording of useful events. This is achieved using buffers in the detector readout combined with a fast, efficient trigger processor.

3.3.6.1 The Level-1 Trigger

From Fig. 3.20 it can be seen that processing at L1 only uses data from the calorimeters (ECAL and HCAL) and tracks from the muon systems [70]. In the case of the muon trigger this simply involves creating a list of all the tracks detected in a bunch crossing, sorted by their transverse momentum. The top four candidates are then forwarded to the Global Trigger (GT) [72]. The calorimeter trigger objects are more complicated, and fundamentally comprise two types of trigger object, reflecting the two fundamental types of energy deposition in the calorimeter. The first of these are electron/photon candidates mostly detected by the ECAL, which are relatively spatially compact objects. The second type are jets from QCD events that shower in the detector, which produce a broader energy deposition pattern, mostly in the HCAL. The highest-ranked candidates of these types of deposition are again forwarded to the GT.

The GT combines candidates from these two systems and uses them to make a decision on whether to read out a particular event from the detector. The trigger depends on the object being sought, but generally involves simple criteria such as a single muon with a transverse momentum greater than a certain threshold. Composite objects such as two jets combined with two forward jets can also be used for triggering, although the types of trigger object should be kept as simple as possible in order to avoid creating bias in the recorded data.

Tracker and pixel information is not currently used at this stage, simply because data from these detectors is not believed to be necessary for triggering under typical LHC conditions. Even if this belief were to change in the future, the current tracker could not support a full trigger system, due to the incredibly large data volume produced (far greater than that of all of the other detectors in CMS combined) and

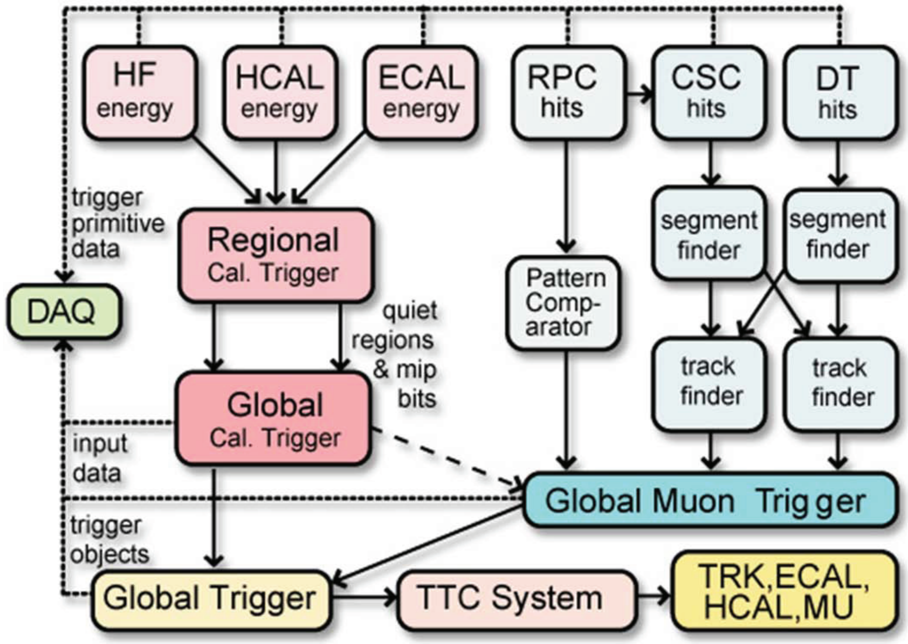

Figure 3.20: Structure of the Level-1 trigger system [70].

the choice of analogue optical link technology and off-detector zerosuppression.

3.3.6.2 Data Acquisition

The CMS data acquisition system processes events accepted by the first-level trigger at a maximum input rate of a few 100 kHz. Event data are read out from the detector and stored in readout buffers at a total rate of 1 Terabit/s. The event-builder then assembles event fragments into full events employing a large switching network. The high-level trigger algorithms run on a farm of O(103) commercial processors. Each event is processed by a single processor, which has access to the full raw event data. High level-trigger reconstruction code will be as close as possible to the full offline analysis code, the main differences resulting from limited processing time and the possible lack of precise calibration constants. The following three key features of HLT software guarantee minimal processing time:

- Reconstruction on demand: trigger objects are only reconstructed if needed in the trigger decision. Unnecessary calculations are avoided by rejecting events as early as possible using fast algorithms. The reconstruction and selection therefore takes place in several stages (virtual trigger levels), which roughly correspond to the functions of traditional second and third trigger levels. There is no limitation to the number of virtual trigger levels or to the algorithms employed except for CPU time. For historic reasons the terminology "Level- 2" is used for a first high-level trigger stage based on data from the muon systems and calorimeters while "Level-3" refers to algorithms including tracker data.

- Partial/Region reconstruction: only parts of detector information are analyzed guided by the trigger objects found in the preceding trigger levels.
- Conditional reconstruction: reconstruction is aborted if further calculations would not alter the result (for example when reconstructing additional tracks in an isolation algorithm) or if the condition arises that resulting trigger object would not be relevant to the trigger decision.

3.4 The CMS Computing and Software

In this analysis the CMS software framework CMSSW is used. Most of the data samples we analyzed were published at the LHC Computing Grid (LCG) system. A remote tool (CRAB) is used to submit the jobs to access the data samples on the grid.

3.4.1 LHC Computing Grid

The LHC experiment, as the largest accelerator on the earth, require enormous amounts of storage capacity and computing power during the operation of the LHC. In addition to the collected raw collision data, there are several millions of simulated Monte Carlo events and various reprocessed or skimmed data samples. The total amount of data adds up to more than 15 Petabytes per year which has to be stored and made accessible for further analyses. These requirements can not be afforded by single institutions or even single countries.

The mission of the LHC Computing Grid project (LCG) [13], in cooperation with the EGEE project (Enabling Grids for E-sciencE) [45], is to build and maintain a data storage and analysis infrastructure for the entire high energy physics community all over the world. It provides access for scientists to geographically distributed computing Grid services, large parts of their computing infrastructures are shared.

LCG is based on four layers or tiers of participating Grid sites distributed around the globe. Fig. 3.21 schematically presents the tier structure of the LCG. The data from the LHC experiments will be distributed according to the tier levels. A primary backup will be recorded on tape at CERN, the "Tier-0" center of LCG. After initial processing, this data will be distributed to a series of Tier-1 centers, large computer centers with sufficient storage capacity for a large fraction of the data, and with round-the-clock support for the Grid. The Tier-1 centers will make data available to Tier-2 centers, each consisting of one or several collaborating computing facilities, which can store su±cient data and provide adequate computing power for specific analysis tasks. Individual scientists will access these facilities through Tier-3 computing resources, which can consist of local clusters in a University Department like one in Peking University.

Like the World Wide Web, invented at CERN in the early 90s for research purposes, scientific Grid projects led by CERN are expected to create new opportunities for commerce and industry. The LHC Computing Grid project, already runs a Grid service for particle physicists spanning over 200 sites at universities and research institutes worldwide.

3.4.2 The CMS Computing Model

The new generation of collider experiments presents challenges not only in terms of the physics to discover and the detector to build and operate, but also in

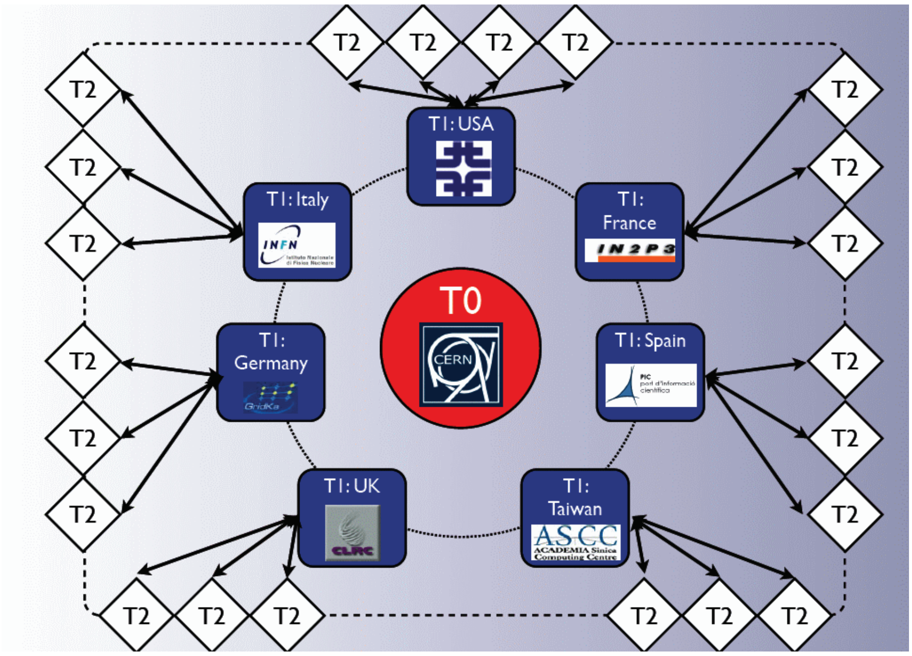

Figure 3.21: Schematic overview of the LCG/CMS tier structure.

terms of the data volume and the necessary computing resources. Data sets and resource requirements are at least an order of magnitude larger than in previous experiments. For both technical and funding reasons, it was decided to connect computing services and resources available in the CMS groups all around the world via the GRID computing network and to construct the CMS computing environment as a fully distributed system. All the computing, storage and connectivity resources will be merged in one infrastructure managing the data processing, data archiving and Monte Carlo event generation. The system will be available to all CMS collaborators, independently of their physical locations.

Overview of the CMS computing model is shown in Fig. 3.22. The CMS computing model [74] defines a hierarchy of the computing centres available to CMS. Three levels or "Tier's" are defined and interconnected:

- the Tier-0 Centre at CERN

  The CMS Grid centre, called Tier-0, is located at CERN. All raw collision

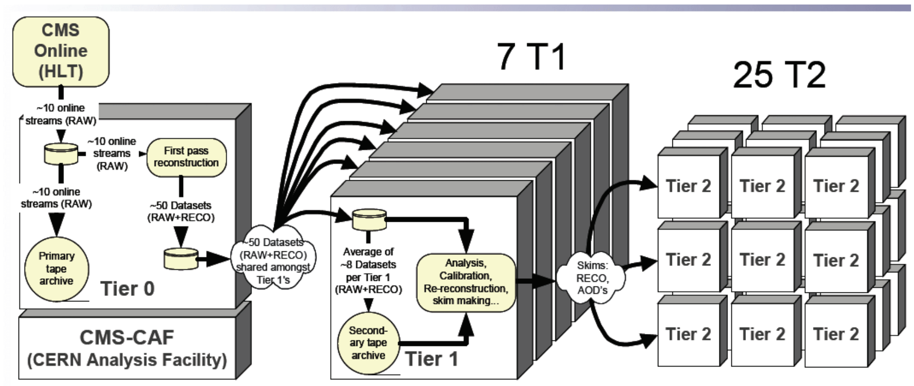

Figure 3.22: Overview of the CMS computing model.

data selected by of the CMS trigger system will be collected on tape and performed a first reconstruction of desired physics objects. The raw and first reconstruction data will be distributed to the Tier-1 centres.

- the Tier-1 Centres

  Currently eight centres are each responsible for the safe keeping of a share of the (second copy of the) RAW and reconstructed data. These centres should have enough CPU power for large-scale reprocessing steps. Their data-product are then distribution to Tier-2 centres, while shares of the simulated data produced in the Tier-2's are stored in the Tier-1 centres too.

- the Tier-2 Centres

  Tier-2 centres are hosted at several CMS institutes all around the world. A typical Tier-2 divides its resources between local institute members and the CMS community as a whole. In general, they provide storage capacities for some smaller skims or AOD (Analysis Object Data) datasets used by physicists for their final analyses on a flexible and easy to access computing farm. Like in case of the Tier-1s, a Tier-2 has to support offline calibration and alignment tasks. Another duty is the production of Monte Carlo datasets and the subsequent transfer to their associated Tier-1 for long term storage.

Hence, the input files for a physics analysis are to be found distributed over the Tier-2 sites. In order to run on the data, jobs should be created, consisting mainly of a configuration file, and send to the sites where the data is located. On a fair share basis, the job is offered a computer node at the given Tier-2 where the job is executed. The resulting output files are then sent back to a storage element selected by the user and can be used for the production of the final physics results. This procedure was followed to access the simulated top quark event data used as an input to the analyses presented in this work.

3.4.3 Simulation and reconstruction software of CMS

In this analysis the CMS software framework CMSSW [75] is used. It's a modular collection of software which is built around the Event Data Model (EDM) and includes the dedicated services which are needed by simulation, reconstruction, detector calibration and alignment. A schematic overview of the software framework is given in Fig. 3.23.

Data is stored in the Event Data Model (EDM), which is capable to hold different types of data from Monte Carlo simulations, raw detector readout, or reconstructed high level objects needed for the physics analysis. The CMSSW framework is modularized in that way that only those parts of the software are loaded which are necessary for the individual job. As mentioned in chapter 2, on the first-level-trigger computer farm a lighter and faster version of the CMS software is run for preselecting the events coming from the detector.

The CMS event data model is centered around the concept of an Event as a C++ object container for all RAW and reconstructed data pertaining to a physics event. During processing, data are passed from one module to the next via the Event, and are accessed only through the Event. The output data is capable to hold different types of data from Monte Carlo simulations, raw detector readout, or reconstructed high level objects needed for the physics analysis. All objects in the Event may be individually or collectively storable as ROOT [76] files, and are thus directly browsable in ROOT.

The CMSSW framework implements a software bus model wherein there is one executable, called *cmsRun*, and many plug-in modules which run algorithms. This allows to use same executable for both detector and Monte Carlo data. This framework is distinct from a more traditional approach in which several executables are used, one per task or set of tasks. The CMSSW executable, cmsRun, is configured at run time by the user's job-specific configuration file (set of parameters). This file tells cmsRun which data to use, which modules to run, which parameter settings to use for each module, and in what order to run the modules. Required modules are dynamically loaded at the beginning of the job.

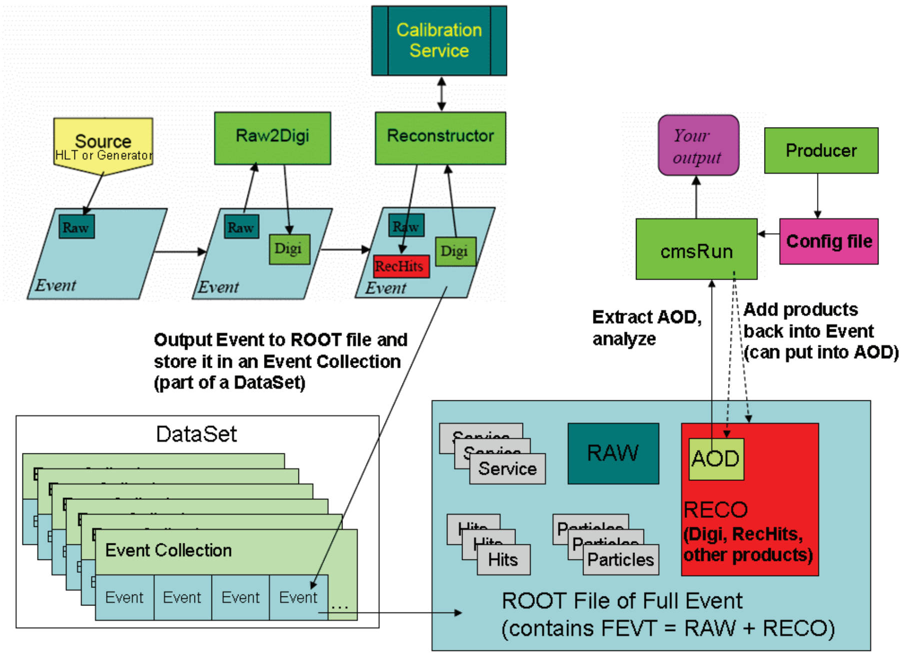

Figure 3.23: A schematic overview of the software framework.

Chapter 4

Event generation and Monte-Carlo samples

Below information will be given on the generation of the Monte Carlo samples used.

4.1 Prompt J/ψ generation in PYTHIA

4.1.1 Processes

We have produced J/ψ events using PYTHIA 6.409 [77]. The implementation [78] is based on the NQRCD approach and quarkonium production via the leading-order singlet and octet mechanism. A summary of sub-processes for all the available color-singlet and color-octet production in PYTHIA is given in Tab. 4.1. With MSEL(61)=1 all are switched on. Detailed information about prompt quarkonium generation can additionally be found in Ref. [50].

The octet $c\bar{c}$-states have a mass of 3.1 GeV/c^2. The values of the NRQCD matrix elements are taken from Ref. [83]. We have modified the default branching ratios for the radiative decays of the χ-states into J/ψ's to correspond to the recent PDG values [2]. The polarization in event generation has been set to zero, and will be modified by event-weighting later. Production via χ states is included. In this

Colour-singlet/octet production in PYTHIA			
Charmonium subprocesses		Bottomonium subprocesses	
421	$g+g \to c\bar{c}[^3S_1^{(1)}]+g$	461	$g+g \to b\bar{b}[^3S_1^{(1)}]+g$
422	$g+g \to c\bar{c}[^3S_1^{(8)}]+g$	462	$g+g \to b\bar{b}[^3S_1^{(8)}]+g$
423	$g+g \to c\bar{c}[^1S_0^{(8)}]+g$	463	$g+g \to b\bar{b}[^1S_0^{(8)}]+g$
424	$g+g \to c\bar{c}[^3P_J^{(8)}]+g$	464	$g+g \to b\bar{b}[^3P_J^{(8)}]+g$
425	$g+q \to q+c\bar{c}[^3S_1^{(8)}]$	465	$g+q \to q+b\bar{b}[^3S_1^{(8)}]$
426	$g+q \to q+c\bar{c}[^1S_0^{(8)}]$	466	$g+q \to q+b\bar{b}[^1S_0^{(8)}]$
427	$g+q \to q+c\bar{c}[^3P_J^{(8)}]$	467	$g+q \to q+b\bar{b}[^3P_J^{(8)}]$
428	$q+\bar{q} \to g+c\bar{c}[^3S_1^{(8)}]$	468	$q+\bar{q} \to g+b\bar{b}[^3S_1^{(8)}]$
429	$q+\bar{q} \to g+c\bar{c}[^1S_0^{(8)}]$	469	$q+\bar{q} \to g+b\bar{b}[^1S_0^{(8)}]$
430	$q+\bar{q} \to g+c\bar{c}[^3P_J^{(8)}]$	470	$q+\bar{q} \to g+b\bar{b}[^3P_J^{(8)}]$
431	$g+g \to c\bar{c}[^3P_0^{(1)}]+g$	471	$g+g \to b\bar{b}[^3P_0^{(1)}]+g$
432	$g+g \to c\bar{c}[^3P_1^{(1)}]+g$	472	$g+g \to b\bar{b}[^3P_1^{(1)}]+g$
433	$g+g \to c\bar{c}[^3P_2^{(1)}]+g$	473	$g+g \to b\bar{b}[^3P_2^{(1)}]+g$
434	$g+q \to q+c\bar{c}[^3P_0^{(1)}]$	474	$g+q \to q+b\bar{b}[^3P_0^{(1)}]$
435	$g+q \to q+c\bar{c}[^3P_1^{(1)}]$	475	$g+q \to q+b\bar{b}[^3P_1^{(1)}]$
436	$g+q \to q+c\bar{c}[^3P_2^{(1)}]$	476	$g+q \to q+b\bar{b}[^3P_2^{(1)}]$
437	$q+\bar{q} \to c\bar{c}[^3P_0^{(1)}]+g$	477	$q+\bar{q} \to b\bar{b}[^3P_0^{(1)}]+g$
438	$q+\bar{q} \to c\bar{c}[^3P_1^{(1)}]+g$	478	$q+\bar{q} \to b\bar{b}[^3P_1^{(1)}]+g$
439	$q+\bar{q} \to c\bar{c}[^3P_2^{(1)}]+g$	479	$q+\bar{q} \to b\bar{b}[^3P_2^{(1)}]+g$

Table 4.1: Color-singlet/octet production sub-processes and their corresponding ISUB indices in PYTHIA [77] (in the left side of each column).

study we forced the J/ψ to always decay into $\mu^+\mu^-$, the branching ratio of which is 5.93%. The following features are included.

4.1.2 Cross section regularization

An event re-weighting function is used to allow the quarkonia cross section to be dampened at small $p_T^{J/\psi}$ values, in analogy to the underlying event (UE) formalism in PYTHIA [79, 80] where the $gg \to gg$ cross section is dampened at small transverse momentum. Since prompt quarkonium production takes dominantly place via $gg \to gg$, this dampening naturally applies here too. Cross section dampening is switched on with MSTP(142)=2. The damping is realized by giving each event a weight w_i according to

$$w_i = \frac{\sigma_{reweighted}}{\sigma_{not\ reweighted}} = \Big(\frac{\hat{p}_T^2}{p_{T_0}^2 + \hat{p}_T^2}\Big)^2 \Big(\frac{\alpha_S(p_{T_0}^2 + Q^2)}{\alpha_S(Q^2)}\Big)^3 \tag{4.1}$$

where $\hat{p}_T$ is the transverse momentum evaluated in the rest frame of the scattering, Q^2 the momentum transfer scale, and p_{T_0} the regularisation scale, used also in the underlying event cross section regularisation. The latter is a free parameter of the model, empirically of order 2 GeV/c at the Tevatron Run 2 ($\sqrt{s} = 1.96$ TeV) [81]. It is not apriori clear what p_{T_0} would be at LHC energies, but is generally believed to grow with s [77]. The default energy dependence in PYTHIA is $p_{T_0} \propto E_{cm}^{PARP(90)} = E_{cm}^{0.16}$, the value of 0.16 being inspired by the rise of the total cross section with the Pomeron term, $s^{0.08} = E_{cm}^{2*0.08} = E_{cm}^{0.16}$.

To retain the analogy with the underlying event formalism, where PARP(82) is the regularization scale of the transverse-momentum spectrum for multiple interactions, and extrapolating the p_{T_0} value determined at 1.96 TeV to the LHC energy, the parameter p_{T_0} for quarkonium reweighting is

$$p_{T_0} = PARP(82)\Big(\frac{E_{cm}}{PARP(89)}\Big)^{PARP(90)} = 1.94\text{GeV}\Big(\frac{14\text{TeV}}{1.96\text{TeV}}\Big)^{0.16} \approx 2.66\text{GeV} \tag{4.2}$$

The value of PARP(82) was determined for CMS to be 1.94 GeV, see Ref. [82]. As can be seen from Eq. (4.1), at small $\hat{p}_T$, and thus small $p_T^{J/\psi}$, a suppression is obtained, while at large $\hat{p}_T$, and thus large $p_T^{J/\psi}$, the cross section is unmodified.

4.1.3 Shower activity associated with quarkonium production

The main advantage of the use of PYTHIA is the fact that parton cascades for the color-octet states are included. Indeed, showers are expected for a colour octet state arising from two contributions: 1) repeated $g \to gg$ branchings before the branching $g \to c\bar{c}$, and 2) from the radiation off the color octet $c\bar{c}$-state once formed. PYTHIA contains dedicated switches (MSTP(148) and MSTP(149)) to regulate the shower activity off the color-octet states by modifying the Altarelli-Parisi evolution of the color-octet states.

4.1.4 Tuning of PYTHIA parameters with CDF data

The main switch for generating quarkonia is MSEL(61)=1 (see Sec. 4.1.1). However, there are several PYTHIA parameters which should be tuned carefully for quarkonium generation at CMS.

- The NRQCD matrix elements. The tuning [26, 83], listed in Table 4.2, is determined from the CDF data for $p_T^{J/\psi}$ >8GeV/c by the Parton Distribution Function (PDF) CTEQ5L. It is important to note that all ^3P_J octet states are simulated using a single NRQCD matrix element $\langle o[^3P_J^{(8)}]\rangle$ with the relation of $\langle o[^3P_J^{(8)}]\rangle = (2J+1)\langle o[^3P_0^{(8)}]\rangle$.

- The cross section dampening at low transverse momenta (see Sec. 4.1.2). As recommended, we make use of cross section reweighting and thus set MSTP(142)=1.

- The shower-activity switches MSTP(148) and MSTP(149) (see Sec. 4.1.3). It is recommended to switch on MSTP(148), allowing for showering. We have chosen to switch on MSTP(149) as well, to allow for a relatively large amount of showering.

- The polarization switches MSTP(145-147). With MSTP(145)=0 non-polarized quarkonium is produced. If MSTP(145) is chosen to be 1,

PYTHIA parameter	Value	Matrix element
PARP(141)	1.16	$\langle O(J/\psi)[^3S_1^{(1)}]\rangle$
PARP(142)	0.0119	$\langle O(J/\psi)[^3S_1^{(8)}]\rangle$
PARP(143)	0.01	$\langle O(J/\psi)[^1S_0^{(8)}]\rangle$
PARP(144)	0.01	$\langle O(J/\psi)[^3P_0^{(8)}]\rangle/m_c^2$
PARP(145)	0.05	$\langle O(\chi_{c0})[^3P_0^{(1)}]\rangle/m_c^2$
PARP(146)	9.28	$\langle O(\Upsilon)[^3S_1^{(1)}]\rangle$
PARP(147)	0.15	$\langle O(\Upsilon)[^3S_1^{(8)}]\rangle$
PARP(148)	0.02	$\langle O(\Upsilon)[^1S_0^{(8)}]\rangle$
PARP(149)	0.02	$\langle O(\Upsilon)[^3P_0^{(8)}]\rangle/m_b^2$
PARP(150)	0.085	$\langle O(\chi_{b0})[^3P_0^{(1)}]\rangle/m_b^2$

Table 4.2: J/ψ and Υ NRQCD matrix elements and corresponding parameters in PYTHIA. See Refs. [26, 83].

MSTP(147)=0 (helicity=0) is used to generated longitudinally polarized quarkonium and MSTP(147)=1 (helicity=$\pm$1) is used to generated transversely polarized quarkonium. Here MSTP(145-147) have been set to zero, i.e. no polarization. The polarization can be adapted at a later stage by event-reweighting.

- General switches, not specifically related to quarkonia, such as PDFs, α_s, etc. Since the NRQCD elements we used are determined from CDF data with the parton distribution function of CTEQ5L, we have used this same PDF. We made use of the default Underlying Event settings that are used for most of the Monte Carlo productions in CMS [84].

With these parameters, we first made some productions with $p\bar{p}$ collision at Tevatron energy: 1.80TeV and 1.96TeV. The resulting cross sections fitted reasonably well with the CDF experiment data, as shown in Fig. 4.1.

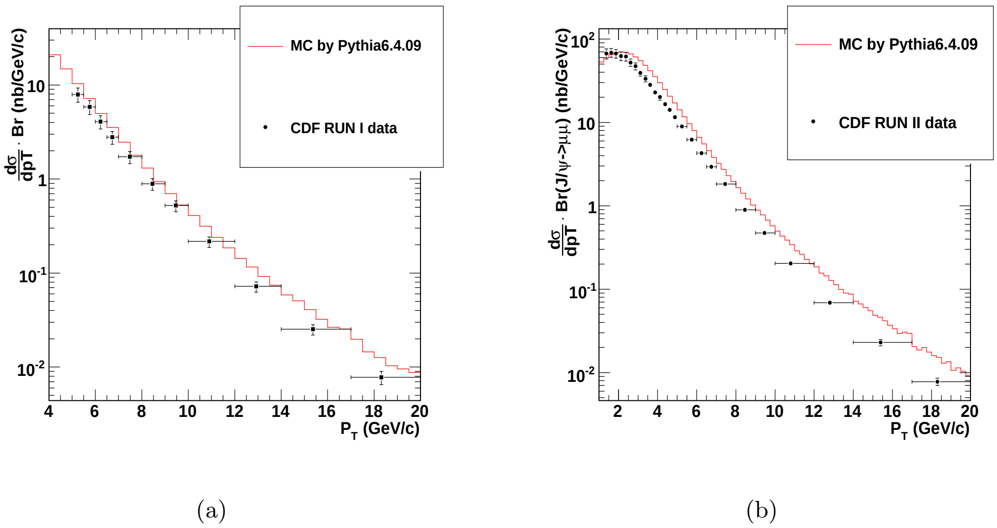

Figure 4.1: Prompt J/ψ differential cross sections in $p\bar{p}$ collision at Tevatron energy: 1.80TeV (left) and 1.96TeV (right) respectively.

The production of $\Upsilon(1S)$, as well as $\Psi(2S)$, $\Upsilon(2S)$ and $\Upsilon(3S)$ can be established by changing the processes and the values of NRQCD matrix elements.

4.2 Overview of the used Monte Carlo samples

4.2.1 Prompt J/ψ event samples

For the current study we have used samples of Monte Carlo generated signal and background events. A list of all the official and private MC event samples used in this analysis is displayed in Tab. 4.3. In CSA07 production, based on the tuned parameters described above, two million prompt $J/\psi \rightarrow \mu^+\mu^-$ signal events were generated and simulated in CMSSW_1_4_2, and then reconstructed in CMSSW_1_6_7. At generator level, only events who have two muons with the following kinematic criteria were retained for the detector simulation:

$$p_T(\mu) > 2.0\ GeV/c, \\ |\eta(\mu)| < 2.5, \tag{4.3}$$

where $p_T(\mu)$ is the transverse momentum of muon and $\eta(\mu)$ is its pseudorapidity. The effective cross section for prompt J/ψ of this sample can be estimated by:

$$\sigma(\text{prompt}) = \sigma(pp \to J/\psi + X) \cdot BR(J/\psi \to \mu^+\mu^-) \cdot \epsilon_{kine} \tag{4.4}$$

where $\epsilon_{kine} = \%$ is the probability of a event to pass the kinematic cuts 4.5. Taking into account the experimentally measured value

$$BR(J/\psi \to \mu^+\mu^-) = (5.93 \pm 0.06)\%, \tag{4.5}$$

the total effective cross section is estimated as:

$$\sigma(\text{prompt}) = 3000\mu b \tag{4.6}$$

The differential cross section at CMS for prompt J/ψ is shown in Fig. 4.2, and compared to that for J/ψ from B-hadron decays.

4.2.2 Non-prompt J/ψ event samples

The non-prompt J/ψ sample used for the current analysis consists of one million inclusive $b \to J/\psi \to \mu^+\mu^-$ events.It contains an admixture of b-flavored hadrons $(B^\pm, B^0, B_s^0 andb - baryon)$, decaying into final states with a J/ψ resonance. The sample is in the CSA07 production by using the generic QCD 2→2 event generation in Pythia (MSEL=1). The first generator filter requires two b quarks which will hadronize into two bottom hadrons. One of the two bottom hadrons is forced to decay with a probability into $J/\psi X$ which always decay into two muons, and the other is forced to decay in leptonic or semi-leptonic modes. The second filter is the same as used in the prompt J/ψ sample , Equation 4.5. The effective cross section for non-prompt J/ψ can be estimated in the following way:

$$\sigma(\text{B-decay}) = 2 \cdot \sigma(pp \to b\bar{b} + X) \cdot BR(b \to J/\psi) \cdot BR(J/\psi \to \mu^+\mu^-) \cdot \epsilon'_{kine} \tag{4.7}$$

where ϵ'_{kine} is the probability to pass the kinematic cuts. The production cross section of the $b\bar{b}$ pairs at LHC is estimated to be 500 nb (see Sec. 2.3.4). Assuming the following branching fractions for the individual decays

$$BR(b \to J/\psi) = (1.16 \pm 0.10)\%, \tag{4.8}$$

$$BR(J/\psi \to \mu^+\mu^-) = (5.93 \pm 0.06)\%, \tag{4.9}$$

the effective cross section can be estimated as:

$$\sigma(\text{B-decay}) = 51.4nb \tag{4.10}$$

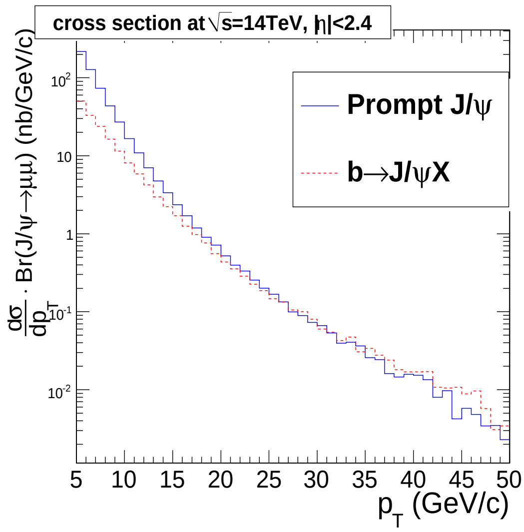

Figure 4.2: Prompt and non-prompt J/ψ differential cross sections in pp collision at 14 TeV in the range $|\eta_{J/\psi}| < 2.4$.

4.2.3 Background samples

As background events we have considered any other source of muons that, when paired, could accidentally have an invariant mass close to the J/ψ mass. The following sources of background events were considered:

- generic QCD 2→2 events produced with Pythia (MSEL=1), requiring the presence of one μ with $p_T^\mu > 2.5$ GeV/c and $|\eta_\mu| < 2.5$, mainly coming from heavy flavoured quark decays. These events are referred to as "muon enriched

QCD background" in the following. Although this sample does take into account background combinatons of one prompt muon and one fake muon (see Sec. ??), background from combinations of two fake muons are not included. The effect of omitting this background is small and will be discussed in the systematic uncertainties.

- Drell-Yan events, where both muons have $p_T^\mu > 2.0$ GeV/c and $|\eta_\mu| < 2.5$.

Overall, about 2 million prompt J/ψ events, 1 million B-hadron decays events, 2 million Drell-Yan and 20 million muon enriched minimum bias events were produced, processed through a full GEANT based detector simulation, and passed through the standard CMS reconstruction program.

Sample	Production	N_0	σ (mb)	$\int \mathcal{L}$ (pb^{-1})	pre-selection
Charmonium_Pt_0_20	CSA07	1021134	0.3544	3.03	2μ $p_T^\mu >$ 2.0GeV/c, $\lvert\eta_\mu\rvert$ <2.5
Charmonium_Pt_20_inf	CSA07	1012650	1.014e-4	416	2μ $p_T^\mu >$ 2.0GeV/c, $\lvert\eta_\mu\rvert$ <2.5
$B \to J/\psi \to \mu\mu$	CSA07	556324	54.71	12.2	2μ $p_T^\mu >$ 2.0GeV/c, $\lvert\eta_\mu\rvert$ <2.5
$\bar{B} \to J/\psi \to \mu\mu$	CSA07	509527	54.71	11.2	2μ $p_T^\mu >$ 2.0GeV/c, $\lvert\eta_\mu\rvert$ <2.5
Muon_ppMuX	CSA07	20697806	54.71	0.45	1μ $p_T^\mu >$2.5 GeV/c, $\lvert\eta_\mu\rvert$ <2.5
J/ψ soup	CSA07-Stew	410718			HLT J/ψ trigger
Drell-Yan	Private	131179	1.051e-4	19	2μ $p_T^\mu >$2.0 GeV/c, $\lvert\eta_\mu\rvert$ <2.5

Table 4.3: Events samples, number of filtered events N_0, σ the total cross section before pre-selection, integrated luminosity, and generator filter cut. CSA07 samples in CMSSW_1_6_X.

4.2.4 Data streams and analysis strategy

The analysis chain consists of two different steps. First, the data are skimmed using a loose pre-selection that requires the presence of a J/ψ as selected by the HLT trigger (see next Section). At this stage we will select also a subset of events skimmed requiring a single muon HLT trigger with the lowest p_T^μ (depending on which trigger menu will be available at the precise instantaneous luminosity of

LHC) and that will be used for measuring most of the efficiencies using a tag and probe method.

In the second step, the analysis is performed using the final selection offline criteria.

Chapter 5

The CMS muon and J/ψ trigger

This chapter presents the CMS muon and J/ψ trigger system and performance. To study the latest trigger menus, the event samples in summer 2008 production were used, which is produced in CMSSW_2_1_8.

5.1 The CMS Muon Trigger system

As mentioned in Sec. 3.3.6, the CMS experiment uses a two-level trigger algorithm: a hardware-based Level-1 (L1) trigger and a software-based single stage High Level Trigger (HLT), running on a dedicated farm of commercial processors. The HLT reduces the output rate of the L1 trigger (100 kHz) to a value of approximately 100 Hz, limited by present storage capabilities. The bandwidth of 100 Hz should be shared between all physical channels of interest.

The L1 Trigger has to take the decision whether to accept or to reject an event for each bunch crossing with negligible deadtime. The crossing interval of 25 ns is too short to process the complete trigger information, therefore a pipelined system that stores the data during a latency time of 3.2 μs has been conceived. The rate reduction capability is designed to be at least a factor of 106 for the combined L1 and HLT, as the highest rate that can be archived by the on-line computer farm is of the order of 100 Hz. The maximum bandwidth allocated to the L1 Trigger is

100 kHz, in accordance with the input capacity limit of the HLT processor farm. However, at the startup of LHC, it will be reduced to 50 kHz for operational reasons.

5.1.1 The Level-1 Muon Trigger

The overall structure of the CMS Level-1 trigger is shown in Fig. 3.20. It consisted of three main systems: the Calorimeter Trigger, the Muon Trigger and the Global trigger. The Level-1 triggers are based on selecting trigger objects, which are candidate electrons or photons, muons, jets, τ -jets as well as total and missing transverse energies and jet multiplicities. Neither the silicon inner tracker nor the pixel vertex detector takes part in the Level-1 Trigger.

The task of the Muon trigger [70] is to identify muons, reconstruct their position and transverse momentum and provide bunch crossing assignment with high purity and efficiency. All three CMS muon subsystems take part in the trigger and can deliver information on transverse momentum and location of muon candidates. The tracking chambers in the barrel and in the forward regions are equipped with electronics suitable for triggering. Precise timing information is delivered both by the drift tube (DT) and cathode strip chambers (CSC). The resistive plate chambers (RPC) mounted on the tracking chambers are dedicated trigger chambers.

In the DT and CSC Trigger, local trigger electronic identify track segments at the muon stations based on the signals of multiple layers of chambers. Segments are then matched by the DT and CSC regional track finder, which reconstruct muon tracks and estimate their p_T. Besides precise position information. the track segments also include information on the track direction and quality. The CSC system covers the end-cap region up to $|\eta| < 2.4$. However, the trigger electronics will not be installed in the region above $|\eta| = 2.1$, effectively limiting the muon trigger geometrical acceptance to $|\eta| < 2.1$. The RPCs provide limited spatial resolution, but excellent time resolution, of a order of few nanoseconds. Six layers of RPCs are present in the barrel and four in each end-cap. No local reconstruction step is present in the RPC trigger, since the measurements in each RPC chamber are simple points.

Since three different muon subsystems take part in the trigger, CMS needs an entity to determine unique muon candidates. This entity is the Global Muon Trigger. It sorts the DT, CSC and RPC candidates and tries to match them. It achieves an increased efficiency with respect to the three separate muon systems, whilst reducing trigger rates and the occurrence of fake muons. The Global Muon Trigger also correlates muon candidates with regions in the calorimeter in order to confirm minimal ionization and to apply isolation criteria.

At a luminosity of $10^31cm^{-2}s^{-1}$, the Level-1 single-muon rate is about 1 kHz for thresholds as low as 5 GeV while the di-muon rate is smaller than 20 Hz at the lowest useful threshold of 3 GeV. More detailed information on Level-1 rates as a function of p_T can be found in the Appendix of Ref. [**?**].

The distribution of transverse momentum and pseudorapidity of signal muon tracks, reconstructed by the level-1 trigger are presented in Fig. 5.1. The muon efficiencies as a function of p_T and η are present in Fig. 5.2. The efficiency of Level-1 muon is above 97% when it's transverse momentum larger than 5 GeV/c. If a muon in barrel region has a transverse momentum smaller than 5 GeV/c, it has few hits in DT and hardly to be triggered.

5.1.2 The High-Level Muon Trigger

The High Level Trigger (HLT) [70] is the second step of the online CMS selection chain. Its goal is to reduce the event rate from the maximum Level-1 output rate of 100 kHz to a rate of O(100) Hz. This is the maximum acceptable rate for storage and further processing, given that the average event size after zero suppression is of the order of 1 MB. The HLT is implemented on software running on a single farm of commercial processors, each processing one full event at a time.

It is customary to identify two steps, the Level-2, where the data of the calorimeters and muon detectors are used, and the Level-3, which also utilizes the full information from the inner tracker, for which reconstruction is more time con-

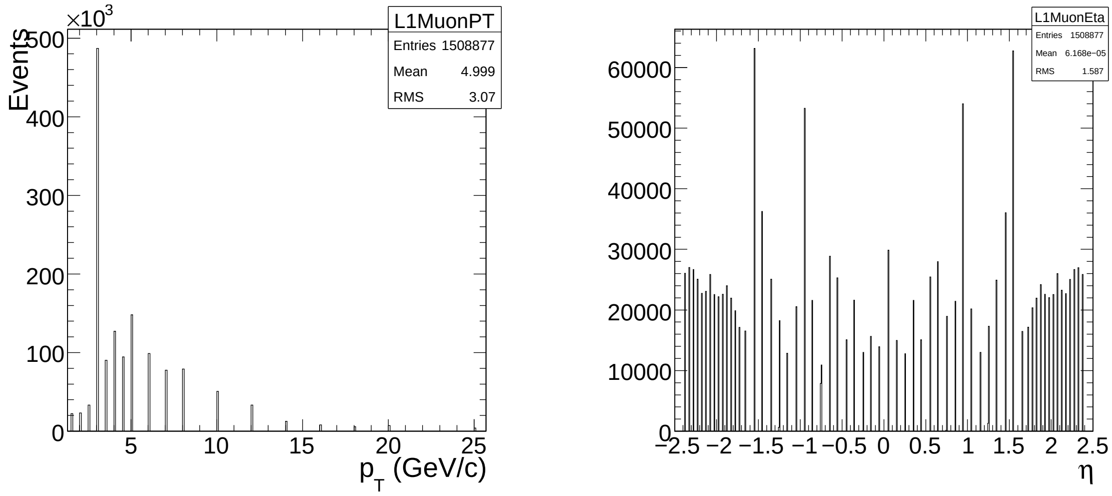

Figure 5.1: Distributions of transverse momentum (a) and pseudorapidity (b) of muon trajectories reconstructed with L1 trigger.

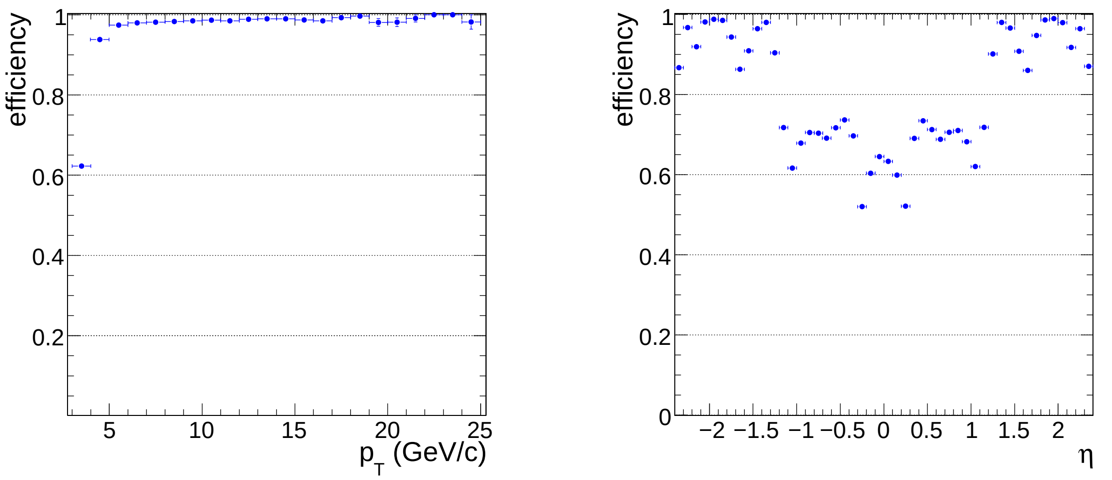

Figure 5.2: (a) L1 muon efficiencies as a function of p_T^{μ} , integrated over the pseudorapidity range $|\eta_\mu| < 2.4$; (b) L1 muon efficiencies as a function of η_μ , integrated over the p_T range $|p_T^{\mu}| > 3GeV/c$.

suming. Additional rate rejection is obtained at both levels by the use of isolation algorithms. The HLT reconstruction algorithms are implemented using the concept of regional reconstruction, that is the ability to reconstruct an object using only the information coming from a limited region of one (or more) sub-detectors. This leads to significant CPU savings and allows discarding uninteresting events even without reading out the full event. Regional reconstruction requires prior definition of a region of interest; therefore each trigger level uses the candidates reconstructed at the previous level as seeds. The steering of the HLT software is based on the concept of reconstruction on-demand, i.e. algorithms are executed only when (and if) the corresponding piece of information is requested.

5.1.2.1 The Level-2 Muon Reconstruction

The Level-2 step improves the Level-1 muon trigger response using the full resolution of the muon detectors. It consists of regional reconstruction based on the iterative Kalman Filter method [86]. The selection is based on a cut on the p_T of reconstructed muons.

Track seeds are initially created using Level-1 muon candidates. Starting from this seed, hits to be included in the fit are looked for iteratively. At each step, the trajectory is extrapolated to the closest layer of detectors, where local reconstruction is performed only in the chambers compatible with the extrapolated state, according to the principle of regional reconstruction. The results of local reconstruction are track segments in the DT or CSC systems, or three-dimensional hits for the RPCs. They are used to update the estimate of the trajectory parameters with the Kalman Filter method. This procedure is repeated until the fit reaches the last station. The result is a track state at the outermost muon station, updated with all available measurements. This is used as seed to the actual fit, which is performed in a similar way going inwards to the detector center.

Ghost tracks are then removed and the trajectory is extrapolated to the point of closest approach to the beam line. The nominal interaction point with its spread is included in the track fit. A cut on the χ^2 of the fit reduces the contribution of non-prompt muons produced by decays of kaons and pions.

The typical p_T resolution obtained by the Level-2 reconstruction, for muons coming from J/ψ decays, is about 10% in the barrel, 16% in the end-cap and 21% in the overlap region. The improvement in the resolution with respect to the Level-1 trigger allows to reduce the muon rate by almost an order of magnitude. The efficiency of Level-2 muon reconstruction is about 95% for a muon with $p_T > 7GeV/c$ and 45% at $3GeV/c < p_T < 4GeV/c$. Fig. 5.3 gives the efficiencies as a function of p_T^{μ} and η_{μ} , comparing with the Level-3 reconstruction.

5.1.2.2 The Level-3 Muon Reconstruction

At Level-3, muon tracks are reconstructed using data from the full tracker system. The resulting improved resolution allows a much sharper p_T cut than at Level-2.

The Level-3 reconstruction starts with the definition of a "region of interest" in the silicon detectors, based on the parameters and uncertainties of the Level-2 track after the vertex constraint. Regional track reconstruction is performed using tracker hits within this region.

Seeds are generated from pairs of reconstructed hits from the pixel detectors or the double-sided silicon strip layers. A beam spot constraint allows an estimate of the trajectory parameters of these seeds, whose number is limited by a cut on their minimum transverse momentum.

The seeds are then used to perform reconstruction within the region of interest using the Kalman Filter method. Starting from the seeds, compatible hits are searched for in the subsequent layers. If more than one is found, a new trajectory is created. These trajectories are grown in parallel, but to avoid a combinatorial explosion their number is limited by selecting them on the basis of the χ^2 of the fit. If no hit is found on a layer, the search is repeated in the following layer. The track is discarded if no hit is found in more than four consecutive layers. After the trajectories for all seeds have been generated, the trajectories with the lowest χ^2 are selected among those that share more than half of their hits. Finally, the trajectories are refitted including also the hits of the Level-2 track reconstructed in the muon chambers.

The typical p_T resolution obtained by the Level-3 reconstruction, for muons coming from J/ψ decays, is about 0.8% in the barrel, 2.0% in the end-cap and 1.5% in the overlap region. Fig. 5.3 shows the efficiencies of Level-3 muon reconstruction as a function of p_T^μ and η_μ , comparing with the Level-2 reconstruction. Muon with $p_T > 7GeV/c$ will have a probability of 80% to be reconstructed as a Level-3 muon.

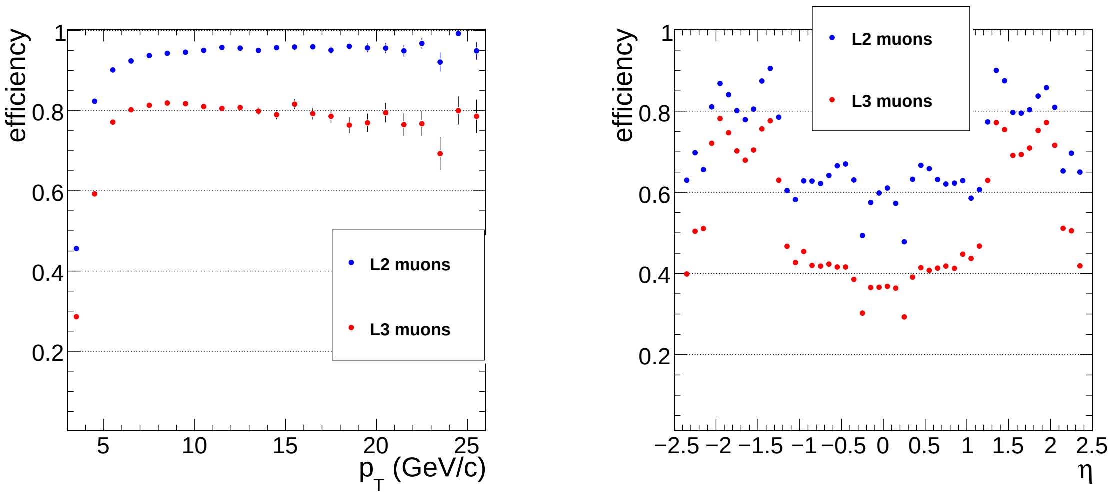

Figure 5.3: (a) L2 and L3 muon efficiencies as a function of p_T^μ , integrated over the pseudorapidity range $|\eta_\mu| < 2.4$; (b) L2 and L3 muon efficiencies as a function of η_μ , integrated over the p_T range $|p_T^\mu| > 3GeV/c$.

5.1.3 The Muon Trigger Paths

5.1.3.1 The single and double muon trigger

The Trigger Study Group (TSG) [87] provided two start-up trigger menus called "8E29" and "1E31", according to the instantaneous luminosities where they are expected to be effective. Tab. 5.1 shows the names of the muon trigger paths, including their Level-1 seeds and HLT p_T and η thresholds. A single muon trigger is based on the Level-3 (combined muon system and tracker) HLT muon reconstruction, with thresholds on p_T and η. The Level-1 single muon trigger is required as input. A double muon trigger, using Level-1 double muon trigger as input, and requiring two Level-3 muons with certain selection criteria.

HLT path	L1 seeds	Description
HLT_Mu3	L1_SingleMu3	one L3 muon $p_T > 3GeV/c, \|\eta\| < 2.1$
HLT_Mu5	L1_SingleMu3	one L3 muon $p_T > 5GeV/c, \|\eta\| < 2.1$
HLT_Mu9	L1_SingleMu7	one L3 muon $p_T > 9GeV/c, \|\eta\| < 2.1$
HLT_DoubleMu3	L1_DoubleMu3	two L3 muons $p_T > 3GeV/c, \|\eta\| < 2.4$
HLT_DoubleMu3_JPsi	L1_DoubleMu3	two L3 muons $p_T > 3GeV/c, \|\eta\| < 2.4$ mass window cut [2.8, 3.4] GeV/c^2
HLT_DoubleMu3_Upsilon	L1_DoubleMu3	two L3 muons $p_T > 3GeV/c, \|\eta\| < 2.4$ mass window cut [8, 12] GeV/c^2

Table 5.1: Some of the HLT muon trigger path: names, L1 seeds, thresholds.

At the LHC start-up, some relaxed single-muon trigger path are used to collect as much muon events as possible. The lowest p_T threshold for a detectable muon in the muon chambers is $p_T > 3GeV/c$, which is unprescaled at the first luminosity. In the second menu, events which have at least one Level-3 muon with $p_T > 5GeV/c$ are reduced at Level-1 trigger by a prescale factor of 25. Events with at least one Level-3 muon $p_T > 9GeV/c$ are unprescaled. The double muon trigger with low rates will not be prescaled in neither two luminosity scenarios. Two special double trigger, J/ψ and Υ trigger which will be described in the following section, are used to collect the events with di-muon resonance for detector calibration and alignment.

5.1.3.2 J/ψ trigger architecture

Since the di-muon channel of J/ψ and Υ can be an important source for detector calibration and alignment at the pilot run, the HLT trigger group would like to increase the rates for $J/\psi \rightarrow \mu\mu$ signals as much as possible for the luminosity of 10^{32} cm^{-2}s^{-1}, which corresponds to the integrated luminosity of the first 1 fb^{-1}

data.

In CMS a dedicated J/ψ trigger will be used, a schematic overview of which is given in Fig. 5.4. The trigger consists of Level 1 (L1), Level 2 (L2) and Level 3(L3) [70]. Although detailed studies are still ongoing, the current understanding is that a double muon trigger will be used, which will be unsprescaled.

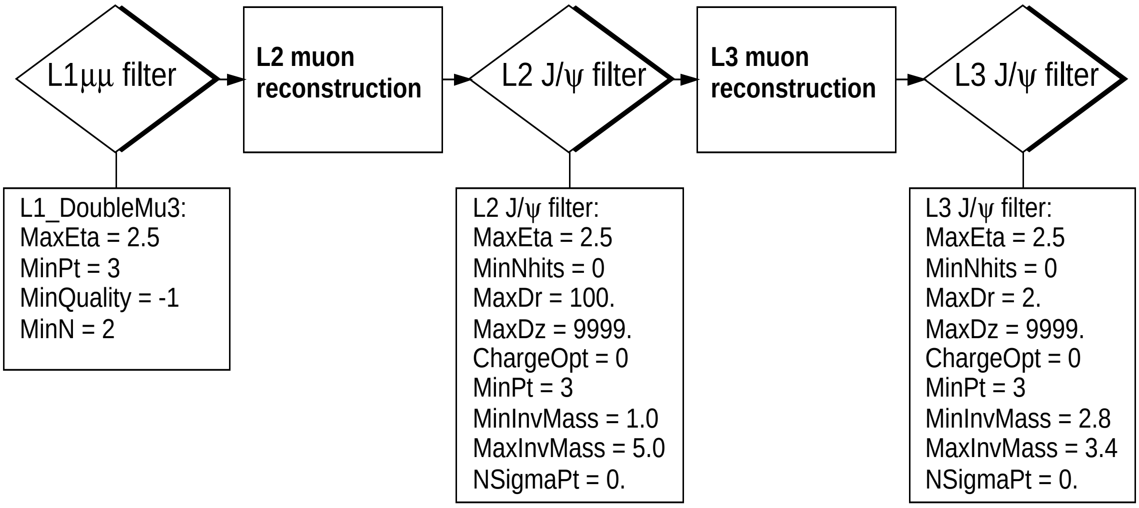

Figure 5.4: Architecture of J/ψ trigger.

At L1, a double muon trigger with a p_T^μ threshold of 3 GeV/c is used. L1 muon candidates are then used to seed the reconstruction of L2 muons in the muon chambers. At this stage the transverse momentum reconstruction of the muons is refined by using the beam spot constraint. After L2 muon candidates are reconstructed they are used to refine the filter for J/ψ. At least two L2 muons with opposite charge and transverse momentum above 3 GeV/c are required. Furthermore, the invariant mass of these two muons should be between 1 and 5 GeV/c^2. This large mass window allows to efficiently select the J/ψ resonance, due to the (still) poor momentum resolution of the L2 muon reconstruction. In fact, as shown in Fig.

5.5(left) , the invariant mass of L2 muon pair from J/ψ meson decays is found to have a width of about 340 MeV/c^2.

Muons from L2 reconstruction are input to the L3 reconstruction step, where the tracker information is used. The track parameters and uncertainties of the L2 muon constrained to the interaction region define a rectangular $\eta\phi$ region in the silicon tracker where tracks are reconstructed from the hits of the tracker and the muon chambers, leading to L3 muons. The L3 J/ψ filter requires at least two L3 muons with opposite charge and transverse momentum above 3 GeV/c, and their invariant mass between 2.8 GeV/c^2 and 3.4 GeV/c^2. The accepted mass window (Fig. 5.5) is larger than the current resolution in the invariant mass, in order to allow for sufficient statistics to populate the non resonant sidebands, that will be used to control the background level and perform the analysis studies.

The Υ trigger is similar with above, with exception of the mass window which is at L2 [6,13] GeV/c^2, and [8,11] GeV/c^2 at Level 3.

It must be noted that at the very beginning of the CMS data taking, because of the extremely low instantaneous luminosity of the LHC, it is possible that lower thresholds will be used. At the very beginning of CMS data taking, because of the extremely low instantaneous luminosity (lower than $10^{30}\text{cm}^{-2}\text{s}^{-1}$), we consider to select J/ψ events using only a single muon trigger. In the current studies the presence of the ψ' resonance has been neglected, but the impact is expected to be small.

5.2 J/ψ trigger efficiencies and rates

As in Tab. **??**, different thresholds will be used for single and double muon triggers at different instantaneous luminosities. The trigger selection is crucial for the start-up analysis on J/ψ measurements. The trigger performance of J/ψ events are studied in CMSSW_2_2_5, using the private data sample of prompt and non-prompt J/ψ without muon kinematics cut at generator level. The inclusive muon

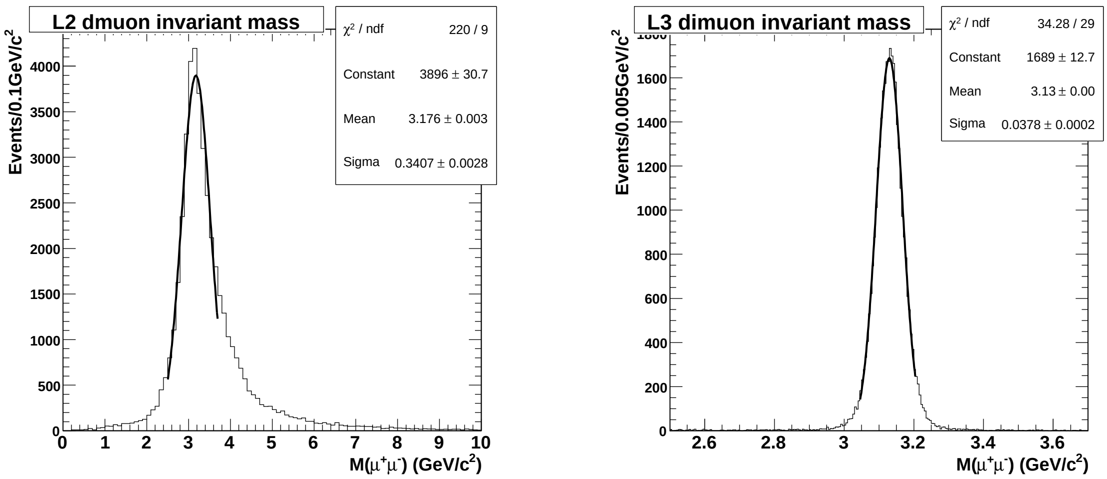

Figure 5.5: J/ψ invariant mass distribution of two Level-2 muons (left) and Level-3 muons (right).

sample in summer 2008 production is used as background.

5.2.1 J/ψ trigger efficiencies

The transverse momentum and pseudorapidity distributions of J/ψ that passes the different L1 muon triggers are shown in Fig.5.6. The Level-1 J/ψ trigger efficiencies times the acceptances as a function of $p_T^{J/\psi}$ and $\eta_{J/\psi}$ are given in Fig.5.7. For J/ψ with $p_T^{J/\psi} > 7GeV/c$, the probability to pass low p_T single muon L1 trigger is above 95%.

The transverse momentum and pseudorapidity distributions of J/ψ that passes the different HLT muon paths are shown in Fig.5.8. The combined Level-1 and HLT J/ψ trigger efficiencies times the acceptances as a function of $p_T^{J/\psi}$ and $\eta_{J/\psi}$ are given in Fig.5.9. For J/ψ with a pseudorapidity above 2.1 should have one muon in $\eta_\mu < 2.1$ to be able to pass the single muon triggers. Due to this acceptances, the efficiency of single muon trigger for J/ψ reaches 90% at high transverse momentum region.

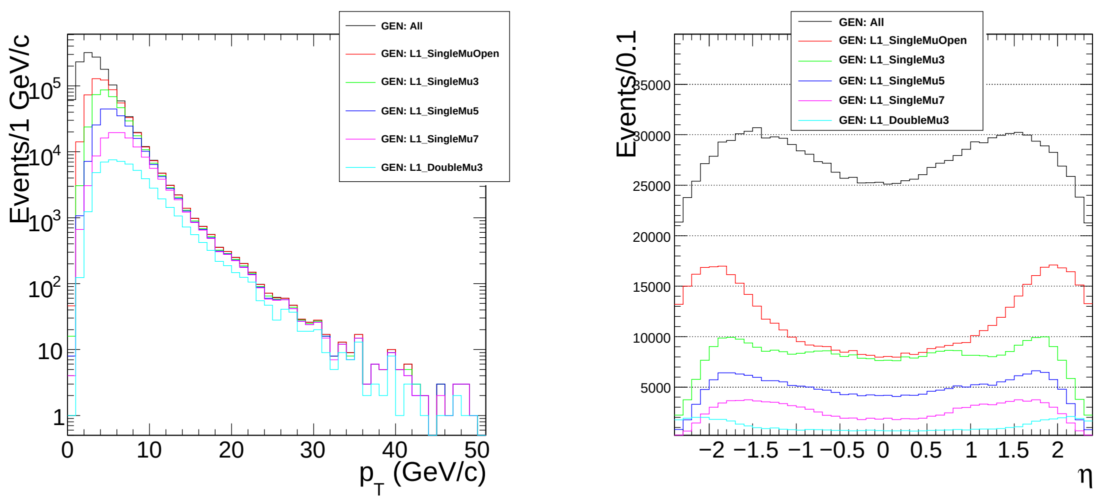

Figure 5.6: p_T (a) and η (b) distribution of J/ψ to be collected by different L1 muon trigger.

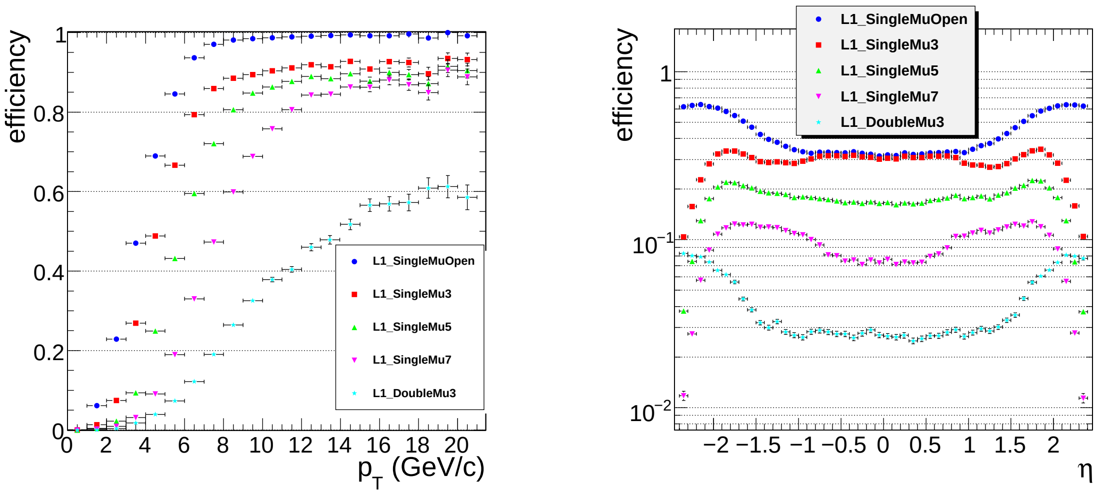

Figure 5.7: (a) Level-1 J/ψ trigger efficiencies as a function of $p_T^{J/\psi}$, integrated over the pseudorapidity range $|\eta_{J/\psi}| < 2.4$; (b) Level-1 J/ψ trigger efficiencies as a function of $\eta_{J/\psi}$, integrated over all the p_T range.

5.2.2 J/ψ trigger rates and expected statistics

For instantaneous luminosities of 8×10^{32} and 10^{31} $\mathrm{cm}^{-2}\mathrm{s}^{-1}$, the rates of J/ψ events are shown in Tabs. 5.2 and 5.3. For the higher luminosity, the total event rate of the HLT J/ψ trigger for signal and backgrounds is 0.261 Hz, which is much

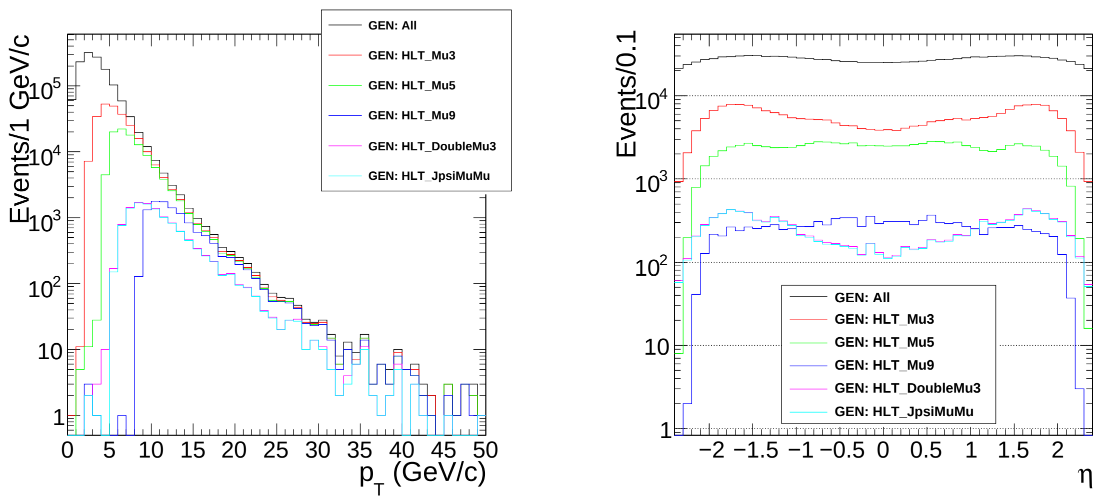

Figure 5.8: p_T (a) and η (b) distribution of J/ψ to be collected by different L1 muon trigger.

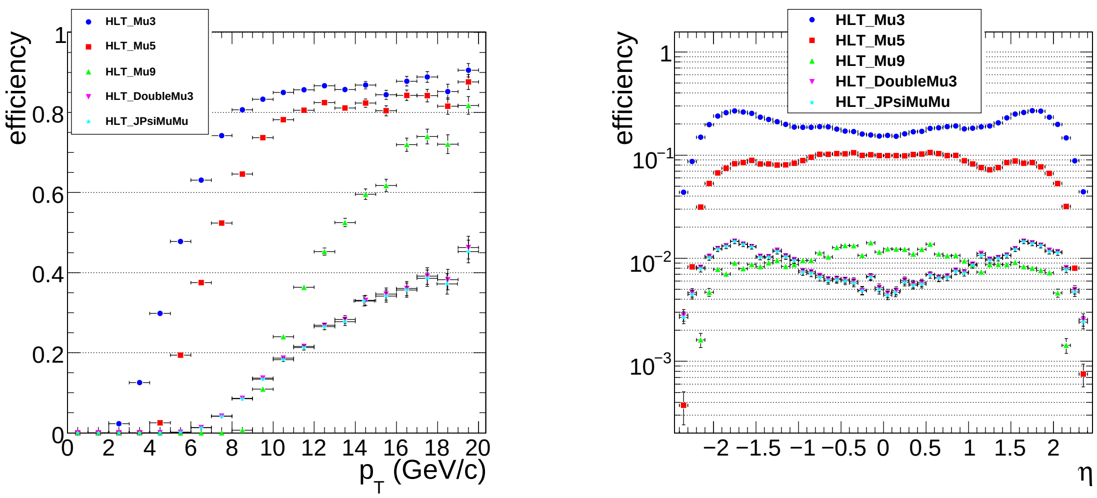

Figure 5.9: (a) Combined L1+HLT J/ψ trigger efficiencies as a function of $p_T^{J/\psi}$, integrated over the pseudorapidity range $|\eta_{J/\psi}| < 2.4$; (b) Combined L1+HLT J/ψ trigger efficiencies as a function of $\eta_{J/\psi}$, integrated over all the p_T range.

smaller than the maximum allowed HLT output rate, ∼100 Hz. Even in further increasing luminosity, i.e. 10^{32} cm^{-2}s^{-1}, the J/ψ trigger still has a small event rate and can be unsprescaled. Therefore, we can collect as much as possible J/ψ events to used for the detector alignment and calibration.

Fig. 5.10 shows the integral luminosities as a function of time in the pp operation during 2009-2010, according to the latest LHC schedule. About 200 $\mathrm{pb}^{-1}$of pp collision data will be collected in the first year. Assuming the two HLT menus in previous section will be used and the menu switches when luminosity reaches 10^{31} $\mathrm{cm}^{-2}\mathrm{s}^{-1}$, the number of J/ψ events to be collected by different trigger paths as a function of time can be roughly estimated as in Fig. 5.11, taking account the event rates and prescale factors in Tabs. 5.2 and 5.3.

After two month of operation in the low luminosity mode, the CMS experiment will accumulate around $3\mathrm{pb}^{-1}$ of data. Assuming the first HLT menu is used in this scenario, about 700k J/ψ events will collected by the single muon trigger with the lowest threshold of $p_T^\mu > 3GeV/c$, which is the ideal trigger path to be used for the first J/ψ cross section measurement. After the switch of the HLT menu, the double muon trigger with threshold of $p_T^\mu > 3GeV/c$ will give the highest event rates. Total $\sim$5M J/ψ events could be written on the tape in the first year.

HLT path	Prescale	Prompt J/ψ	B-decay J/ψ	Background	Total
HLT_Mu3	1	0.256	0.0838	15.6	15.9
HLT_Mu5	1	0.107	0.0472	6.23	6.38
HLT_Mu9	1	0.0116	0.00886	0.814	0.834
HLT_DoubleMu3	1	0.0120	0.00793	0.122	0.142
HLT_JPsi	1	0.0117	0.00630	0.00294	0.0209

Table 5.2: The unprescaled rates and prescale factors of HLT trigger selection for prompt, non-prompt J/ψ and background events, at an instantaneous luminosity of 8×10^{28} $\mathrm{cm}^{-2}\mathrm{s}^{-1}$.

HLT path	Prescale	Prompt J/ψ	B-decay J/ψ	Background	Total
HLT_Mu3	infinity	3.20	1.05	195	None
HLT_Mu5	25	1.34	0.590	77.4	79.8
HLT_Mu9	1	0.145	0.111	10.2	10.5
HLT_DoubleMu3	1	0.150	0.099	1.53	1.78
HLT_JPsi	1	0.146	0.079	0.037	0.261

Table 5.3: The unprescaled rates and prescale factors of HLT trigger selection for prompt, non-prompt J/ψ and background events, at an instantaneous luminosity of 10^{31} cm^{-2}s^{-1}.

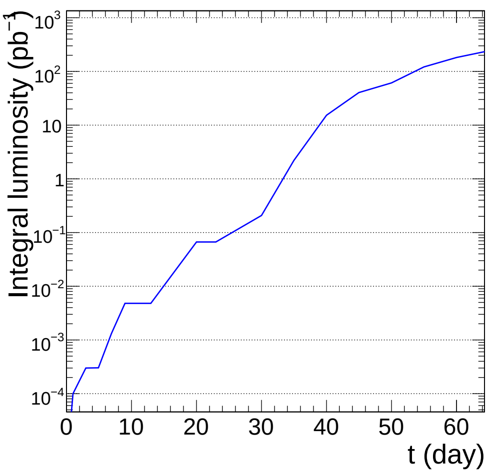

Figure 5.10: The integral luminosities as a function of time in 2009-2010, according to the latest plan of LHC operation [88].

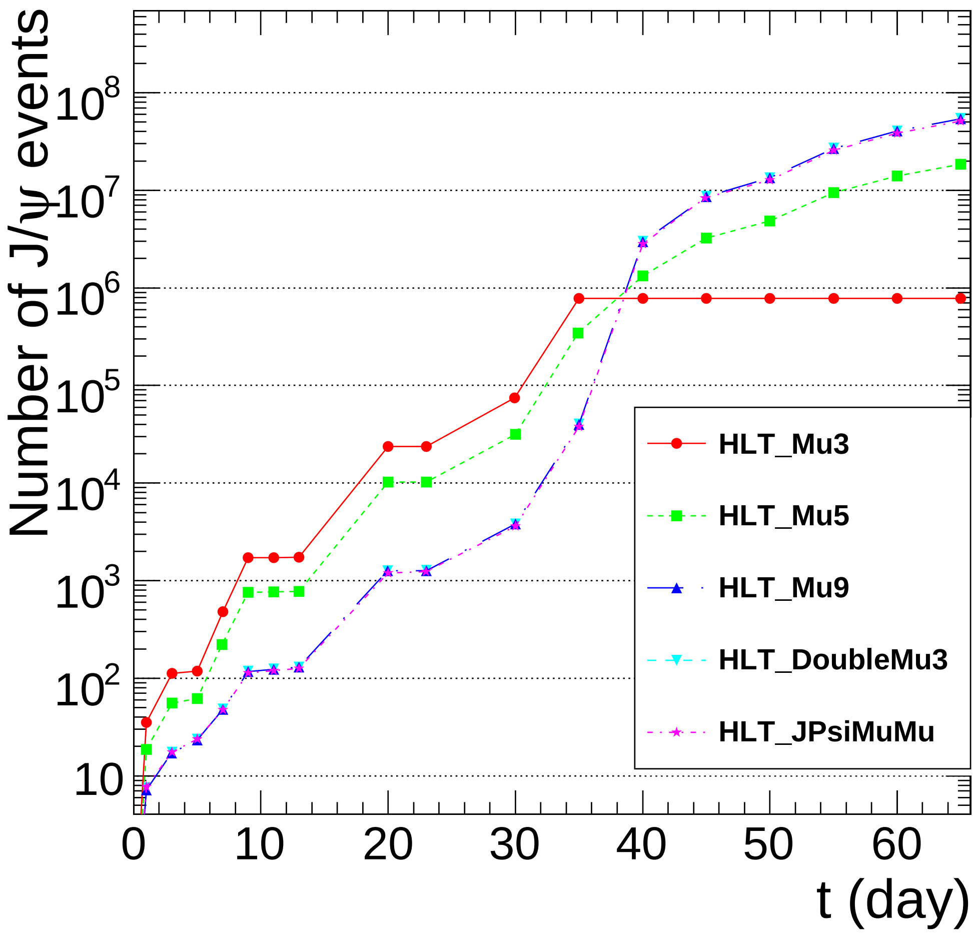

Figure 5.11: Estimation of the number of J/ψ events collected by different trigger paths as a function of time, including both prompt and non-prompt J/ψ.

Chapter 6

Muon and J/ψ reconstruction performance

Before discussing the selection criteria for J/ψ-events, it is important to understand the characteristics of the muons coming from J/ψ-decays, as well as the performance for single muon and J/ψ-reconstruction. In Ref. [89] the muon and dimuon reconstruction efficiency was already studied, but in the ORCA framework. Here, we study the performance for muon reconstruction in CMSSW.

6.1 Single muon reconstruction

6.1.1 Offline muon reconstruction

Muon reconstruction in CMS is described in detail in Ref. [63]. The muon candidates are reconstructed and identified with the GlobalMuonProducer algorithm in CMSSW, based on independent reconstruction of a muon in a standalone muon system and matching it with a track of similar kinematic parameters in the tracker, as shown in Fig. 6.1.

Track Reconstruction Due to the complexity of the CMS tracker, which consists of thousands of detector units, and the large multiplicity of tracks in high-energy

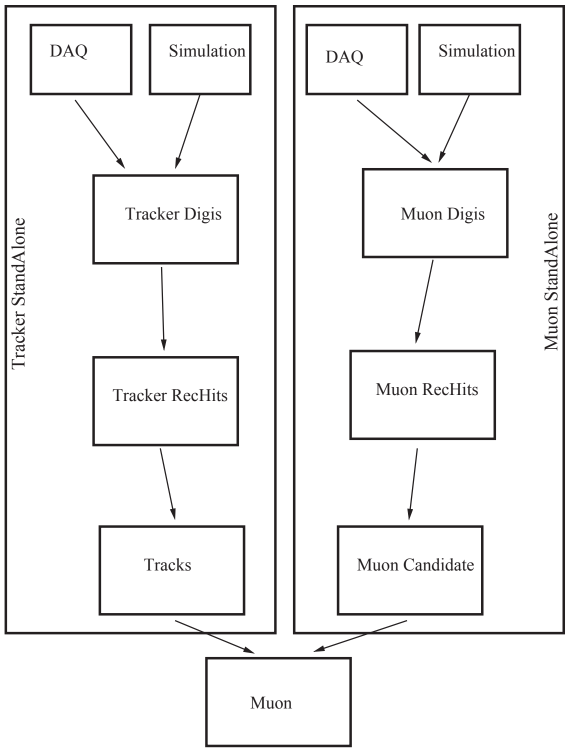

Figure 6.1: Algorithm to produce a muon using information from Tracker and Muon Systems.

pp collisions at the LHC, different algorithms are used in CMS for track reconstruction, each optimized for a special task may be needed. All methods use the reconstructed positions (hits) of the passage of charged particles in the silicon detectors to determine the helix trajectories of the charged tracks and therefore measure their directions and momenta. The main standard algorithm designed for the reconstruction of proton-proton collisions is the Combinatorial Track Finder (CTF). The CTF proceeds in three stages: seeding, finding and fitting. The basic algorithm for fitting the track parameters is using the Kalman filter [49] technique. However, due to the flexibility of the CMS track reconstruction framework, more advanced algorithms such as a Deterministic Annealing Filter or a Multi Track Filter (see [41] and references therein) were successfully implemented as well.

Standalone muon reconstruction Reconstruction in the Muon system is often called "Standalone muon" since it does not make use of Tracker hits; and it is also used in the Level 2 trigger algorithms. The reconstruction makes use of the track hits and track segments from the local reconstruction step in the individual muon subdetector modules of the CSC, DT, and RPC detectors. The algorithm starts from the locally-reconstructed muon track segments. A segment in one of the innermost detector stations (those closest to the interaction point) is used as a seed for a Kalman filter, which builds trajectories in the radially-increasing direction. A χ^2 cut is applied to reject hits unlikely to be associated with the track, which can arise from showering, delta rays, and pair production. The trajectory is propagated using a detailed map of the magnetic field and taking account of energy loss in the detector material (mainly the steel of the magnet return yoke), until the outermost detector layer of the Muon system is reached. A backward Kalman filter is then applied, working from outside in, and the track parameters are defined at the innermost muon station. Finally, the track is extrapolated to the nominal interaction point and a vertex-constrained fit to the track parameters is performed. In this fit, since the magnetic field is inhomogeneous and nonuniform in the 2 end-cap regions, the two-dimensional hits in CSC layers are used instead of the track segments which were used for seeding.

Global muon reconstruction The global muon reconstruction consists in extending the muon trajectories to include hits in the silicon tracker (silicon strip and silicon pixel detectors). The first step is to identify the silicon tracker track to combine with the standalone muon track, so called track matching. The matching of two disjoint tracks is performed by comparing the 5 parameters describing the trajectory, this is best done by propagating the tracks onto a common reference point or surface, taking into account the muon energy loss in the material and the effect of multiple scattering. After the selection of a subset of tracker tracks that match the stand-alone muon track, the next step in making a global muon track is to fit a track using the hits from the tracker track and the stand-alone muon track. The global refit algorithm attempts to perform a track fit for each tracker track -

stand-alone muon pair. If, after the fit is attempted for each pair, there is more than one possible global muon track, the global muon track with the best χ^2 is chosen. Thus, for each stand-alone muon there is a maximum of one global muon that will be reconstructed.

6.1.2 Muon reconstruction efficiency

The η-coverage for muon reconstruction in the CMS detector is $|\eta_\mu| < 2.4$. The performance of single muon reconstruction was described in Ref. [63] for muons in the range p_T^μ=10-1000 GeV/c. However, muons from J/ψ decays have generally lower $p_T^\mu$and mostly reconstructed at endcap region, as can be seen in Fig. 6.2.

The muon reconstruction efficiency depends on p_T^μ and η_μ and is determined by comparing the reconstructed muon with the information at the generator level. The muon originating directly from the J/ψ decay is identified via the information provided by the event generator. The angular variable $\Delta R = \sqrt{\Delta\eta^2 + \Delta\phi^2}$ is determined between each reconstructed muon identified with the correct electric charge in the final state and the generated muon from the J/ψ decay. The distribution of this variable ΔR is shown in Fig. 6.3 for all reconstructed global muon candidates. The reconstructed muons in the final state are categorized as being correctly reconstructed when ΔR is smaller than 0.2 and $\Delta p_T^\mu / p_T^\mu < 0.2$.

We define the μ reconstruction efficiency as

$$\epsilon_{muon} = \frac{N_{rec}^\mu}{N_{gen}^\mu}, \tag{6.1}$$

where N_{gen}^μ is the number of generated muons, and N_{rec}^μ is the number of reconstructed muons passing the matching criteria described above. Thus, the μ reconstruction also takes into account the detector acceptance.

Global reconstruction requires the matching of reconstructed tracks in both the muon system and the tracker and the overall efficiency is a product of the stand-alone, the tracker track and the matching efficiencies. Figs. 6.4 and 6.5 respectively show the results for reconstructing single muons from J/ψ decays as a function of

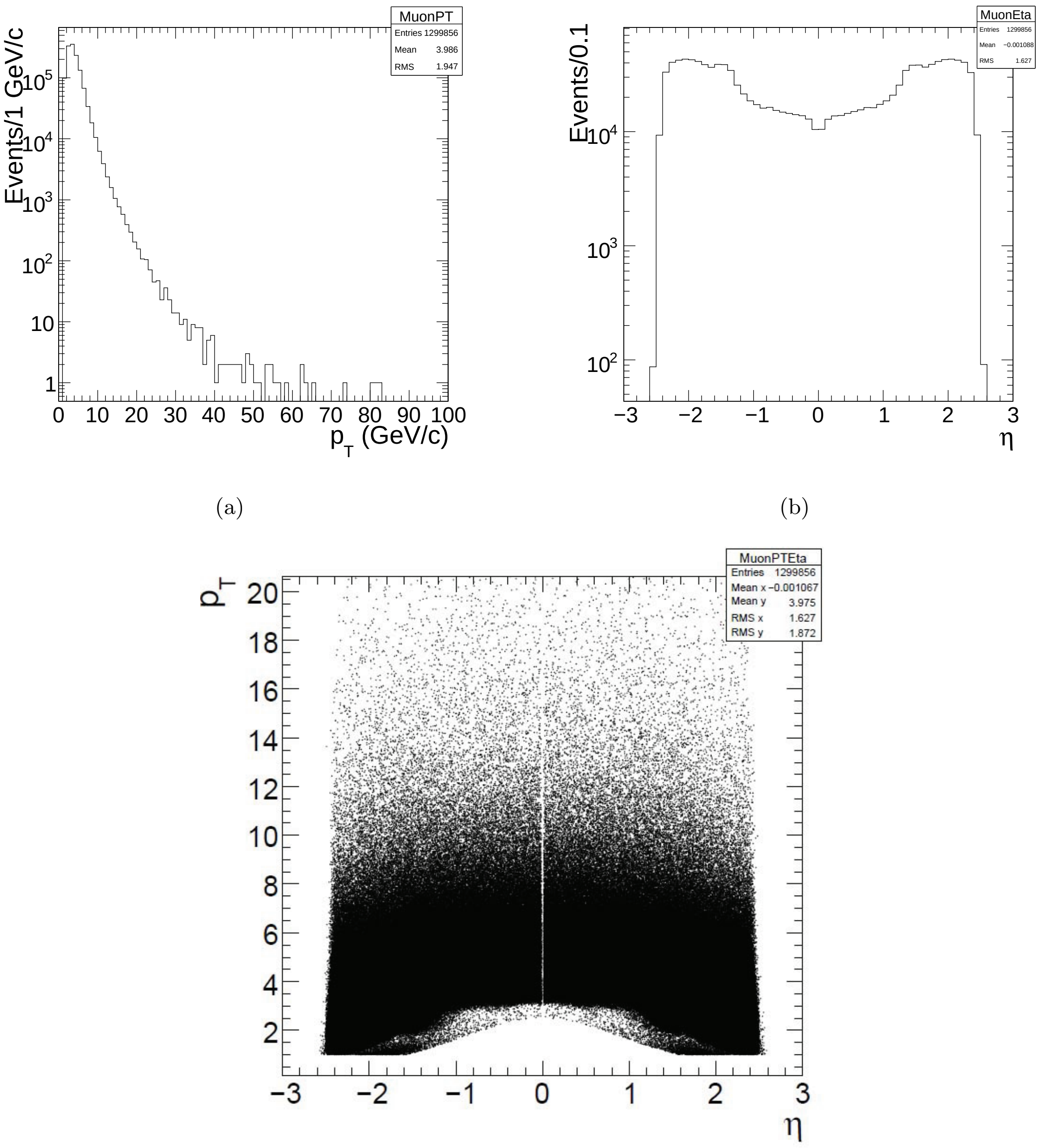

(a) (b) (c)

Figure 6.2: The η_μ (left) and p_T^μ (right) 2D distributions of muon and prompt J/ψ for reconstructed J/ψ events.

the p_T and η of the muon. Most of the muons with $p_T^\mu < 4$ GeV/c cannot reach the barrel muon chambers (corresponding to the region of $|\eta_\mu| < 1.2$), so the efficiency is very low in that region. The reconstruction efficiency for muons drops at several

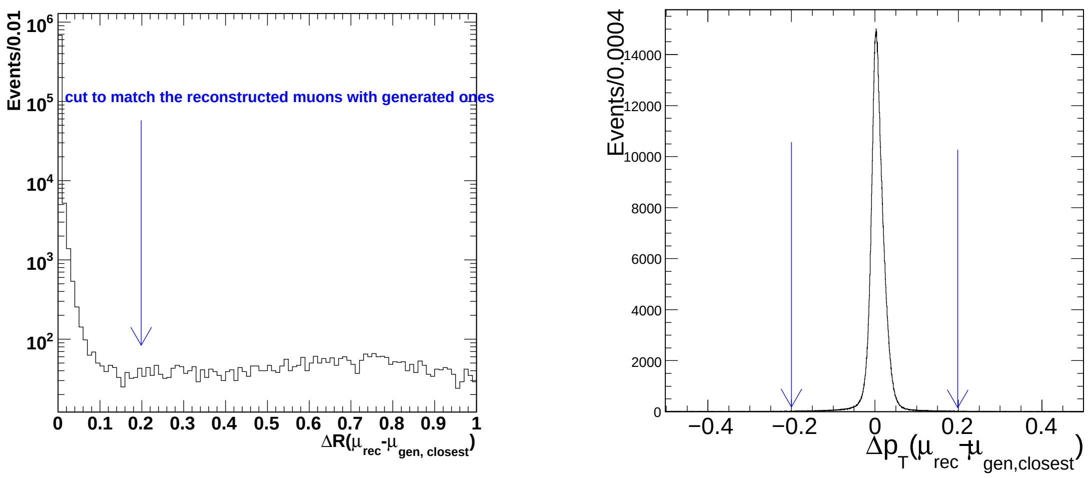

Figure 6.3: $\Delta R = \sqrt{\Delta\eta^2 + \Delta\phi^2}$ distribution of the Monte Carlo truth muon and the reconstructed muon from prompt J/ψ events.

pseudorapidity regions: e.g. around $|\eta_\mu| = 0.25$ and 0.75 (the regions between two wheels) and around $|\eta_\mu| = 1.2$ (where the DT and CSC systems overlap), and around $\eta_\mu = 1.7 \sim 1.8$ (where there are gaps in the CSC system). The maximum efficiency, which is about 90%, is reached for p_T^μ >7 GeV/c, for any η_μ. The momentum resolution of muons is at the percent level.

The fraction of pions or kaons originating from the p-p interaction that are reconstructed as muons (fake rate) is about 0.3%. The majority of those are coming from genuine muons from pion and kaon decays occurring before the measuring muon stations, either in the tracker volume or after it.

6.1.3 Muon tracking performance

Figs. 6.6, 6.8and **??** show the residuals of transverse momentum as a function of pseudorapidity in p_T bins for muons obtained with the global reconstruction algorithm. The transverse momentum resolution was evaluated by a Gaussian fitting to the distribution of the quantity

$$\frac{1/p_T^{rec} - 1/p_T^{gen}}{1/p_T^{gen}}, \tag{6.2}$$

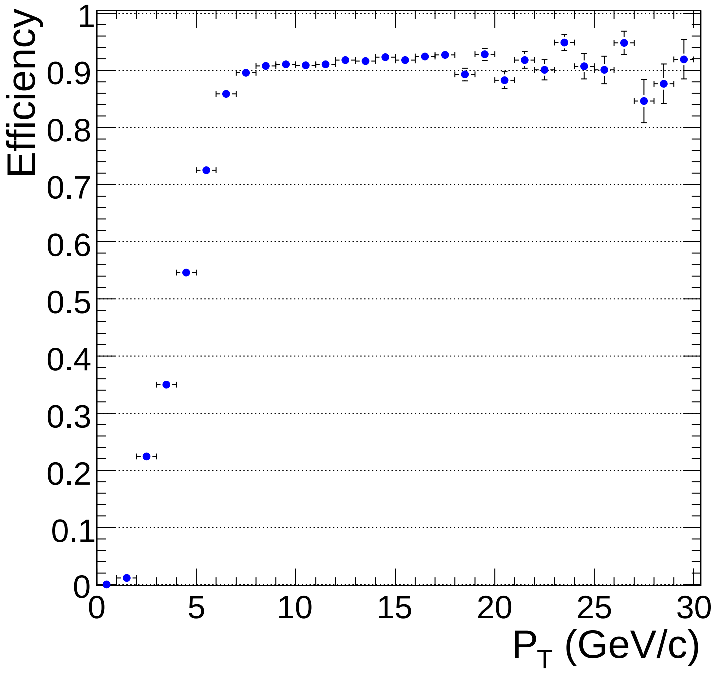

Figure 6.4: Muon reconstruction efficiency vs. p_T^μ for muons with $|\eta_\mu| < 2.5$.

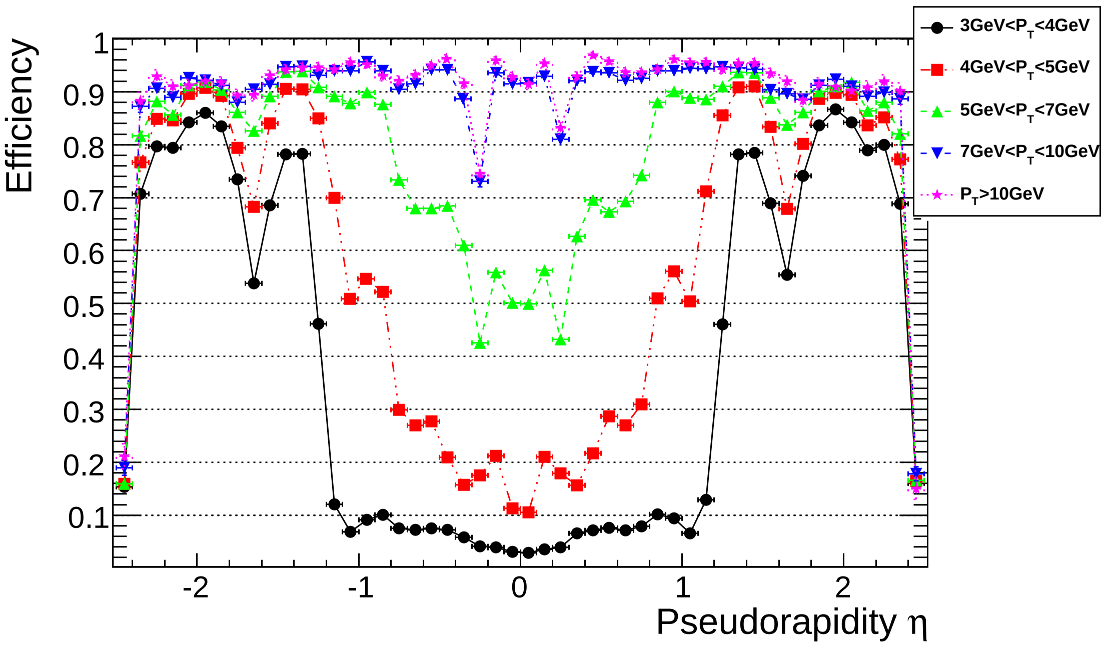

Figure 6.5: Muon reconstruction efficiency vs. η_μ at different $p_T^{J/\psi}$.

where p_T^{rec} and p_T^{gen} are the closest transverse momenta of generated and reconstructed good muons. Figs. 8-10 are several examples of the Gaussian fitting.

The p_T resolutions in Fig. 6.9 are consist with the ones in [10, 11] at most points, deteriorating while the η grows.

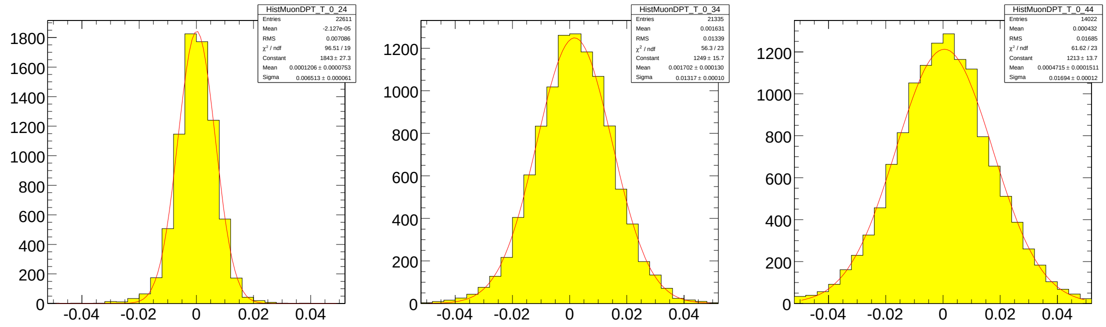

Figure 6.6: $1/p_T$ resolution for global muons with $3GeV/c < p_T^{\mu} < 4GeV/c$, shown in three η_μ bins: (a)$0.1 < \eta_\mu < 0.2$, (b) $1.1 < \eta_\mu < 1.2$ and (c) $2.1 < \eta_\mu < 2.2$.

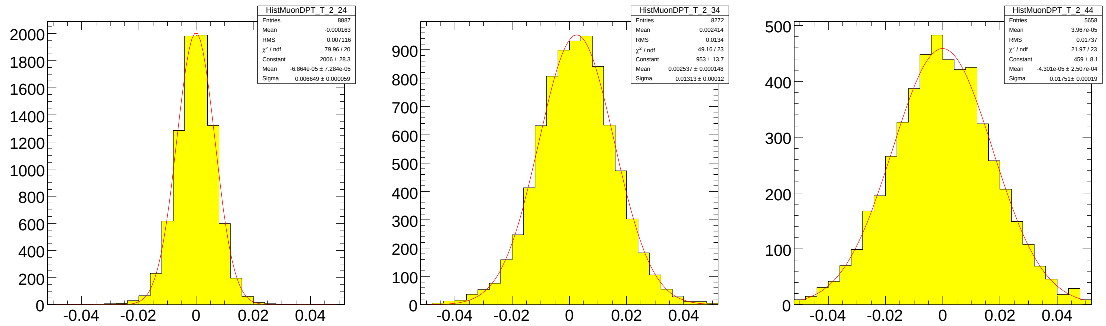

Figure 6.7: $1/p_T$ resolution for global muons with $5GeV/c < p_T^{\mu} < 7GeV/c$, in the same η_μ bins as Fig.8.

Fig 6.10 (6.11) is the $\eta(\phi)$ resolution as a function of pseudorapidity in five p_T bins for muons. The $\eta(\phi)$ resolution was obtained by a Gaussian fitting to the distribution of $\eta(\phi)$ residuals

$$\Delta(\eta) = \eta_{rec} - \eta_{gen}, \tag{6.3}$$

$$\Delta(\phi) = \phi_{rec} - \phi_{gen}, \tag{6.4}$$

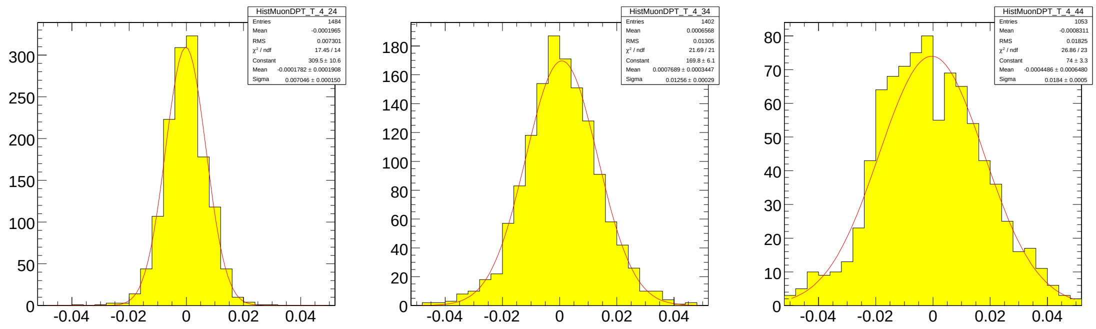

Figure 6.8: $1/p_T$ resolution for global muons with $p_T^\mu > 10GeV/c$, in the same η_μ bins as Fig.8.

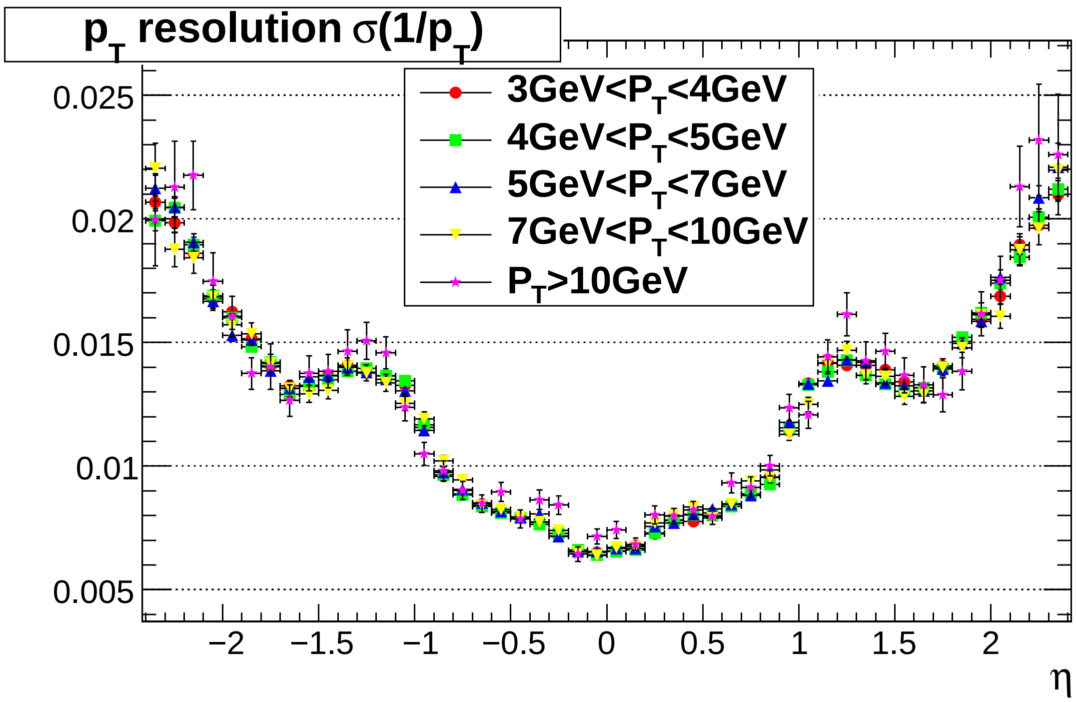

Figure 6.9: $1/p_T$ resolution for global reconstructed muons as a function of pseudorapidity.

where $\eta_{rec}(\phi_{rec})$ and $\eta_{gen}(\phi_{gen})$ are the closest pseudorapidity (ϕ angle) between the generated and the reconstructed good muons. The $\eta(\phi)$ resolution is also consist with the ones in [11], deteriorating while the pseudorapidity grows.

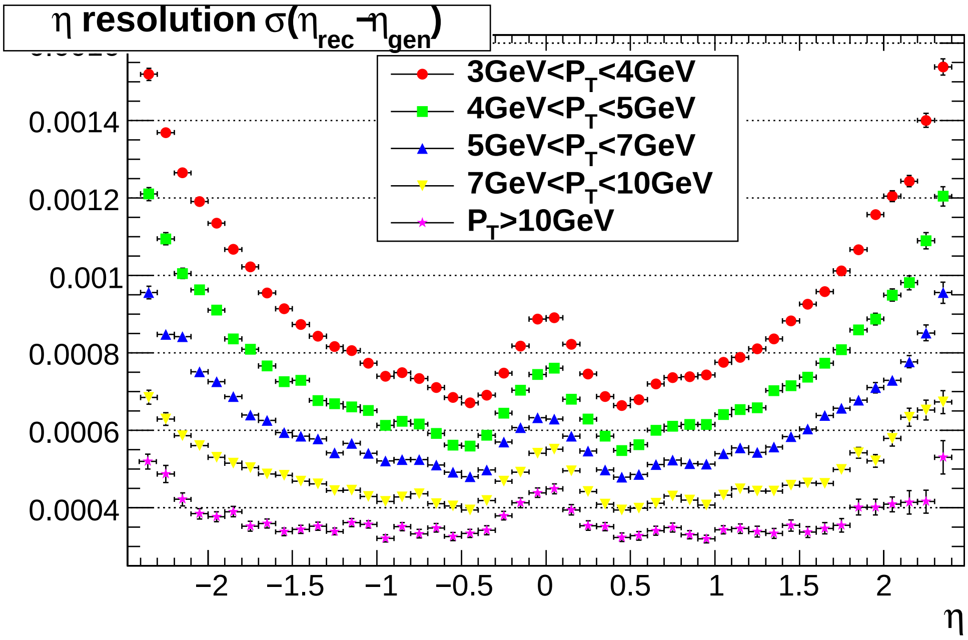

Figure 6.10: η resolution for global reconstructed muons as a function of pseudorapidity.

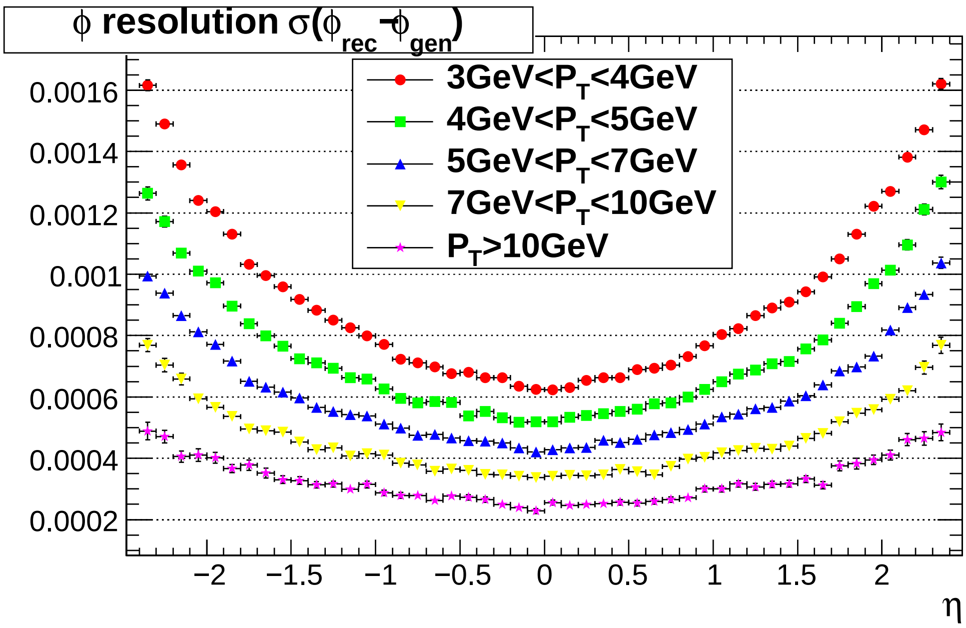

Figure 6.11: ϕ resolution for global reconstructed muons as a function of pseudorapidity.

6.2 J/ψ selection and reconstruction

6.2.1 J/ψ event selection

J/ψ candidates are reconstructed by pairing muons with at least 3 GeV/c transverse momentum and opposite charge. The invariant mass of the muon pair is required to be between 2.8 and 3.4 GeV/c^2. Furthermore, the two muons should come from a common vertex, which is determined by the point of their closest approach in space by using the KalmanVertexFitter [90, 91]. It must be noted that the efficiency of this vertex requirement in the Monte Carlo sample of prompt J/ψ is 0.9996 ± 0.0001.

The p_T and η distributions of selected J/ψ candidates are shown in Fig. 6.12. Most of the candidates have low $p_T^{J/\psi}$ and large η.

6.2.2 J/ψ mass resolution and bias

The mean value and mass resolution ($=\frac{\sigma(m)}{\text{mean}}$) of the J/ψ's invariant mass are investigated in regions of $p_T^{J/\psi}$ and $\eta_{J/\psi}$ for prompt J/ψ's. Fig. 6.13, 6.14 and 6.15 show examples of the J/ψ invariant mass distribution in different $\eta_{J/\psi}$ and $p_T^{J/\psi}$ bin, fitted with a single Gaussian. The mean value and mass resolution as a function of $\eta_{J/\psi}$ and $p_T^{J/\psi}$ can be seen in Figs. 6.16 and 6.17. It can be noted that the mean values are generally around the world average value 3.096 GeV/c^2, no significant dependence on p_T or η. The mass resolution is smaller at high $p_T^{J/\psi}$ and at small $\eta_{J/\psi}$. The smaller resolution with increasing $p_T^{J/\psi}$ is counter-intuitive, but explained by the fact that J/ψ's with higher transverse momenta are produced more centrally, where the resolution is better.

Since the mass resolution is a function of $p_T^{J/\psi}$ and $\eta_{J/\psi}$, one simple Gaussian function is not suitable to fit the J/ψ signal peak. We anticipate to fit in bins of $p_T^{J/\psi}$, and will use two Gaussian functions to allow for the different resolutions due to the $\eta_{J/\psi}$ dependence of the resolution.

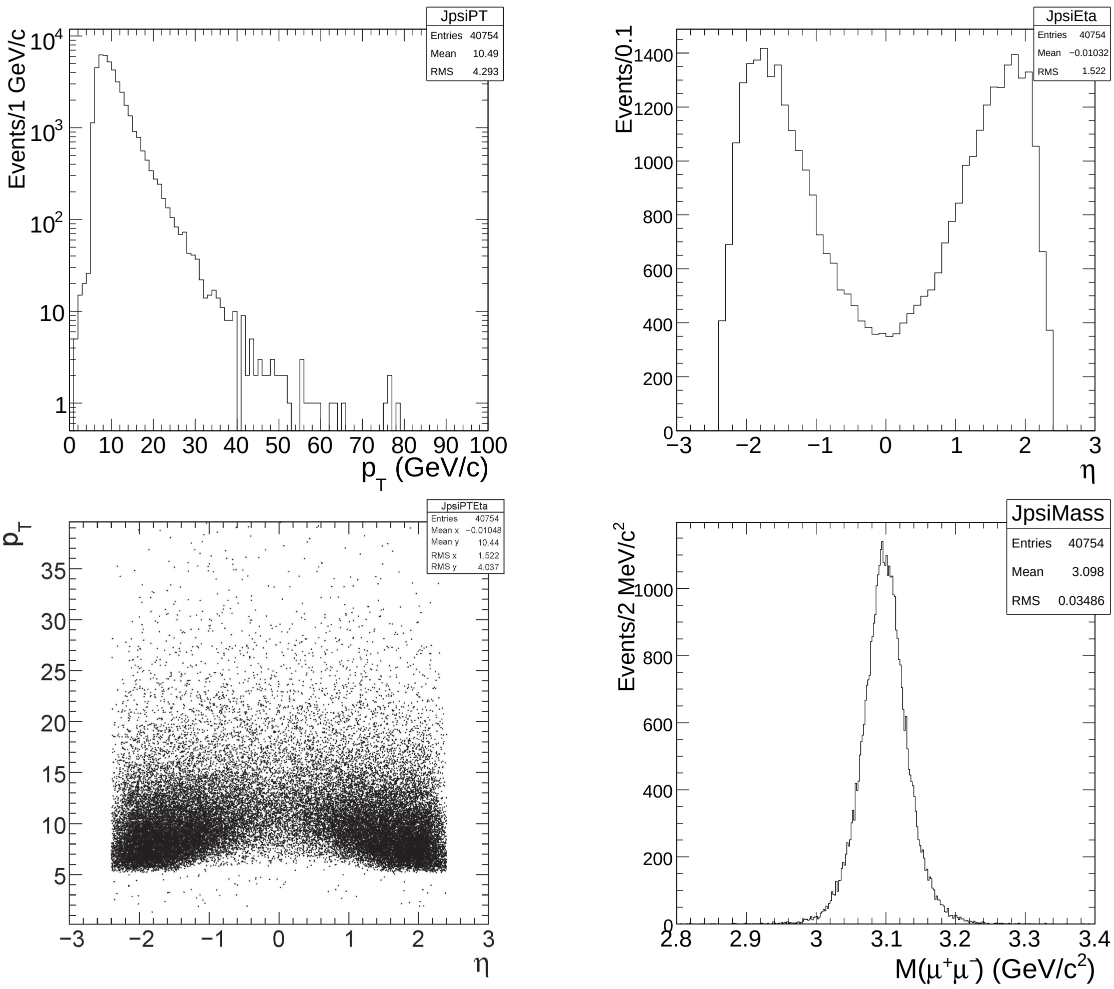

Figure 6.12: The η_μ (left) and p_T^μ (right) 2D distributions of muon and prompt J/ψ for reconstructed J/ψ events.

6.2.3 J/ψ mass spectrum

The dimuon mass spectrum including background and signal is given in Fig. 6.18. The level of the Drell-Yan background in the same mass window is computed to be less than a percent with respect to the other background sources, and hence neglected from now on. Concerning the background source coming from two fake muons, this is of the order of 10% with respect to the muon enriched QCD background, and is taken into account as systematic uncertainty.

Given the invariant mass spectrum, the number of J/ψ candidates, $N^{fit}_{J/\psi}$ in each

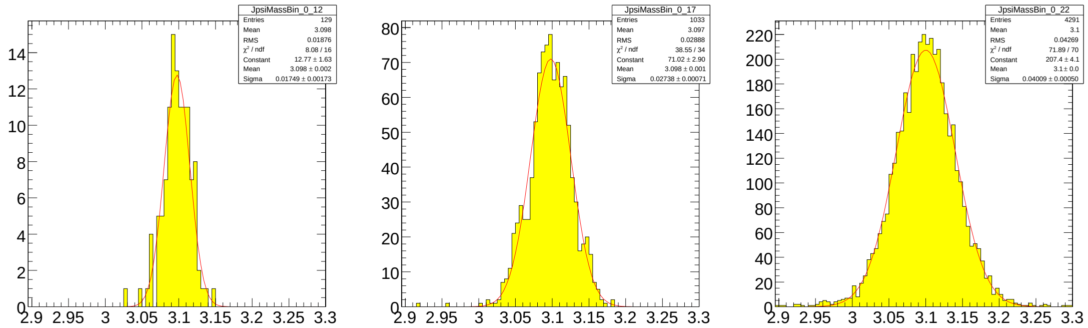

Figure 6.13: Invariant mass distribution of J/ψ with $p_T^{J/\psi} > 15$ GeV/c, in three $\eta_{J/\psi}$ bins: $0.0 < \eta_{J/\psi} < 0.2$ (a), $1.0 < \eta_{J/\psi} < 1.2$ (b), and $2.0 < \eta_{J/\psi} < 2.2$ (c) .

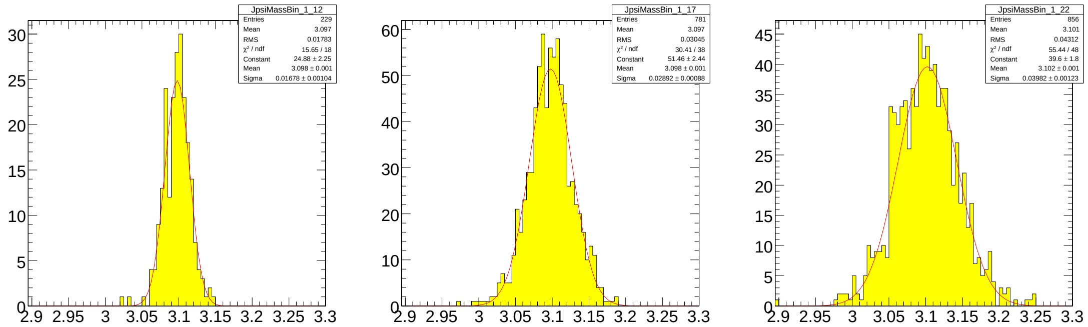

Figure 6.14: Invariant mass distribution of J/ψ with $p_T^{J/\psi} > 15$ GeV/c, in the same $\eta_{J/\psi}$ bins as Fig.8..

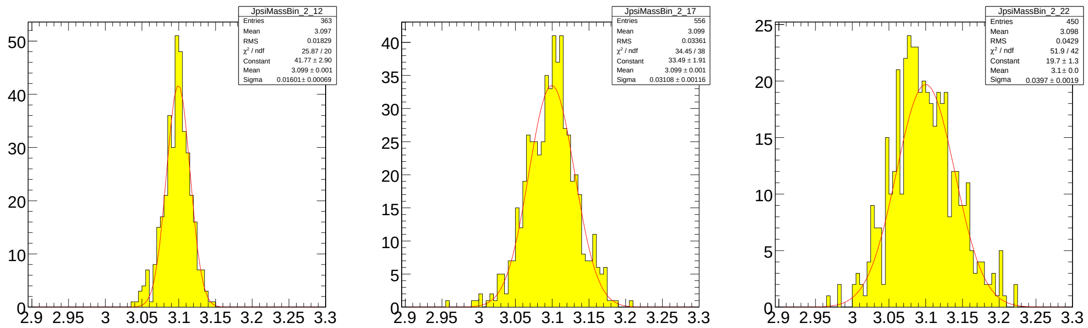

Figure 6.15: Invariant mass distribution of J/ψ with $p_T^{J/\psi} > 15$ GeV/c, in the same $\eta_{J/\psi}$ bins as Fig.8.).

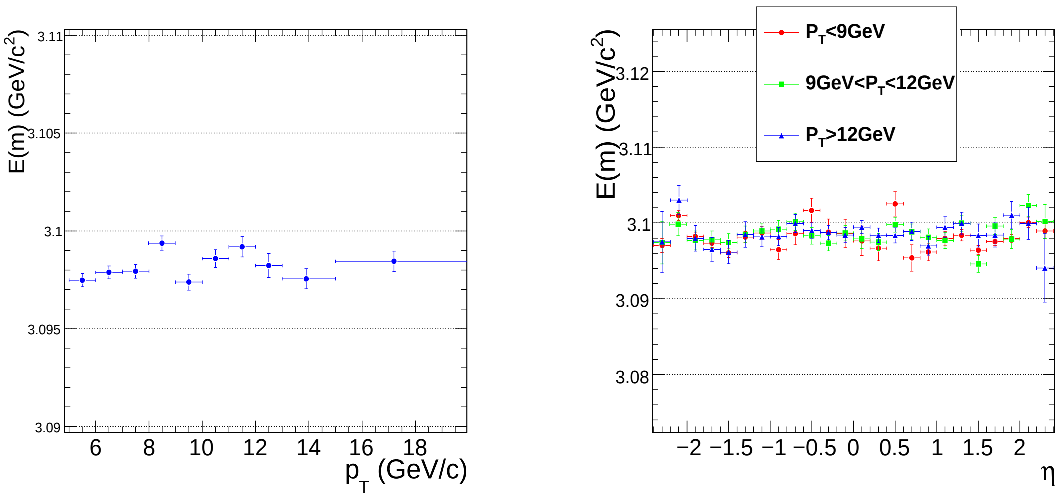

Figure 6.16: Mean value of J/ψ invariant mass as a function of $p_T^{J/\psi}$ (a) and $\eta_{J/\psi}$ (b).

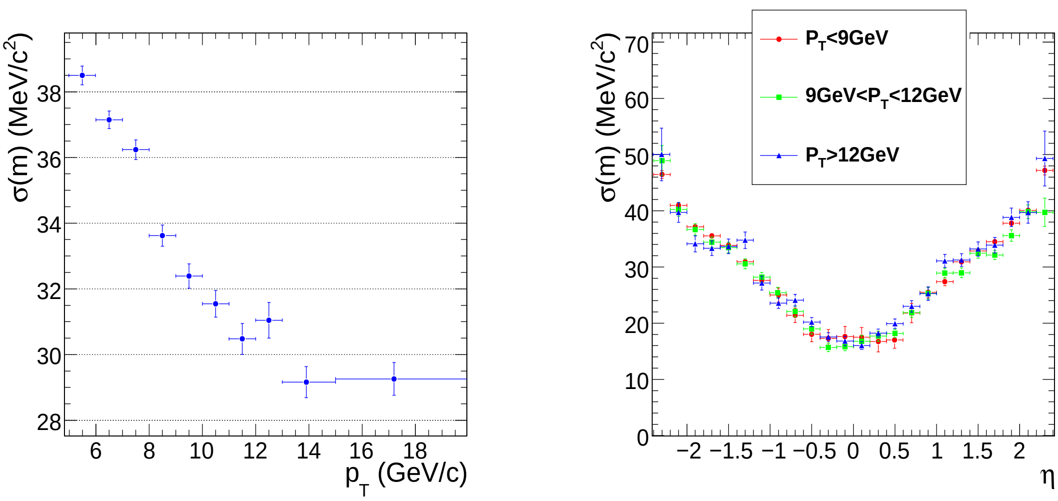

Figure 6.17: Gaussian width of J/ψ invariant mass as a function of $p_T^{J/\psi}$ (a) and $\eta_{J/\psi}$ (b).

$p_T^{J/\psi}$ bin can be obtained by fitting the dimuon invariant mass distribution with a background hypothesis and a signal hypothesis. As anticipated in Section 6.2.2, the J/ψ invariant mass distribution is better described as a sum of two Gaussian functions, rather than a single Gaussian. This can be seen from Figs. 6.19 and 6.20, where the signal and background are displayed together and fitted with a linear background and a single and double gaussian for the signal. The background invariant mass distribution is indeed well described by a linear function, as can be seen from Fig. 6.21, where the background is displayed alone.

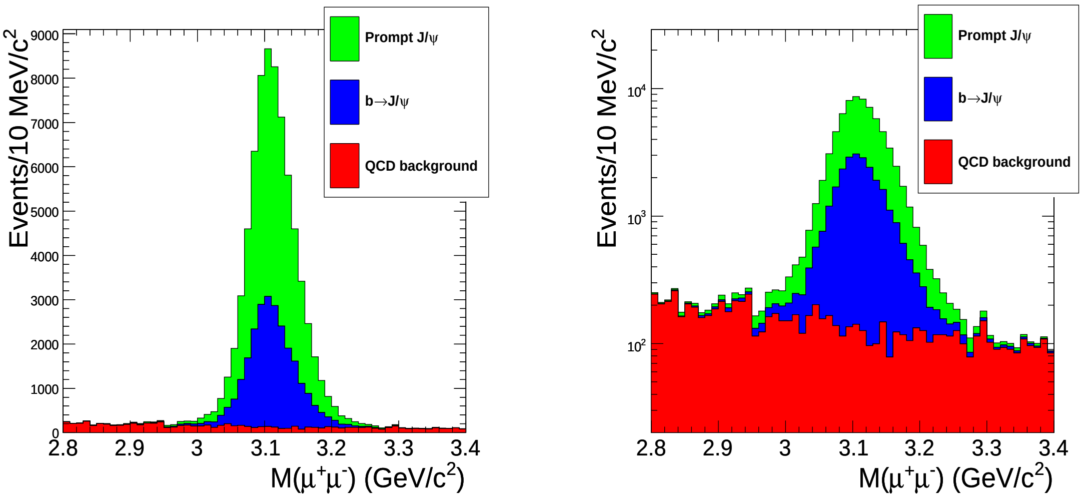

Figure 6.18: Dimuon invariant mass distribution normalized to 3 pb^{-1} in linear (left) and logarithmic (right) scale. The green (light grey), blue (black) and red (dark grey) areas are the prompt, non-prompt and QCD background contributions, respectively.

6.2.4 J/ψ reconstruction efficiency with respect to filtered events

A useful quantity is the J/ψ reconstruction efficiency $\epsilon^{filt}_{J/\psi}$ with respect to the number of filtered events (for filter see Sect. **??**):

$$\epsilon^{filt}_{J/\psi}(p_T^{J/\psi}, \eta_{J/\psi}) = \frac{N^{fit}_{J/\psi}(p_T^{J/\psi}, \eta_{J/\psi})}{N^{gen+filt}_{J/\psi}(p_T^{J/\psi}, \eta_{J/\psi})}, \tag{6.5}$$

where $N^{fit}_{J/\psi}$ is the number of fitted J/ψ's in a certain $p_T^{J/\psi}$-bin as explained in Sec. 6.2.3, and $N^{gen+filt}_{J/\psi}$ is the number of *generated and filtered* J/ψ's in this region. The efficiency $\epsilon^{filt}_{J/\psi}$ as a function of $p_T^{J/\psi}$ and $\eta_{J/\psi}$ are shown in Fig. 6.22. From this figure we see that $\epsilon^{filt}_{J/\psi}$ is up to 80% at high $p_T^{J/\psi}$and high $\eta_{J/\psi}$. Below $p_T^{J/\psi}$=5 GeV/c it drops dramatically to zero. At low $\eta_{J/\psi}$, the value of $\epsilon^{filt}_{J/\psi}$ is smaller than at

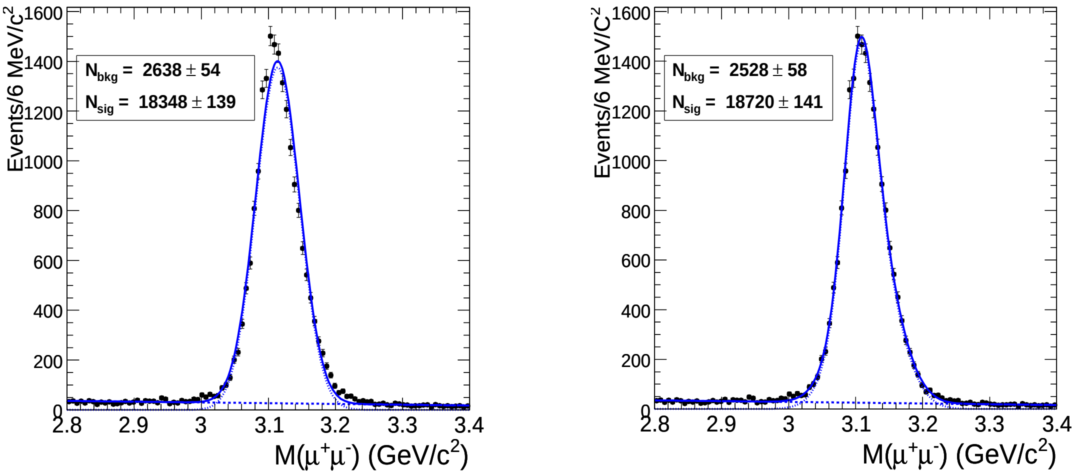

Figure 6.19: Left: mass distribution fit of background and signal fitted with a linear function and a single Gaussian in the $p_T^{J/\psi}$ range of 9 GeV/c< $p_T^{J/\psi}$ < 10 GeV/c. Right: the same, but with the signal fitted to a double Gaussian.

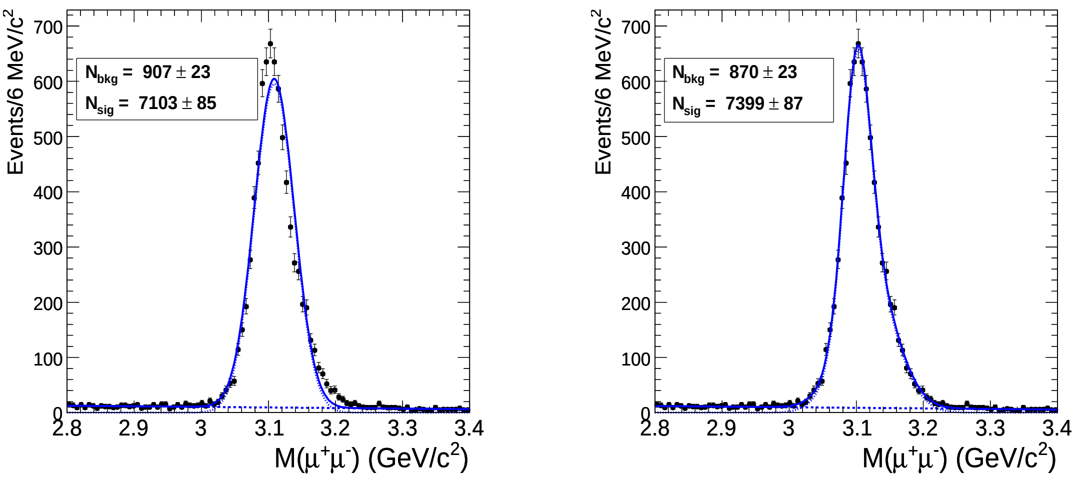

Figure 6.20: Left: mass distribution fit of background and signal fitted with a linear function and a single Gaussian in the $p_T^{J/\psi}$ range of 17 GeV/c< $p_T^{J/\psi}$ < 20 GeV/c. Right: the same, but with the signal fitted to a double Gaussian.

high $\eta_{J/\psi}$ when looking at the same value of $p_T^{J/\psi}$, because the muons have a lower absolute momentum at lower η_μ .

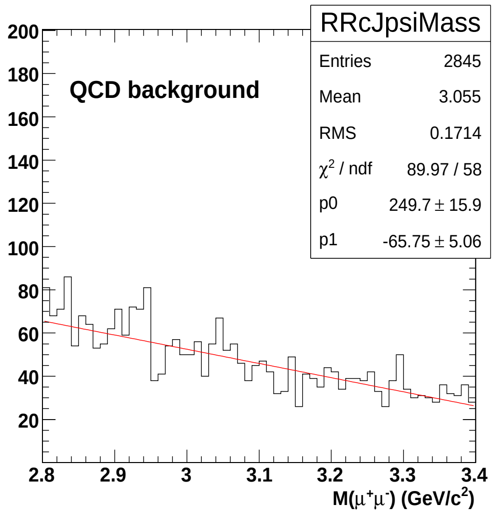

Figure 6.21: Dimuon invariant mass distribution of QCD background, fitted with a first order polynomial function.

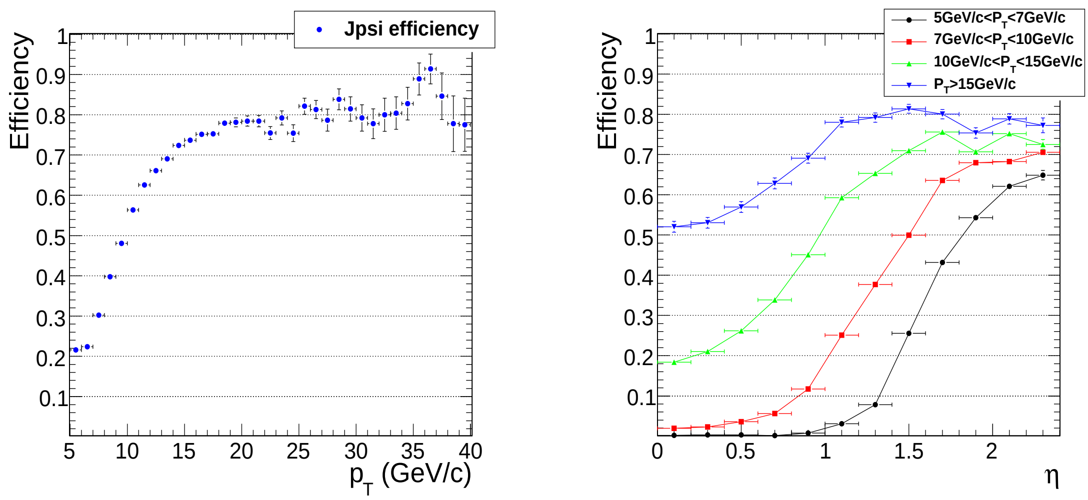

Figure 6.22: Efficiency $\epsilon_{J/\psi}^{filt}$ vs. $p_T^{J/\psi}$ (left) and $|\eta_{J/\psi}|$ (right).

Chapter 7

Measurement of prompt and non-prompt J/ψ cross sections

In this section we will describe the strategy to determine the inclusive J/ψ differential cross section and the procedure and results to obtain both the prompt and the non-prompt components by using the large lifetime of the B-hadron.

7.1 Inclusive J/ψ cross section

The J/ψ differential cross section will be measured in the region $|\eta_{J/\psi}|$ <2.4. It is based on the following expression:

$$\frac{d\sigma}{dp_T}(J/\psi) \cdot Br(J/\psi \to \mu^+\mu^-) = \frac{N^{fit}_{J/\psi}}{\int Ldt \cdot A \cdot \lambda^{corr}_{trigger} \cdot \lambda^{corr}_{reco} \cdot \Delta p_T} \tag{7.1}$$

where

- $N^{fit}_{J/\psi}$ is the number of reconstructed J/ψ candidates in a given p_T bin. This is obtained by fitting the J/ψ mass spectrum with a linear background and double gaussian signal hypothesis, as was explained in Sec. 6.2.3.

- A is the the total efficiency for triggering and offline reconstructing the J/ψ events, as extracted from Monte Carlo. It will be explained in Sec. 7.1.1.

- $\lambda^{corr}_{trigger}$ and λ^{corr}_{reco} are correction factors to the trigger and offline efficiencies, respectively, as measured in data compared to the Monte Carlo simulation , and will be addressed in Sec.7.1.2.1.

- $\int Ldt$ is the integrated luminosity.

- Δp_T is the size of the p_T bin.

Below we discuss A, the correction factors, and the evaluation of the fraction of J/ψ's from B-hadron decay.

7.1.1 Total reconstruction efficiency A

7.1.1.1 Definition of A from Monte Carlo simulation

The relevant quantity for the cross section measurement is the total J/ψ selection efficiency as a function $p_T^{J/\psi}$ and $\eta_{J/\psi}$. It is entirely determined from Monte Carlo and defined as:

$$A(p_T^{J/\psi}, \eta_{J/\psi}) = \frac{N^{rec}_{J/\psi}(p_T^{J/\psi}, \eta_{J/\psi})}{N^{gen}_{J/\psi}(p_T^{J/\psi}, \eta_{J/\psi})}. \qquad (7.2)$$

Here $p_T^{J/\psi}$ and $\eta_{J/\psi}$ are the true value of transverse momentum and pseudorapidity of the generated J/ψ, $N^{rec}_{J/\psi}$ is the number of reconstructed J/ψ's in a region of $\eta_{J/\psi}$ and $p_T^{J/\psi}$, and N^{gen} is the *total* true number of generated J/ψ's, i.e. *before applying the generator dimuon filter.* The definition of the total reconstruction efficiency in Eq. (7.2) *also takes into account the detector acceptance.* It should also be noted that it is *not* the same as the J/ψ reconstruction efficiency defined in Eq. (6.5), which was with repect to the filtered events. Indeed, for a cross section measurement we are interested in the true number of J/ψ's in the η-region $|\eta_{J/\psi}| < 2.4$, not only in the ones passing the filter. The total reconstruction efficiency as a function of p_T is shown in Fig.7.1.

7.1.1.2 Effects of J/ψ polarization

The polarization of the J/ψ affects the decaying muons spectra, and therefore influences the kinematic acceptance in Eq. (7.2). The normalized angular distribution is given by

$$I(\cos\theta) = \frac{3}{2(\alpha+3)}(1+\alpha\cdot\cos^2\theta) \tag{7.3}$$

where θ is the angle between the muon in the J/ψ rest frame and the direction of the J/ψ in the lab frame, and α quantifies the polarization. Fully transverse polarization corresponds to α=+1, fully longitudinal to α=-1, and α=0 indicates no polarization. Fig. 7.1 shows the total reconstruction efficiencies for transverse, longitudinal and no polarization. The difference is about 10% at high p_T and 20% in the low p_T region. Indeed, at low $p_T^{J/\psi}$, the polarization effect is stronger, since there is a muon p_T reconstruction threshold. Once the polarization parameter α is measured, the total reconstruction efficiency can be computed by a weighted sum of the total efficiencies from transversely and longitudinally polarized J/ψ production: $A_\alpha = (1-\eta_\alpha)\cdot A_T + \eta_\alpha \cdot A_L$.

The measurement of the J/ψ polarization is currently under study and a separate analysis note is in preparation. For this cross section measurement we will make use of the polarization measured in other experiments and evaluate the effects of this assumption as a systematic error.

7.1.1.3 Correction factor A'

Due to the detector resolution and the size of the interaction region, some J/ψ's with $\mid \eta^{gen} \mid > 2.4$ can be reconstructed as $\mid \eta^{rec} \mid < 2.4$. This effect should be very small due to the excellent tracking resolution. The relative acceptance A' can be calculated from Monte Carlo and is defined as as:

$$A'(p_T) = \frac{N^{rec}(p_T, \mid \eta^{rec} \mid < 2.4, \mid \eta^{gen} \mid > 2.4)}{N^{gen}(p_T, \mid \eta^{gen} \mid > 2.4)} \tag{7.4}$$

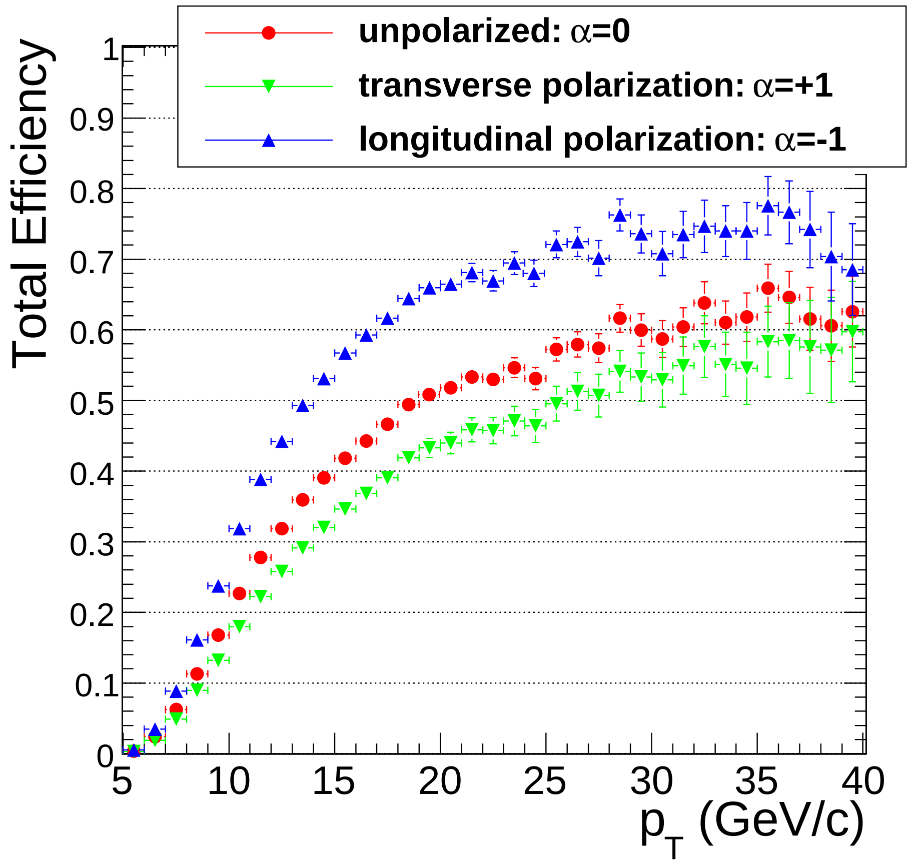

Figure 7.1: Total reconstruction efficiency including detector acceptance as a function of J/ψ p_T: transverse polarization (down-triangle), longitudinal polarization (up-triangle) and unpolarized production (dot).

where $N^{rec}(p_T, \mid \eta^{rec} \mid < 2.4, \mid \eta^{gen} \mid > 2.4)$ is the number of J/ψ events in the Monte Carlo sample, which are generated $\mid \eta^{gen} \mid > 2.4$ and reconstructed $(\mid \eta^{rec} \mid < 2.4)$, and $N^{gen}(p_T, \mid \eta^{gen} \mid > 2.4)$ is the total number of events generated with $\mid \eta^{gen} \mid > 2.4$. In this analysis the relative acceptance A' is about 0.01%.

7.1.2 Determination of the correction factors to the efficiencies using tag and probe method

The total reconstruction efficiency A as defined in Eq. (7.2) is computed using the Monte Carlo simulation. Any deviation to the total efficiency that could arise in real data taking can be determined on data itself, using the "tag and probe" methods. Ref. [92] has outlined how to determine these deviations. As previously mentioned at the beginning of Section 5, there will be both corrections to trigger efficiencies as well as to the offline efficiencies.

The subsequent sections will sketch how the method could be applied. The details of the method as well as the results will be part of a separate note, which is being written with the CSA08 exercise of the dimuon group within the Muon POG (Physics Object Groups) [93].

7.1.2.1 Reconstruction efficiency correction

Given the low momenta of the two muons, we will investigate the reconstruction efficiency measurement in the data using known resonances, such as J/ψ , ψ' and Υ (hereafter referred as Onia), whose decayed muons can be triggered by single muons with suitable low p_T threshold. One candidate data stream for this is the SingleMuPT3 or SingleMuPT7, where the muon is reconstructed offline using a GlobalMuon reconstruction. Onia candidates are then reconstructed by pairing the offline reconstructed GlobalMuon (that will be used for the *tag*) with an opposite charge muon that will serve as the *probe*. Tight selection criteria in the mass of the resonance should be used in order to limit the level of the background.

We will follow the prescriptions given in Section 7.1 of Ref. [92]. Preliminary studies for the J/ψ could be found in Ref. [94]. Assuming that the offline reconstruction efficiency can be expressed as the product of the individual muons efficiencies:

$$\epsilon^{J/\psi}_{offline}(p_T^{J/\psi}, \eta_{J/\psi}, \theta_{J/\psi}) = \epsilon_{\mu_1}(p_T^{\mu_1}, \eta_{\mu_1}) \times \epsilon_{\mu_2}(p_T^{\mu_2}, \eta_{\mu_2}), \tag{7.5}$$

both in the data and in the Monte Carlo simulated samples. The correction factors to efficiencies is the ratio between real data and Monte Carlo simulation efficiencies:

$$\lambda^{corr}_{reco}(p_T^{\mu}, \eta^{\mu}) = \frac{\epsilon^{\mu}_{data}(p_T^{\mu}, \eta^{\mu})}{\epsilon^{\mu}_{MC}(p_T^{\mu}, \eta^{\mu})} \tag{7.6}$$

Ideally, $\lambda_{reco}^{corr}(p_T^{\mu}, \eta_{\mu})$ should be one, if the Monte Carlo simulation used is perfect.

7.1.2.2 Trigger efficiency correction

In a similar way, the trigger efficiency correction can be determined. We will use opposite sign GlobalMuons compatible to come from the decay of an quarkonia in single muon triggered event skims. The muon that triggered the event is used as a tag and another muon is used to probe the trigger efficiency path for that muon. This method is able to measure the trigger efficiency of the single muon path from L1 down to L3 muons, but it must be noted that the trigger efficiency is defined as the efficiency of the trigger path over the *offline* reconstructed J/ψ. The J/ψ trigger efficiency, as computed with this method, is therefore measuring the probability of a reconstructed J/ψ event to fire the J/ψ trigger:

$$\epsilon_{trig}(p_T^{J/\psi}, \eta_{J/\psi}) = \frac{N_{trig}(p_T^{J/\psi}, \eta_{J/\psi})}{N_{offlinereco}(p_T^{J/\psi}, \eta_{J/\psi})} \tag{7.7}$$

The efficiency (normalized to the offline reconstructed J/ψ) as function of $p_T^{J/\psi}$ and $\eta_{J/\psi}$ is shown in Figs. 7.2 and 7.3 respectively.

The J/ψ trigger efficiency can therefore be expressed as:

$$\epsilon_{trigger}^{J/\psi} = \epsilon_{trigger}^{\mu_1} \cdot \epsilon_{trigger}^{\mu_2} \cdot \zeta(\mu_1, \mu_2) \tag{7.8}$$

where $\epsilon_{trigger}^{\mu_i}$ is the single muon trigger efficiency path for muon i and $\zeta(\mu_1, \mu_2)$ an ad-hoc factor that can be computed in the Monte Carlo to take into account for remaining correlation effects. It should be noted that, due to the requirement of the two GlobalMuons coming from the Onia, the correlation induced by this selection is largely taken into account in the determination of $\epsilon_{trigger}^{\mu_i}$, and it is therefore valid to assume that $\zeta(\mu_1, \mu_2)$=1. Thus measuring the J/ψ trigger efficiency is reduced to measuring the single muon trigger efficiencies.

The total trigger efficiency is a combination of L1, L2 and L3 muon trigger efficiencies. It can be expressed as the product of the conditional probabilities:

$$\begin{aligned}\epsilon^{\mu}_{trigger} =&\epsilon^{\mu}_{L1} \cdot \epsilon^{\mu}_{L2} \cdot \epsilon^{\mu}_{L3} \\ =&\mathrm{P(L1, offline|offline)} \cdot \mathrm{P(L1, L2, offline|L1, offline)} \\ &\cdot \mathrm{P(L1, L2, L3, offline|L1, L2, offline)}\end{aligned} \tag{7.9}$$

Each single probability can be determined with the tag and probe method. First, unbiased events will be collected by a high p_T single muon trigger and with at least two offline reconstructed muons with $p_T > 3$ GeV/c and invariant mass compatible to come from a Onia. Then we will determine $\mathrm{P(L1, offline|offline)}$: the fraction of unbiased events that pass the L1 di-muon trigger, given that both muons have been reconstructed offline, or in other words the L1 trigger efficiency for a single muon. The second probability term, $\mathrm{P(L1, L2, offline|L1, offline)}$,is the fraction of events unbiased relative to L2 that pass the L2 trigger, given that the muons passed the L1 di-muon trigger and have been reconstructed offline; this probability is therefore measuring the L2 trigger efficiency for single muon. Finally, the third probability term, $\mathrm{P(L1, L2, L3, offline|L1, L2, offline)}$, is the fraction of events unbiased relative to L3 that pass the L3 trigger, given that the muons passed the L1 and L2 di-muon trigger and have been reconstructed offline.

The correction factors to the trigger efficiency is the ratio between the efficiency found in data and that of the Monte Carlo simulation:

$$\lambda^{corr}_{trigger}(p^{\mu}_T, \eta^{\mu}) = \frac{\epsilon^{data}_{trigger}(p^{\mu}_T, \eta^{\mu})}{\epsilon^{MC}_{trigger}(p^{\mu}_T, \eta^{\mu})} \tag{7.10}$$

7.2 Measurement of fraction of J/ψ from B-decay

From a theory point of view a measurement of the prompt J/ψ production cross section is highly interesting. Hence the $J/\psi's$ from B-hadron decays should be separated from the prompt components. This separation can be done by fitting the pseudo-proper decay length distribution of J/ψ.

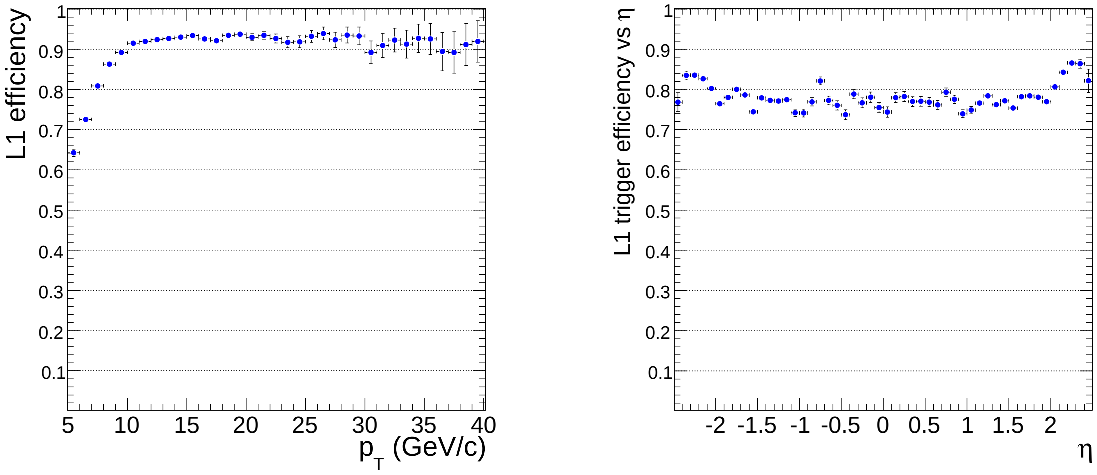

Figure 7.2: The J/ψ L1 trigger efficiencies as a function of $p_T^{J/\psi}$ (left) and $\eta_{J/\psi}$ (right).

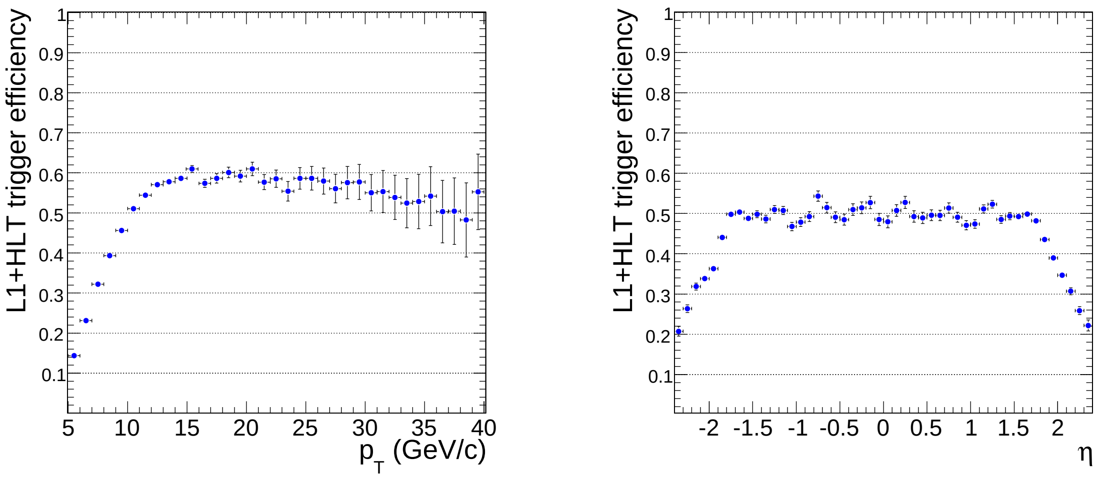

Figure 7.3: The J/ψ L1+HLT trigger efficiencies as a function of $p_T^{J/\psi}$ (left) and $\eta_{J/\psi}$ (right).

7.2.1 Pseudo-proper decay length distribution

Prompt charmonia decay immediately after being produced. In contrast, B-hadrons have long lifetimes in the order of pico seconds, because the decay of a B-hadron to a J/ψ is mediated by the weak interaction $b \to cW$. This implies that J/ψ events from the decays of B-hadrons are likely to be displaced from the primary vertex. In order to separate the prompt and non-prompt components, an excellent performance of secondary vertex reconstruction is required. The pseudo-proper decay length is defined as:

$$\ell_{xy}^{J/\psi} \equiv \frac{L_{xy}^{J/\psi} \cdot M_{J/\psi}}{p_T^{J/\psi}}, \tag{7.11}$$

where $L_{xy}^{J/\psi}$ is the component of the proper decay length (defined as the distance between the vertex of the two muons from J/ψ decays and the primary vertex of the event) on J/ψ's transverse momentum direction and $M_{J/\psi}$ the mass of the J/ψ. The $\ell_{xy}^{J/\psi}$ distribution of prompt and non-prompt J/ψ's is shown in Fig. 7.4. The component due to the prompt fraction is describing the intrinsic resolution function due to the finite performance of the tracking reconstruction. The long exponential behaviour, visible at large $\ell_{xy}^{J/\psi}$ clearly shows the B hadron component. It should be noticed that negative values of the $\ell_{xy}^{J/\psi}$ come from resolution effects, where the vectors of the J/ψ momentum and the one joining the primary and secondary vertices in the transverse plane are in opposite directions and is in fact occurring at small decay lengths.

While at Monte Carlo truth level the pseudo-proper decay length for prompt J/ψ's is equal to zero, for reconstructed J/ψ's, the distribution is described by a resolution function, as will be explained below (see Eq. (7.19)).

The pseudo-proper decay length for non-prompt J/ψ's has a more complicated shape. It must be noted that the *pseudo proper decay length* defined in Eq. (7.11) is different from the *proper decay length* defined as:

$$\ell_{xy}^{B} = \frac{L_{xy}^{B} \cdot M_{B}}{p_T^{B}} \tag{7.12}$$

where M_B and p_T^B are the mass and transverse momentum of the B-meson. The ℓ_{xy}^B distribution of B-hadrons has an exponential behaviour. However, the distribution of $\ell_{xy}^{J/\psi}$ of J/ψ's from B-hadrons is not perfectly exponential, since the transverse momentum of the J/ψ does not coincide with the transverse momentum of the B hadron. To estimate the shape at Monte Carlo truth level, we notice that the

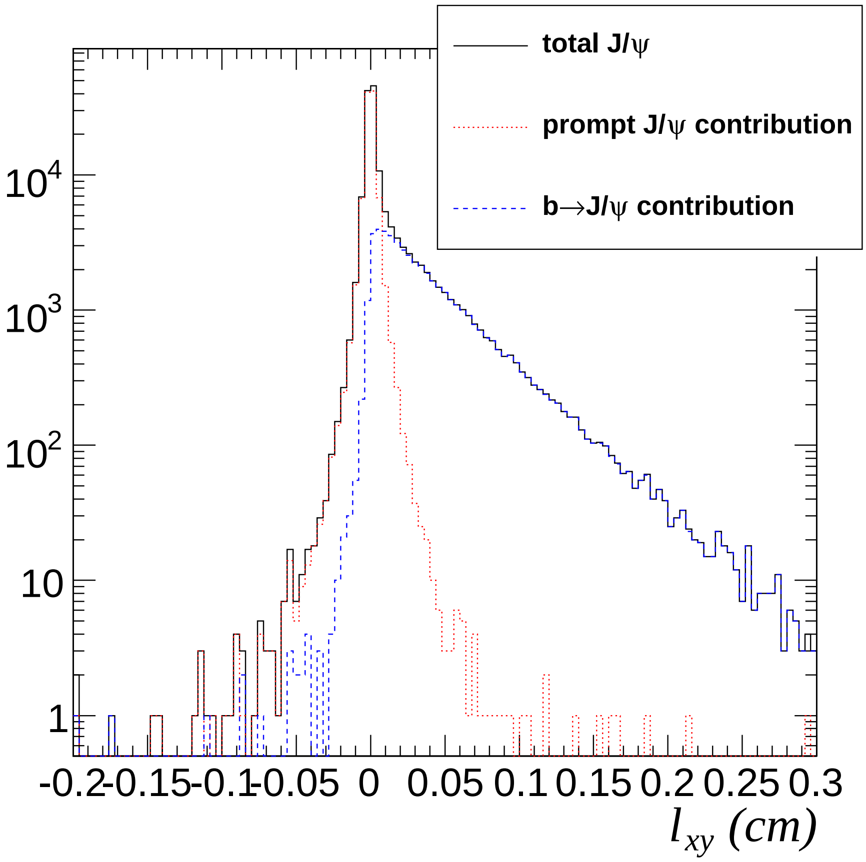

Figure 7.4: The ℓ_{xy} distributions for prompt (dotted), B-decay (dashed) and total J/ψ (solid) events.

relation between the pseudo-proper and the proper decay length is given by

$$\frac{\ell_{xy}^{J/\psi}}{\ell_{xy}^{B}} = \frac{\frac{M_{J/\psi}}{p_T^{J/\psi}}}{\frac{M_B}{p_T^B}}, \tag{7.13}$$

which is described by a Gaussian function

$$G_{mc}(\ell_{xy}, \mu_{mc}, \sigma_{mc}) \tag{7.14}$$

with sigma σ_{mc} and mean μ_{mc}.

Hence, the function that approximates the $\ell^{J/\psi}$ distribution for the B-hadron component at Monte Carlo truth level will be:

$$X_{mc}(\ell_{xy}) = Exp(-\ell_{xy}/\ell_{xy_0}) \otimes G_{mc}(\ell_{xy}, 0, \sigma_{mc}) \tag{7.15}$$

where $Exp(-\ell_{xy}/\ell_{xy_0})$ describes the exponent part, and G_{mc} the correction as explained in Eq. (7.14).

To describe the ℓ_{xy} distribution for non-prompt J/ψ events at reconstruction level, Eq. (7.15) must be convoluted with the same resolution function as that for prompt J/ψ's, which will be described in Eq. (7.19).

7.2.2 Likelihood function

To determine the B-fraction we follow the procedure as described in Ref. [23]. We perform an unbinned maximum likelihood fit on the data to extract the fraction f_B, i.e. the fraction of J/ψ's which come from B-hadron decays. The mass and ℓ_{xy} of each event is simultaneously fitted by a log-likelihood function L which is defined as:

$$\ln L = \sum_{i=1}^{N} \ln F(\ell_{xy}, m_{\mu\mu}), \tag{7.16}$$

where N is the total number of events in the mass window of signal, ℓ_{xy} the pseudo proper decay length, and $m_{\mu\mu}$ the reconstructed dimuon mass.

The distribution of mass and pseudo-proper decay time is described by:

$$F(\ell_{xy}, m_{\mu\mu}) = f_{Sig} \times F_{Sig}(\ell_{xy}) \times M_{Sig}(m_{\mu\mu}) + (1 - f_{Sig}) \times F_{Bkg}(\ell_{xy}) \times M_{Bkg}(m_{\mu\mu}), \tag{7.17}$$

where:

- f_{Sig} is the fraction of signal J/ψ events (i.e. both prompt and non-prompt) in the mass region,
- $F_{Sig}(\ell_{xy})$ and $F_{Bkg}(\ell_{xy})$ are the functional forms describing the J/ψ pseudo-proper decay length distribution for the signal and background respectively,
- $M_{Sig}(m_{\mu\mu})$ and $M_{Bkg}(m_{\mu\mu})$ are the functional forms describing the invariant mass distributions for the signal and background respectively.

The signal ℓ_{xy} distribution of the J/ψ's, $F_{Sig}(\ell_{xy})$, is expressed as:

$$F_{Sig}(\ell_{xy}) = f_B \times F_B(\ell_{xy}) + (1 - f_B) \times F_p(\ell_{xy}), \tag{7.18}$$

where f_B is the fraction of J/ψ from B-hadron decays, and $F_B(\ell_{xy})$ and $F_p(\ell_{xy})$ are the pseudo-proper decay length distributions for non-prompt and prompt J/ψ's respectively. Starting with the prompt component of Eq. (7.18), we remind that prompt J/ψ's are produced at the primary vertex, therefore their observed displacement is described by a resolution function

$$F_p(\ell_{xy}) = R(\ell_{xy}) \tag{7.19}$$

Ref. [23] found that $R(\ell_{xy})$ is best described by a sum of a wide and a narrow Gaussian convoluted plus a double-sided exponential functions, the latter in order to describe the (small) tails:

$$R(\ell_{xy}) = G_n(\ell_{xy}, \mu_n, \sigma_n) \oplus G_w(\ell_{xy}, \mu_w, \sigma_w) \oplus Exp(-|\ell_{xy}|/\lambda) \tag{7.20}$$

Concerning the non-prompt component of Eq. (7.18), the shape of $F_B(\ell_{xy})$ is given by a product of two separate parts

$$F_B(\ell_{xy}) = R(\ell_{xy} - \ell'_{xy}) \otimes X_{mc}(\ell'_{xy}), \tag{7.21}$$

where R is again the resolution function of ℓ_{xy} (see Eq. (7.20)), and $X_{mc}(\ell_{xy})$ the ℓ_{xy} distribution of the J/ψ's from B-decay, which was given in Eq. (7.15).

With regard to the background going in Eq. (7.17), this has a more complicated function because the sideband events. Part of the background is from the long lived B-hadrons that produce muons with opposite sign such as $B \to c\mu^-\bar{\nu}X$ and $c \to \mu^+\nu X$. The expression for F_{Bkg} [23] is as follows:

$$F_{Bkg}(\ell_{xy}) = \begin{cases} (1 - f_+ - f_- - f_{sym}) \cdot R(\ell_{xy}, \sigma) + \frac{f_+}{\lambda_+} e^{-\frac{\ell'_{xy}}{\lambda_+}} \otimes R(\ell'_{xy} - \ell_{xy}, \sigma) \\ \quad + \frac{f_{sym}}{2\lambda_{sym}} e^{-\frac{\ell'_{xy}}{\lambda_{sym}}} \otimes R(\ell'_{xy} - \ell_{xy}, \sigma) & \text{when } \ell_{xy} > 0, \\ (1 - f_+ - f_- - f_{sym}) \cdot R(\ell_{xy}, \sigma) + \frac{f_-}{\lambda_-} e^{\frac{\ell'_{xy}}{\lambda_-}} \otimes R(\ell'_{xy} - \ell_{xy}, \sigma) \\ \quad + \frac{f_{sym}}{2\lambda_{sym}} e^{\frac{\ell'_{xy}}{\lambda_{sym}}} \otimes R(\ell'_{xy} - \ell_{xy}, \sigma) & \text{when } \ell_{xy} < 0, \end{cases} \tag{7.22}$$

where $f_{\pm,sym}$ is the fraction of the background distribution in the positive, negative and symmetric exponential tails respectively, and where $\lambda_{\pm,sym}$ are corresponding exponential slopes.

The mass distribution used in the likelihood expression in Eq. (7.17) is a double Gaussian for signal, and a linear function for background:

$$M_{Sig}(m_{\mu\mu}) = (1 - f_2) \cdot G_1(m_{\mu\mu}, \mu_M, \sigma_M) + f_2 \cdot G_2(m_{\mu\mu}, \mu_{M+D}, \gamma_2\sigma_M) \tag{7.23}$$

$$M_{Bkg}(m_{\mu\mu}) = \frac{1}{m_{\mu\mu}^{max} - m_{\mu\mu}^{min}} + M_{slope}(m_{\mu\mu} - \frac{m_{\mu\mu}^{max} + m^{min}}{2}) \tag{7.24}$$

Here μ_M is the mean of the mass distribution, σ_M the width of the first Gaussian distribution, f_2 the fraction of the second Gaussian distribution at the given $m_{\mu\mu}$, and γ_2 the ratio of the widths of the two Gaussian distributions. Further $m_{\mu\mu}^{max}$ and $m_{\mu\mu}^{min}$ are the mass range and M_{slope} is the slope of the mass background distribution, and D is the difference between the widths of the two Gaussian.

7.2.3 Fitting procedure

The prompt, non-prompt J/ψ and background samples are mixed together with a weight, according to their cross sections and statistics. The unbinned maximum likelihood was performed in 15 $p_T^{J/\psi}$-bins from 5 to 40 GeV/c, requiring each p_T bin to contain at least 2000 Monte Carlo events. Fig. 7.5 shows the fraction of J/ψ's from B-hadron decay as resulting from the fit as compared to that at Monte Carlo truth level. A good agreement is seen. In Appendix B we show the results of the fit for each $p_T^{J/\psi}$ bin. One example of the fitting result in the $p_T^{J/\psi}$ bin of 9 GeV/c $< p_T^{J/\psi} <$ 10 GeV/c can be seen in Fig. 7.6.

the B fraction rises from $\sim 15\%$ at low p_T to $\sim 50\%$ at high p_T.

7.2.4 Validation of the B fraction fitting

The fitting method in the previous section is called the standard fit. Several checks are applied to ensure that the fits do indeed describe the data. To test if the

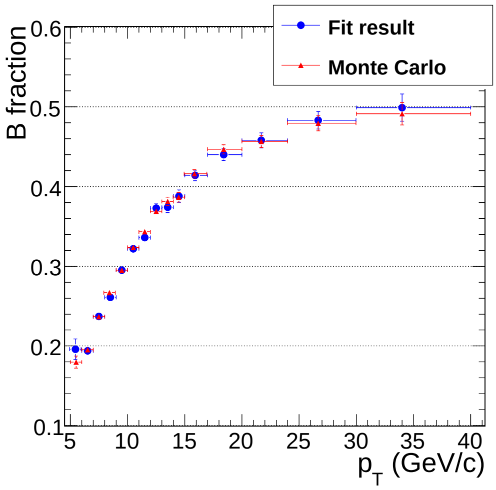

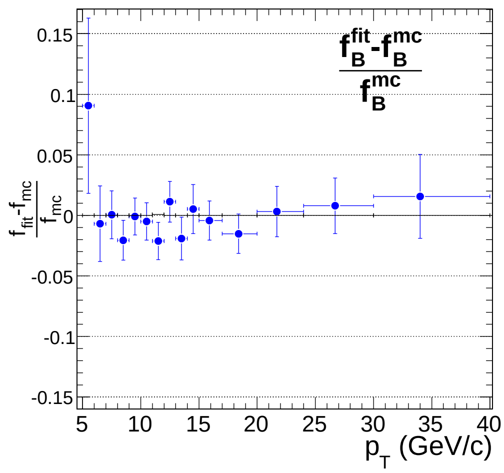

Figure 7.5: Left: the B fraction from fitting (dot) and the MC truth (triangle). Right: the deviation of the fitted B fraction from MC truth. The unbinned maximize likelihood fitting provides the correct results, within the range of three σ.

fits are stable under variations in the fitting technique the fits are redone with the following variations:

- The vertex resolution is changed to a triple Gaussian resolution function.
- A simple exponential function is used to describe the ℓ_{xy} distribution of B-decay J/ψ.
- The background level is doubled.

Fig. 7.7 shows the result with statistic uncertainties of the new fits divided by the results of the standard fitting method. In all cases, the variations are small compared to the statistical uncertainties. The deviations are considered as the systematic uncertainties introduced in the B fraction fit (see the systematics Section).

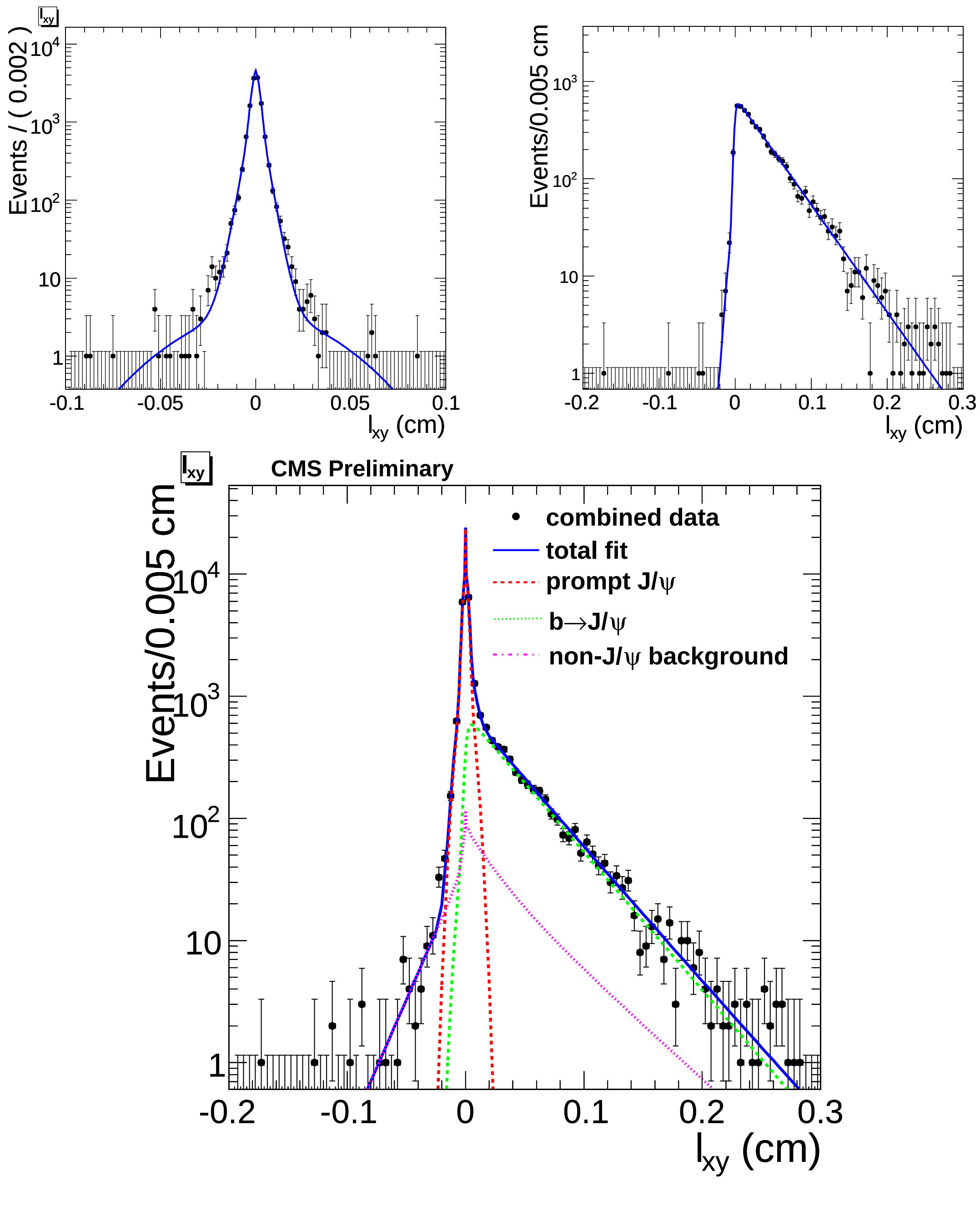

Figure 7.6: Fits to the ℓ_{xy} distributions in the range of 9 GeV/c $< p_T <$ 10 GeV/c for prompt (top left) , B-decay (top right) and combined (bottom center) J/ψ events.

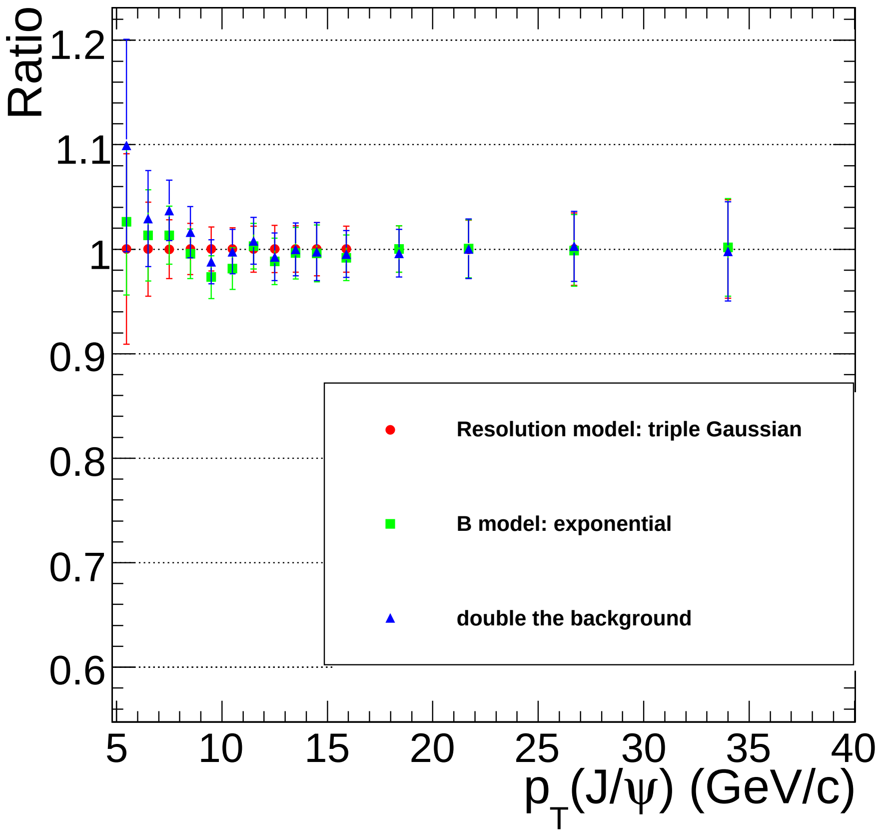

Figure 7.7: Variation in the J/ψ B fraction as a function of $p_T^{J/\psi}$ for the different fitting methods: $f_{new}/f_{standard}$.

Chapter 8

Misalignment effects in early data

A precision alignment of the CMS tracking and muon detectors is one of the most challenging offline calibration tasks CMS faces. A detailed description of the general alignment concepts and the procedures involved for the muon and Tracker are presented in [63]. This section gives an overview of alignment strategy and simulation. After that, the misalignment effects in the J/ψ analysis are discussed.

8.1 Alignment strategy

The tracker alignment has to be performed in 3 steps:

- During the ongoing assembly of the CMS Tracker, positions and orientations of the Tracker components (silicon sensors as well as support structures) are being measured and stored in databases with the help of, e.g., coordinate-measurement machines or photogrammetry.

- After assembly, the Laser Alignment System (LAS) [63] will provide the positions of the Tracker sub-detectors TIB, TOB, and TEC (not including the pixel detector and the TID) with respect to each other with a precision of about 100 μm.

- The initial track-based alignment has two scenarios: the first step will be its precise internal and external alignment, so that it can then define the reference system for the subsequent alignment of the strip tracker. The pixel alignment will be performed using tracks that have been reconstructed using pixel hits only (and a vertex constraint) to avoid bias originating from the not yet aligned strip tracker. In the second step, strip tracker alignment will be carried out using the pixel detector as a reference.

Once the Tracker is aligned, it will define the reference system relative to which the positions of the calorimeter modules and muon detectors will be adjusted. In particular, for the optimal reconstruction of muon tracks, it is important to combine information from the Tracker and the muon detectors. In order to study the impact of both Muon and Tracker misalignment on the reconstruction of muon tracks, the tools described in the follow section are used to simulate a realistic environment that includes the expected alignment uncertainties for the individual tracking devices.

8.2 Simulation of misalignment

The displacement of detector modules is implemented after detector simulation at the reconstruction level using a dedicated software tool, which is able to move and rotate all Tracker parts (individual modules as well as rods, layers, half-barrels, etc.). Hits on Tracker sensors are generated according to the ideal detector geometry, and the geometrical shift and rotation of the sensor are introduced afterward. Within the quoted uncertainties, the misalignments are applied using a flat distribution for mechanical constraints, whereas a Gaussian distribution is used for laser and track-based alignment results. To achieve a reasonable χ^2 distribution in the track fit, the hit position error is increased by adding an additional error, so called Alignment Position Error (APE), in quadrature that reflects the size of the assumed misalignment.

8.3 Misalignment effects in early data

In order to study any possible bias and degradations in disentangling the prompt and non-prompt components, we have investigated the effects of misalignment by re-reconstructing the same samples, made with ideal alignment conditions, in the 10 and 100 pb^{-1} misalignment scenarios [63]. Differences as a result of misalignment will be taken into account in the systematic uncertainties. The effect of misalignment has been investigated for the following quantities:

- The reconstruction efficiency. Fig. 8.1 shows $\epsilon^{filt}_{J/\psi}$ (see Eq. (6.5)) as function of $p_T^{J/\psi}$. The reconstruction efficiency is not affected by misalignment. In fact, the alignment position error is added to the intrinsic hit measurement error (in quadrature) to take into account the residual uncertainty in the alignment parameters. This guarantees that no hits are lost during the pattern recognition even in worse misalignment scenarios.

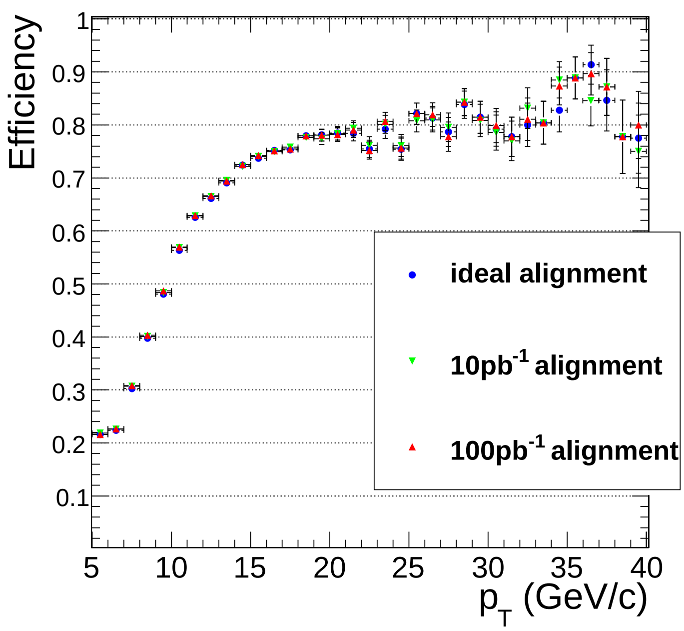

Figure 8.1: J/ψ reconstruction efficiency vs. $p_T^{J/\psi}$.

- J/ψ mass resolution. This is affected as a consequence of a worse tracking resolution performance. Fig. 8.2 shows the J/ψ invariant mass distribution in 10 pb^{-1} and 100 pb^{-1} misalignment scenarios, and Tab. 8.1 shows the mass resolution by fitting the mass peaks with a single Gaussian function.

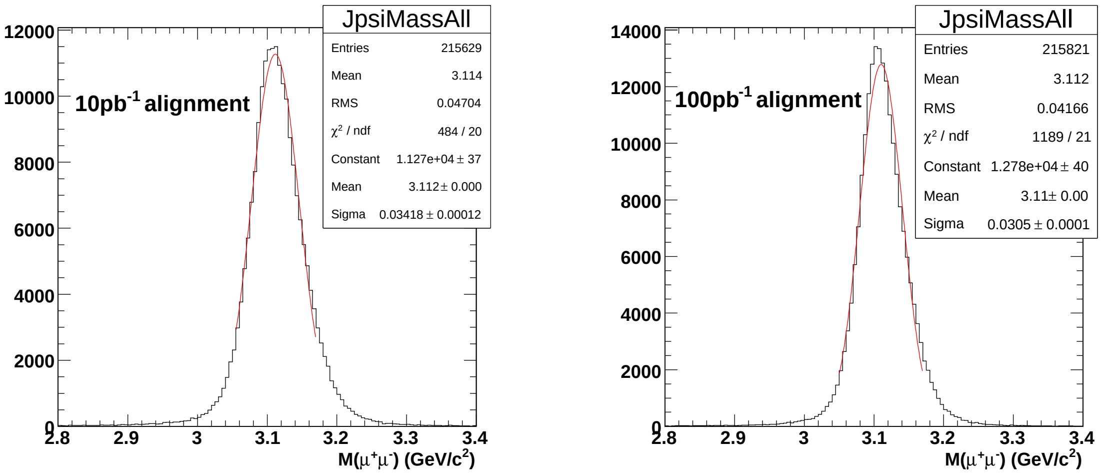

Figure 8.2: J/ψ invariant mass distribution in 10 pb^{-1}(left) and 100 pb^{-1} (right).

	10 pb^{-1}	100 pb^{-1}	ideal
J/ψ mass resolution (MeV)	34.2	30.5	29.5

Table 8.1: J/ψ mass resolution in different misalignment scenarios

The dimuon mass resolution turns out to depend linearly on the muon momentum resolution and thus on the degree of misalignment. Thus, in a short-term misalignment scenario, the worse muon momentum resolution will result in a wider J/ψ mass peak.

- Distribution of $\ell_{xy}^{J/\psi}$. The vertex resolution being worse in a short term scenario, we expect the $\ell_{xy}^{J/\psi}$ distribution to be affected. Fig. 8.3 shows the pseudo-proper decay length distributions of both prompt and B-decay J/ψ in an ideal and a 10 pb^{-1} scenario. The influence on the B fraction resulting from the fit has been investigated by comparing the ideal alignment scenario with that expected at 10 pb^{-1}. Fig. 8.4 displays the comparison between the two different misalignment scenarios with the input from Monte Carlo.

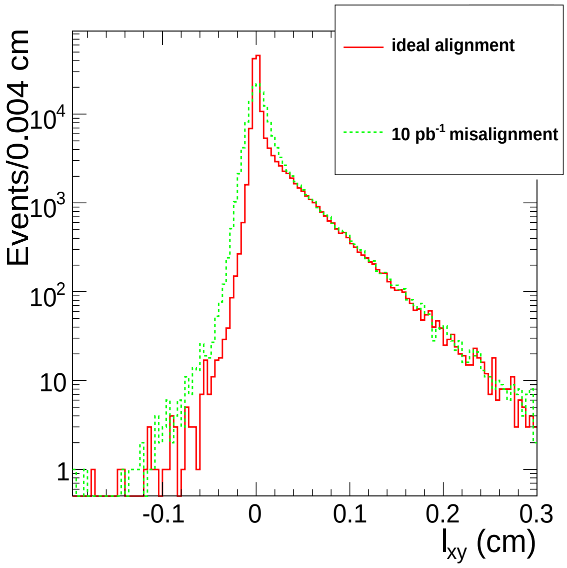

Figure 8.3: J/ψ pseudo-proper decay length distribution in different misalignment scenarios.

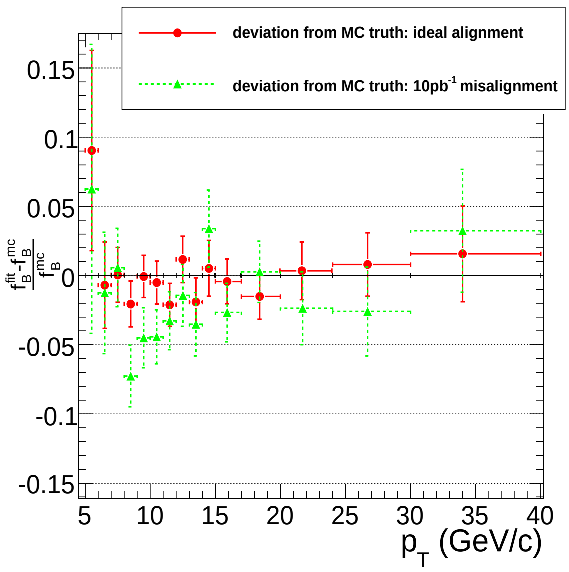

Figure 8.4: The relative deviation of the measured B fraction with respect to the Monte Carlo truth for an ideal misalignment scenario (dots) and a 10 pb^{-1} misalignment scenario (triangles).

Chapter 9

Systematics uncertainties

In this section an estimate of possible systematic uncertainties is given. It must be noticed that some of the systematics will certainly come from the study of other groups (such as the one from the luminosity or alignment). Others may arise when real data taking will start, for example the corrections to the trigger and offline reconstruction efficiencies as explained in Section 7.1.2.

The following systematic uncertainties have been considered:

- Luminosity determination. The LHC experiment TOTEM [58] will be able to measure the luminosity with an uncertainty of the order of 5% or less already at the LHC start [95]. As a comparison, in the J/ψ measurement of CDF II [23], that uncertainty was about 5.9% for an integrated luminosity of 39.7 pb^{-1}. In this analysis, 10% was considered as a feasible target.

- Finite Monte Carlo statistics. As a Monte Carlo simulation was used to determine the total efficiencies in this analysis, it will introduce a systematic uncertainty related with the statistics of simulated events affecting the total efficiency. The uncertainty is dependent on the $p_T^{J/\psi}$ bin, and the effect on the cross section is given in Tab. 11.1 in Appendix C.

- J/ψ polarization uncertainty. Kinematic acceptance as a function of $p_T^{J/\psi}$

depends upon the J/ψ polarization, as shown in Fig. **??**. It is our plan to make a measurement of the polarization with collision data at CMS and then can be used to determine the J/ψ total efficiency value and uncertainty. In absence of it at this moment, an estimation was made from the measurements of CDF for prompt J/ψ [32] and of BaBar for non-prompt J/ψ [96]. The mean of α measured in different $p_T^{J/\psi}$ bins is used to determine the central value of the total efficiency, while the systematic uncertainty is taken by varying α by three standard deviations around the measured value. It's found the uncertainty is 2.4% near $p_T^{J/\psi}$=6 GeV/c and 6.0% in the region $p_T^{J/\psi}$>20 GeV/c. The effect on the cross section is displayed in Table 11.2 in Appendix C for each $p_T^{J/\psi}$ bin.

- Binning in $p_T^{J/\psi}$. The choice of the binning in $p_T^{J/\psi}$ affects the total efficiency A in each $p_T^{J/\psi}$ bin. A large binning was chosen to allow for enough background statistics in the lifetime fit. In order to evaluate the effect of the chosen binning in $p_T^{J/\psi}$ on the total efficiency, each $p_T^{J/\psi}$ bin was splitted into four smaller bins in equal $p_T^{J/\psi}$ size and re-calculate the total efficiencies in the sub-bins. The average value for the total efficiencies in the four sub-bins has a small difference with the one of the whole $p_T^{J/\psi}$ bin, as defined in Eq. (9.1). The value ΔA/A was considered as a systematic uncertainty from the binning in $p_T^{J/\psi}$, where

$$\Delta A = \frac{1}{4}\sum_{i=1}^{4} A_i - \frac{\sum_{i=1}^{4} A_i N_i}{\sum_{i=1}^{4} N_i} \tag{9.1}$$

The result for each $p_T^{J/\psi}$ bin is given in Table 11.3 in Appendix C.

- Muon momentum scale. The mass of the dimuon system depends linearly on the momentum scale of the two muons. The number of events will be determined from a fit to the dimuon invariant mass distribution. This means that a difference in the muon p_T cut between data and Monte Carlo will affect the number of events that will pass the HLT trigger, and also the number of events in a given bin of $p_T^{J/\psi}$. Thus, an uncertainty in the muon momentum scale affects the total efficiency for each bin of $p_T^{J/\psi}$. This uncertainty has been evaluated and found to be at most 1%.

- Parametrization of the invariant mass fitting function. As shown in Section 6.2.2 a double Gaussian function is found to describe quite accurately the dimuon invariant mass in each $p_T^{J/\psi}$ bin. In order to investigate any dependence on $\eta_{J/\psi}$ in the $p_T^{J/\psi}$ bin, the J/ψ candidates in each bin were splitted into three separate $|\eta_{J/\psi}|$ regions with the following boundaries: $(0.-0.8-1.6-2.4)$. In each of those regions the dimuon invariant mass is fitted with a single Gaussian and the difference with respect to a single $\eta_{J/\psi}$ bin and double Gaussian is taken as systematics. As can be seen from Table 11.4 in Appendix C, the differences are of the order of 2%, except for the two largest $p_T^{J/\psi}$ bins, where the statistical fluctuations are anyhow large.

- The corrections to the total efficiency as measured by the tag and probe technique. No final results are available for the analysis yet. Extrapolating the result from CDF [23], where about 3 times more J/ψ's were reconstructed and an error of about 3% was quoted, we have taken a 5% uncertainty.

- Residual misalignment effect. In Sec. 8.3 the effect of misalignment was investigated on the different ingredients in the analysis. Misalignment affects the ℓ_{xy} distributions, and as such could affect the fitted B-fraction. In order to test any bias in the fitting procedure of B-hadron fraction, the unbinned maximum likelihood fit was repeated in in two scenarios (i.e. perfectly aligned and 10 pb^{-1} misalignment). The results of fit comparing with the input from the Monte Carlo is shown in Fig. 8.4. There was no bias observed in the fraction of J/ψ's from B-hadron decay. A conservative 50% of the difference between the results of the two scenarios is taken as a systematics. The result for all $p_T^{J/\psi}$ bins is given in Table 11.7 in Appendix C.

- Resolution model. The ℓ_{xy} resolution function for the prompt J/ψ has been parameterized as a double Gaussian plus a double-sided exponential. We have compared a triple gaussian resolution function and taken the differences as a systematic error. The graphs of the unbinned maximum likelihood fit using a triple Gaussian resolution function are displayed in Appendix D for all $p_T^{J/\psi}$ bins. The systematic errors for all $p_T^{J/\psi}$ bins is given in Table 11.5 in Appendix C.

- B-hadron lifetime model. The B hadron pseudo-proper time is described by a convolution of an exponential decay with a Gaussian function describing the fragmentation effect of the difference between the transverse momentum of the J/ψ and that of the B-hadron, from which J/ψ originates. The Gaussian function was removed to have a conservative estimate of the model used to describe the B-hadron lifetime distribution and a negligible difference was found. The result is given in Table 11.6 in Appendix C.

- Background uncertainty. Both the background level and its ℓ_{xy} parametrization influence the fit to the B-hadron fraction. The sample used to determine the QCD background gives only about 500 events in the invariant mass window between 2.8 and 3.4 GeV/c^2, out of 20 million generated. Those need to be split into 15 $p_T^{J/\psi}$ bins, clearly giving very small statistics to get any assumption on their mass distribution as well as their pseudo proper decay length distribution. It would need much more QCD background to study any effects due to this source properly. All the 500 events were used for each $p_T^{J/\psi}$ bin, and scaled to the appropriate background level as expected. As said in Section 4.2.3, the double fake muons background is missing. The average effect of such background is estimated to be at most of the same order of magnitude in the first $p_T^{J/\psi}$ bin and decreasing very rapidly for higher $p_T^{J/\psi}$. We fitted the B-hadron fraction in each $p_T^{J/\psi}$ bin and varied the background level by 50%, on average. We also compared the results of the fit in the extreme case where no background is taken and found similar variations. The result is displayed in Table 11.8 in Appendix C.

A summary of all systematic sources and numbers are given in Tab. 9.1.

Parameter affected	Source	$\Delta\sigma/\sigma$
Luminosity	Luminosity	$\sim$ 10 %
Number of J/ψ	J/ψ mass fit	1.0 - 6.3 %
Number of J/ψ	Momentum scale	$\sim$ 1 %
Total efficiency	J/ψ polarization	1.8 - 7.0%
Total efficiency	$p_T^{J/\psi}$ binning	0.1 - 10 %
Total efficiency	MC statistics	0.53 - 1.7 %
$\lambda_{reconstruction}$	Non-perfect detector simulation	$\sim$ 5 %
$\lambda_{trigger}$	Non-perfect detector simulation	$\sim$ 5 %
B fraction	ℓ_{xy} resolution model	0 - 1.9 %
B fraction	B-hadron lifetime model	0.01 - 0.05 %
B fraction	Background	0.1 - 3.0 %
B fraction	Misalignment	0.7 - 3.5 %
Total systematics 13 % - 19 %		

Table 9.1: Summary of possible systematic uncertainties in the J/ψ cross section measurement in CMS early data. All the uncertainties are $p_T^{J/\psi}$-dependent, except for the uncertainty from luminosity. The total uncertainty is about 13% in the region $p_T^{J/\psi}$ >20 GeV/c and 19 % at the lowest $p_T^{J/\psi}$ bin 5-6 GeV/c.

Chapter 10

Results and prospects

Tab. 10.1 displays for each bin of $p_T^{J/\psi}$ the number of fitted J/ψ's, the total efficiency, the fitted B-fraction, and the systematic uncertainty. Tab 10.2 displays the values of the J/ψ differential cross section with systematic and statistical uncertainties. Figs. 10.1 and 10.2 display the inclusive (left) and prompt (right) J/ψ differential cross sections respectively, with combined systematic and statistical uncertainties, corresponding to an integrated luminosity of $3\,\mathrm{pb}^{-1}$. Fig. 10.3 shows the result of the fits to the fraction of J/ψ's from B-hadron decay in each bin of $p_T^{J/\psi}$.

The measurement of the differential J/ψ cross section is shown to be feasible already for an integrated luminosity of 3 pb^{-1}. The low level of background and the excellent performance of the reconstruction, permit to test the inclusive $p_T^{J/\psi}$ differential $J/\psi \to \mu^+\mu^-$ production cross section, and determine the fraction of J/ψ produced by B-hadron decays, in the full range of $p_T^{J/\psi}$ between 5 and 40 GeV/c. The precision of the result is limited by systematic uncertainties, and is around at the 15 % level. The accuracy for this integrated luminosity is slightly worse than the CDF one in the $p_T^{J/\psi}$ range common to both measurements, but is probing for the first time the spectrum beyond 20 GeV/c. Some of the systematics will, of course, benefit from the larger data set that will be collected with higher integrated luminosities. The uncertainties in the background level will be checked in data directly,

$p_T^{J/\psi}$ bin GeV/c	Yield N_{sig}	Total efficiency A_i	B fraction f_B	Systematic %
5-6	2591±52	0.00319±0.00006	0.196±0.013	19
6-7	11098±109	0.0228±0.0002	0.194±0.0061	14
7-8	17565±137	0.0599±0.0004	0.237±0.0047	14
8-9	20007±147	0.111±0.0006	0.261±0.0044	14
9-10	18856±141	0.163±0.0009	0.295±0.0045	14
10-11	16601±132	0.224±0.0012	0.322±0.0050	14
11-12	13685±119	0.272±0.0015	0.336±0.0053	13
12-13	10669±106	0.316±0.0019	0.373±0.0062	13
13-14	8304±93	0.358±0.0023	0.374±0.0067	13
14-15	6513±82	0.388±0.0027	0.388±0.0078	14
15-17	8923±96	0.423±0.0025	0.414±0.0067	15
17-20	7420±88	0.484±0.0029	0.440±0.0073	14
20-24	4480±68	0.529±0.0040	0.458±0.0095	14
24-30	2617±52	0.570±0.0055	0.483±0.011	14
30-40	1287±36	0.612±0.0085	0.499±0.017	15

Table 10.1: Summary of the J/ψ cross section components in this analysis. The $p_T^{J/\psi}$ bin (1st column), the yield and statistical uncertainty from the fits (2nd column), the total efficiencies and the systematic uncertainties (3rd column), the fitted B fraction and statistical uncertainties (4th column), and the total systematic uncertainties (5th column).

by using an analysis of the same sign muon pairs, which will not show any resonant behaviour in their invariant mass plot. They will be used to check the agreement between the data and the Monte Carlo simulation, in terms of yield and shape of the different distributions. The tag and probe methods will necessarily be more accurate, or the invariant mass fit would be feasible in different $\eta_{J/\psi}$ regions, where

$p_T^{J/\psi}$	$d\sigma/dp_T \cdot$ Br(nb/(GeV/c))		MC input values (nb/(GeV/c))	
(GeV/c)	prompt J/ψ	B-decay J/ψ	prompt J/ψ	B-decay J/ψ
5-6	216±15($stat$)±42($syst$)	52.6±3.6($stat$)±10.1($syst$)	217	50.6
6-7	129±4±18	31.1±1.0±4.3	128	32.9
7-8	73.8±1.6±10.2	22.9±0.5±3.2	73.6	23.8
8-9	44.1±0.8±6.0	15.6±0.3±2.1	43.8	16.4
9-10	26.9±0.5±3.8	11.3±0.2±1.6	27.1	11.5
10-11	16.6±0.3±2.2	7.88±0.14±1.06	16.7	8.09
11-12	11.0±0.2±1.4	5.57±0.10±0.71	10.9	5.88
12-13	6.98±0.14±0.94	4.15±0.08±0.56	7.03	4.23
13-14	4.80±0.10±0.63	2.87±0.06±0.38	4.76	2.98
14-15	3.39±0.08±0.46	2.15±0.05±0.29	3.35	2.23
15-17	2.04±0.04±0.30	1.44±0.03±0.21	2.03	1.48
17-20	0.944±0.019±0.133	0.742±0.015±0.105	0.934	0.765
20-24	0.379±0.010±0.055	0.320±0.008±0.046	0.377	0.325
24-30	0.131±0.004±0.019	0.122±0.004±0.017	0.128	0.125
30-40	0.0348±0.0015±0.0052	0.0346±0.0015±0.0051	0.0333	0.0356

Table 10.2: The prompt and non prompt J/ψ differential cross sections as a function of $p_T^{J/\psi}$ with statistical and systematic uncertainties. The cross section in each $p_T^{J/\psi}$ bin is integrated over the $\eta_{J/\psi}$ range $|\eta_{J/\psi}| < 2.4$. The Monte Carlo input values are listed in the last 2 columns.

the momentum resolution is expected to differ noticeably. It is expected therefore that after few months of LHC operation, the measurement can be performed with a better accuracy than the CDF one.

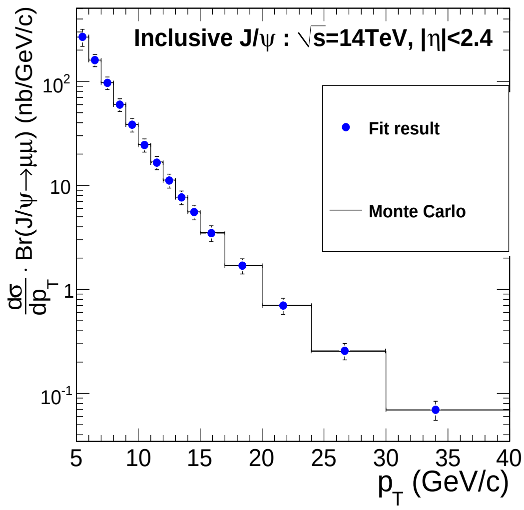

Figure 10.1: The inclusive J/ψ differential cross section, $d\sigma/dp_T \cdot Br(J/\psi \to \mu^+\mu^-)$, as a function of $p_T^{J/\psi}$, integrated over the pseudorapidity range $|\eta_{J/\psi}| < 2.4$, corresponding to an integrated luminosity of 3 pb^{-1}.

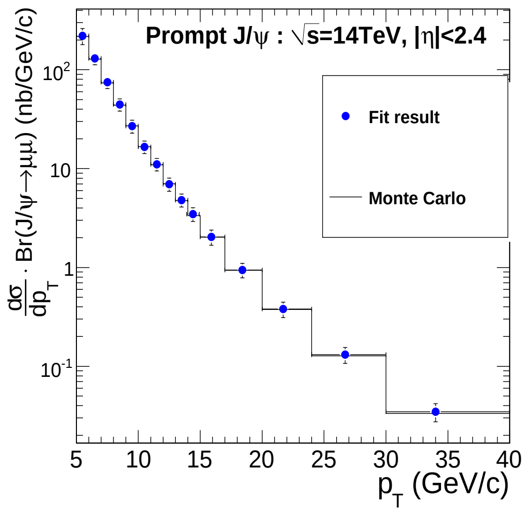

Figure 10.2: The prompt J/ψ differential cross-section as a function of $p_T^{J/\psi}$, integrated over the pseudorapidity range $|\eta_{J/\psi}| < 2.4$, corresponding to an integrated luminosity of 3 pb^{-1}.

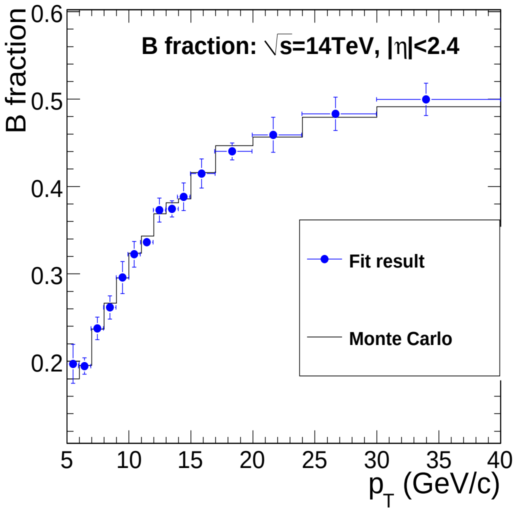

Figure 10.3: The fitted fraction of J/ψ's from B-hadron decays, integrated over the pseudorapidity range $|\eta_{J/\psi}| < 2.4$, corresponding to an integrated luminosity of 3 pb^{-1}, as a function of $p_T^{J/\psi}$.

Chapter 11

Conclusions

In this thesis, the author describes a feasibility study for measuring the J/ψ production cross section in the CMS experiment using $J/\psi \to \mu^+\mu^-$ decay mode.

The measurement is able to be performed with the first data collected by the CMS detector, i.e. an integral luminosity of $3\,\mathrm{pb}^{-1}$. The differential cross sections are determined as functions of the J/ψ transverse momentum, $p_T^{J/\psi}$, integrated over the pseudorapidity range $|\eta_{J/\psi}| < 2.4$. We have shown how to measure the inclusive J/ψ cross section, as well as the prompt and non-prompt components separately, by making use of the large B-hadron lifetime. The most important systematic uncertainties to the measurement were addressed.

The uncertainty in the result is dominated by the systematics, even with the small integrated luminosity that have been considered. Some of the systematics will, of course, benefit from the larger data set that will be collected with higher integrated luminosity. For instance, the tag and probe methods will necessarily be more accurate, or the invariant mass fit would be feasible in different $\eta_{J/\psi}$ regions, where the momentum resolution is expected to differ noticeably. The uncertainties in the background level will be checked in data directly, by using an analysis of the same sign muon pairs, which will not show any resonant behavior in their invariant mass plot. They will be used to check the agreement between the data and the

Monte Carlo simulation, in terms of yield and shape of the different distributions. In the case of the prompt J/ψ measurement, a better alignment and a tighter cut on the decay muons of the J/ψ could help to better disentangle the B-hadron component and reject the non-J/ψ background, respectively.

In the future, with more data available, it will be possible to directly measure the polarization of prompt J/ψ, thus decreasing the cross section uncertainty and may lead to important new insight into the production of charmonium.

By the end of the next year, with an integrated luminosity of $\sim$200 pb^{-1}, the J/ψ differential cross section measurement are expected up to a transverse momentum about 100 GeV/c and possibly beyond. About 5 million J/ψ signals might be collected at that moment and the detector could be much better understood. Therefore, the separation of J/ψ from $\chi_c s$ feeddown should become possible and the measurements mentioned above will become more precise.

During the future high luminosity running, the J/ψ trigger will longer available and we have to increase of the thresholds of relevant single and double muon triggers. This will further expand the range of reachable transverse momenta and allow further tests of the production mechanisms.

Appendix

A Acronyms and abbreviations

ALICE	A Large Ion Collider Experiment
AOD	Analysis Object Data
APE	Alignment Position Error
ATLAS	A Toroidal LHC ApparatuS
BES	Beijing Spectrometer
CSC	Cathode Strip Chamber
CDF	Collider Detector at Fermilab
CEM	Color Evaporation Model
CERN	Conseil Européen pour la Recherche Nucléaire
c.m.	center-of-momentum
CMS	Compact Muon Solenoid
CMSSW	CMS software framework
CEM	Colour Evaporation Model
CLEO	CLEO(patra) or Cornell's Largest Experimental Object (or Operation or Organization)
COM	Colour Octet Mechanism
CSA07	Computing Software and Analysis challenge of 2007
CSA08	Computing Software and Analysis challenge of 2008

CSM	Colour Singlet Model
CTF	Combinatorial Track Finder
DESY	Deutsches Elektronen-Synchrotron
DT	Drift Tube
EB	ECAL Barrel
EDM	Event Data Model
EE	ECAL Endcap
EGEE	Enabling Grids for E-scienc
ES	Preshower detector
ECAL	Electromagnetic Calorimeter
FNAL	Fermi National Accelerator Laboratory (Fermilab)
GT	the Global Trigger
HERA	Hadron Elektron Ring Anlage (Hadron Electron Ring Accelerator)
HCAL	Hadron Calorimeter
HB	HCAL barrel
HE	HCAL endcaps
HF	HCAL forward
HLT	Higher Level Trigger
HO	Outer barrel Hadron calorimeter
LAS	Laser Alignment System
LCG	LHC Computing Grid
LEP	Large Electron - Positron (storage ring)
LHC	Large Hadron Collider
LHCb	LHC-beauty
LHCf	LHC-forward
LINAC	A linear accelerator at CERN
LO	Leading order
MB	Muon Barrel

MC	Monte Carlo
ME	Muon Endcaps
NLO	Next-to-Leading Order
NNLO	Next-to-Next-to-Leading-Order
NRQCD	Non Relativistic Quantum ChromoDynamics
NuSea	Nucleonic Sea experiment
PDF	Parton Distribution Functions
PDG	Particle Data Group
pQCD	perturbative Quantum ChromoDynamics
POG	Physics Object Groups
PSB	Proton Synchrotron Booster
QCD	Quantum ChromoDynamics
QED	Quantum ElectroDynamics
QWG	Quarkonium Working Group
RPC	Resistive Plate Chamber
SM	Standard Model physics
SPS	Super Proton Synchrotron
SST	Silicon Strip Tracker
SUSY	Supersymmetric partner particle
TIB	Tracker Inner Barrel
TID	Tracker Inner Disks
TOB	Tracker Outer Barrel
TEC	Tracker End Caps
TOTEM	Total Cross Section, Elastic Scattering and Diffraction Dissociation
TriDAS	CMS Trigger and Data Acquisition system
TSG	Trigger Study Group
VPT	Vacuum Photo Triodes

B Tables of systematic uncertainties

Tables 11.1 to 11.8 contain the detailed systematic uncertainties of different sources in bins of $p_T^{J/\psi}$.

MC statistics	
$p_T^{J/\psi}$ (GeV/c)	$\Delta\sigma/\sigma$ (%)
5-6	±1.7
6-7	±0.8
7-8	±0.63
8-9	±0.55
9-10	±0.53
10-11	±0.53
11-12	±0.54
12-13	±0.59
13-14	±0.64
14-15	±0.70
15-17	±0.57
17-20	±0.60
20-24	±0.76
24-30	±0.97
30-40	±1.4

Table 11.1: Systematic uncertainties from MC statistics.

J/ψ **polarization**		
$p_T^{J/\psi}$ (GeV/c)	$\Delta\sigma/\sigma$(+)(%)	$\Delta\sigma/\sigma$(-)(%)
5-6	+2.2	-2.4
6-7	+2.0	-2.2
7-8	+1.8	-1.9
8-9	+1.8	-1.9
9-10	+2.1	-2.4
10-11	+2.1	-2.4
11-12	+2.0	-2.3
12-13	+3.1	-3.4
13-14	+3.0	-3.3
14-15	+2.9	-3.2
15-17	+5.7	-7.0
17-20	+5.2	-6.4
20-24	+4.8	-5.8
24-30	+4.3	-5.2
30-40	+3.3	-4.0

Table 11.2: Systematic uncertainties from J/ψ polarization.

J/ψ **pT spectrum**	
$p_T^{J/\psi}$ (GeV/c)	$\Delta\sigma/\sigma$ (%)
5-6	-10
6-7	-3.3
7-8	-1.9
8-9	-1.4
9-10	-1.0
10-11	-0.77
11-12	-0.57
12-13	-0.45
13-14	-0.23
14-15	-0.20
15-17	-0.10
17-20	-0.73
20-24	-0.34
24-30	-0.48
30-40	-2.3

Table 11.3: Systematic uncertainties from $p_T^{J/\psi}$ binning.

Mass fit function	
$p_T^{J/\psi}$ (GeV/c)	$\Delta\sigma/\sigma$ (%)
5-6	+3.6
6-7	+1.5
7-8	+1.7
8-9	+1.6
9-10	+1.4
10-11	+1.4
11-12	+1.3
12-13	+1.8
13-14	+2.1
14-15	+1.7
15-17	+1.6
17-20	+1.0
20-24	+1.9
24-30	+2.7
30-40	+6.3

Table 11.4: Systematic uncertainties from mass fit function.

Resolution model	
$p_T^{J/\psi}$ (GeV/c)	$\Delta\sigma/\sigma$ (%)
5-6	-1.0
6-7	+1.0
7-8	+0.4
8-9	+0.8
9-10	+0.7
10-11	-0.9
11-12	-0.3
12-13	-0.2
13-14	-0.3
14-15	-1.8
15-17	-1.9
17-20	+0.2
20-24	-1.9
24-30	+0.4
30-40	+0.4

Table 11.5: Systematic uncertainties from the ℓ_{xy} resolution model.

B-decay lifetime model	
$p_T^{J/\psi}$ (GeV/c)	$\Delta\sigma/\sigma$ (%)
5-6	+0.019
6-7	-0.0054
7-8	+0.0019
8-9	-0.022
9-10	-0.025
10-11	-0.022
11-12	-0.0066
12-13	-0.015
13-14	-0.0088
14-15	-0.021
15-17	-0.019
17-20	-0.016
20-24	-0.0040
24-30	-0.015
30-40	-0.011

Table 11.6: Systematic uncertainties from B-decay lifetime function.

Misalignment	
$p_T^{J/\psi}$ (GeV/c)	$\Delta\sigma/\sigma$ (%)
5-6	-6.9
6-7	-2.4
7-8	-4.3
8-9	+3.8
9-10	+5.6
10-11	+4.2
11-12	+0.38
12-13	+3.2
13-14	+1.7
14-15	-2.6
15-17	+2.7
17-20	-1.4
20-24	+2.6
24-30	+3.1
30-40	-1.4

Table 11.7: Systematic uncertainties from misalignment.

Background	
$p_T^{J/\psi}$ (GeV/c)	$\Delta\sigma/\sigma$ (%)
5-6	-3.0
6-7	-1.3
7-8	-1.4
8-9	-1.5
9-10	-1.1
10-11	-0.4
11-12	-0.2
12-13	-0.2
13-14	-0.2
14-15	-0.2
15-17	+0.8
17-20	+0.8
20-24	+0.1
24-30	+1.0
30-40	-0.4

Table 11.8: Systematic uncertainties from background.

C Fit results of pseudo-proper decay length for all bins of $\mathbf{p_T^{J/\psi}}$ (I)

In Figs. 11.1 to 11.8 the results of the unbinned maximum likelihood fit are displayed for each bin of $p_T^{J/\psi}$. We used a double Gaussian plus a double-sided exponential function as resolution function.

Each graphs displays the analysis data (dots), the total fitted function (dark (blue) solid line), prompt J/ψ contribution (dark (red) dashed line), non-prompt J/ψ contribution (light (green) dashed line) and non-J/ψ background (dotted (purple) line).

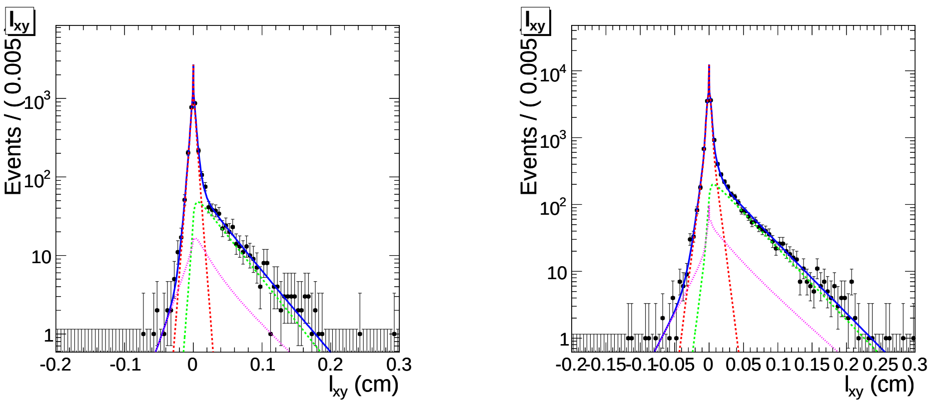

Figure 11.1: Pseudo-proper decay length fitting in the range of 5 GeV/c $< p_T^{J/\psi} <$ 6 GeV/c (left) and 6 GeV/c$< p_T^{J/\psi} <$ 7 GeV/c (right).

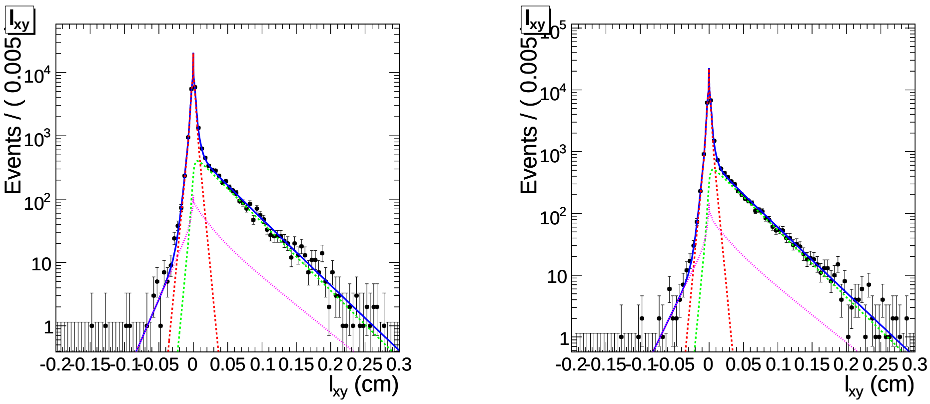

Figure 11.2: Pseudo-proper decay length fitting in the range of 7 GeV/c < $p_T^{J/\psi}$ < 8G eV/c (left) and 8 GeV/c < $p_T^{J/\psi}$ < 9 GeV/c (right).

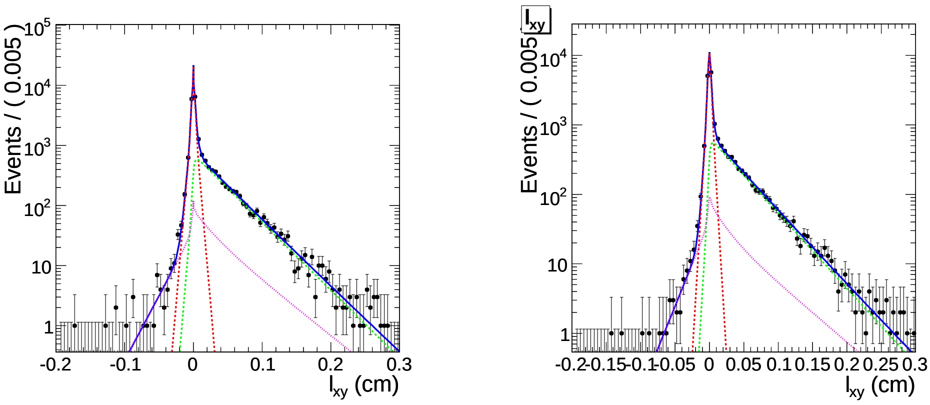

Figure 11.3: Pseudo-proper decay length fitting in the range of 9 GeV/c < $p_T^{J/\psi}$ < 10 GeV/c (left) and 10 GeV/c < $p_T^{J/\psi}$ < 11 GeV/c (right).

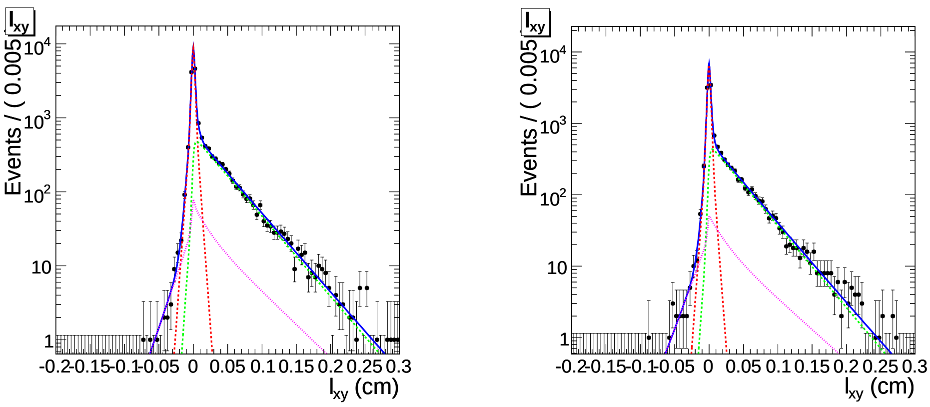

Figure 11.4: Pseudo-proper decay length fitting in the range of 11 GeV/c < $p_T^{J/\psi}$ < 12 GeV/c (left) and 12 GeV/c < $p_T^{J/\psi}$ < 13 GeV/c (right).

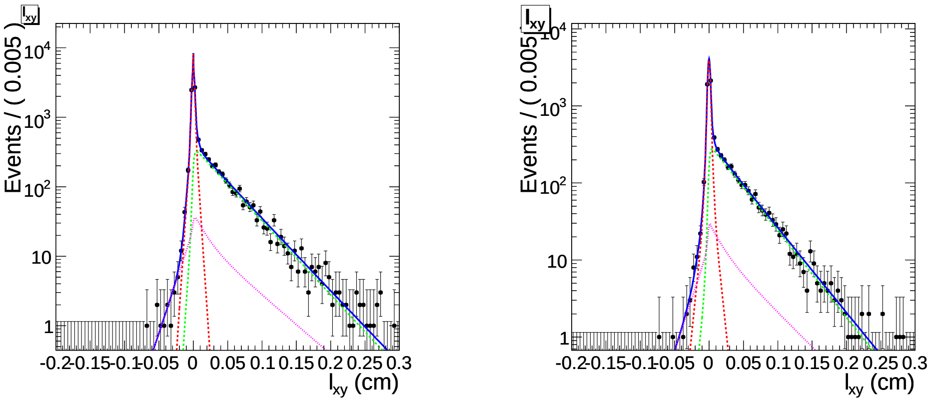

Figure 11.5: Pseudo-proper decay length fitting in the range of 13 GeV/c < $p_T^{J/\psi}$ < 14 GeV/c (left) and 14 GeV/c < $p_T^{J/\psi}$ < 15 GeV/c (right).

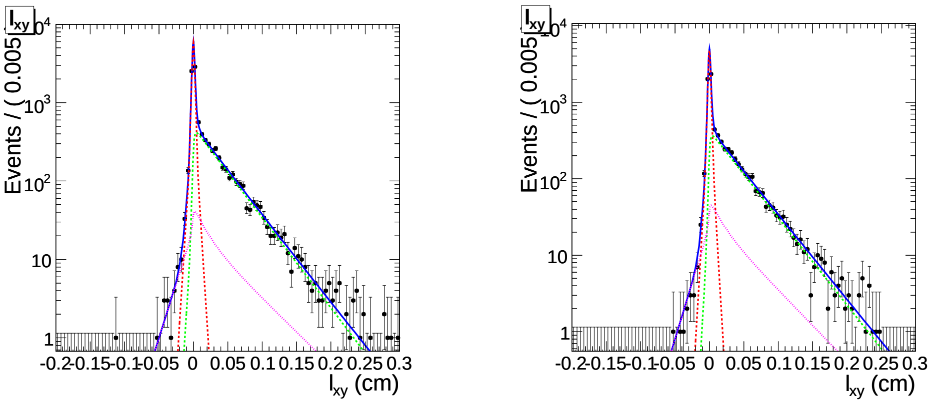

Figure 11.6: Pseudo-proper decay length fitting in the range of 15 GeV/c < $p_T^{J/\psi}$ < 17 GeV/c (left) and 17 GeV/c < $p_T^{J/\psi}$ < 20 GeV/c (right).

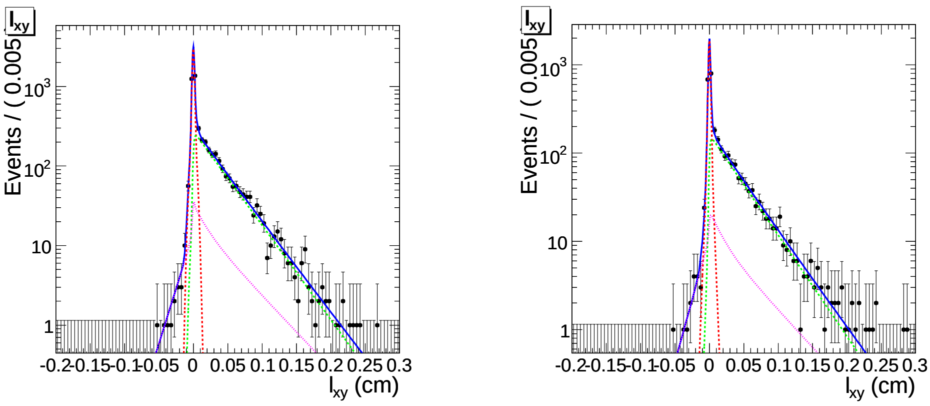

Figure 11.7: Pseudo-proper decay length fitting in the range of 20 GeV/c < $p_T^{J/\psi}$ < 24 GeV/c (left) and 24 GeV/c < $p_T^{J/\psi}$ < 30 GeV/c (right).

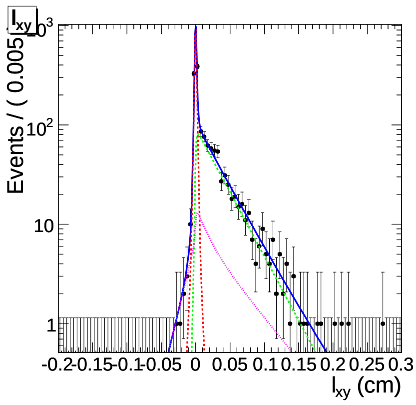

Figure 11.8: Pseudo-proper decay length fitting in the range of 30 GeV/c $< p_T^{J/\psi} <$ 40 GeV/c.

D Fit results of pseudo-proper decay length for all bins of $\mathbf{p_T^{J/\psi}}$ (II)

In Figs. 11.9 to 11.16 the results of the unbinned maximum likelihood fit are displayed for each bin of $p_T^{J/\psi}$. Now we used a triple Gaussian resolution function. The differences between double Gaussian plus exponential and triple Gaussian are considered as the systematic uncertainty from the parametrization of the vertex resolution function.

Each graph displays the analysis data (dots), the total fitted function (dark (blue) solid line), prompt J/ψ contribution (dark (red) dashed line), non-prompt J/ψ contribution (light (green) dashed line) and non-J/ψ background (dotted (purple) line).

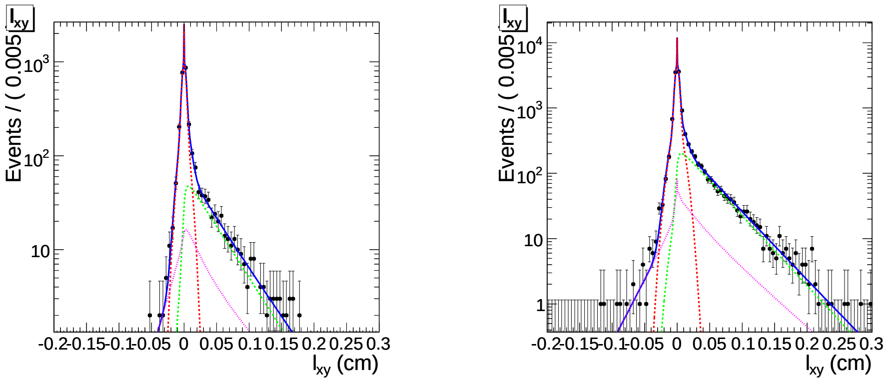

Figure 11.9: Pseudo-proper decay length fitting in the range of 5 GeV/c < $p_T^{J/\psi}$ < 6 GeV/c (left) and 6 GeV/c< $p_T^{J/\psi}$ < 7 GeV/c (right), with triple Gaussian resolution function.

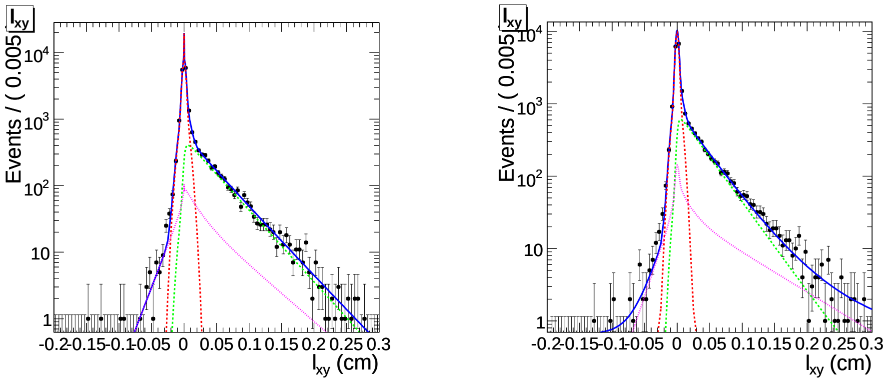

Figure 11.10: Pseudo-proper decay length fitting in the range of 7 GeV/c < $p_T^{J/\psi}$ < 8 GeV/c (left) and 8 GeV/c < $p_T^{J/\psi}$ < 9 GeV/c (right), with triple Gaussian resolution function.

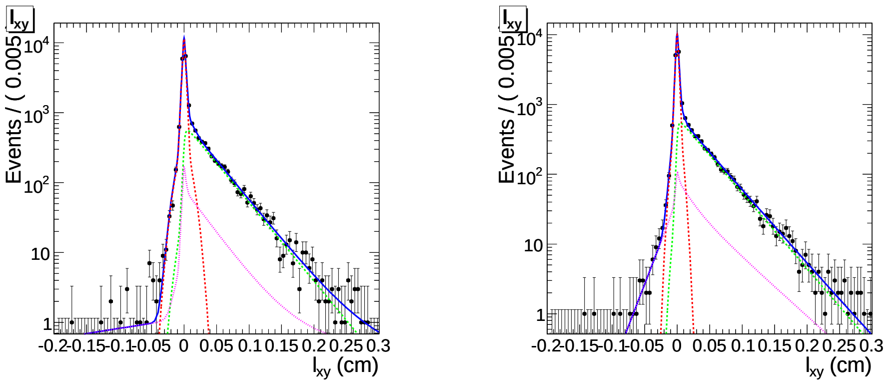

Figure 11.11: Pseudo-proper decay length fitting in the range of 9 GeV/c < $p_T^{J/\psi}$ < 10 GeV/c (left) and 10 GeV/c < $p_T^{J/\psi}$ < 11 GeV/c (right), with triple Gaussian resolution function.

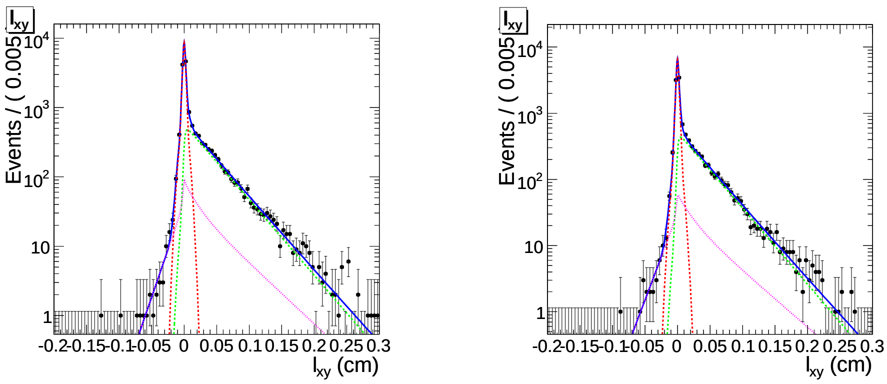

Figure 11.12: Pseudo-proper decay length fitting in the range of 11 GeV/c < $p_T^{J/\psi}$ < 12 GeV/c (left) and 12 GeV/c < $p_T^{J/\psi}$ < 13 GeV/c (right), with triple Gaussian resolution function.

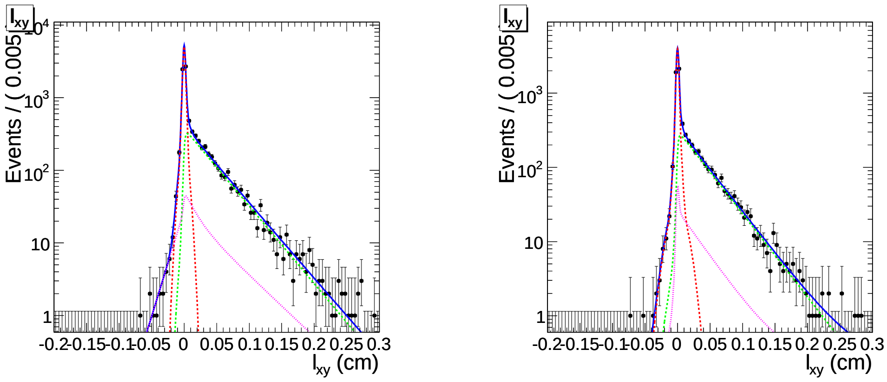

Figure 11.13: Pseudo-proper decay length fitting in the range of 13 GeV/c < $p_T^{J/\psi}$ < 14 GeV/c (left) and 14 GeV/c < $p_T^{J/\psi}$ < 15 GeV/c (right), with triple Gaussian resolution function.

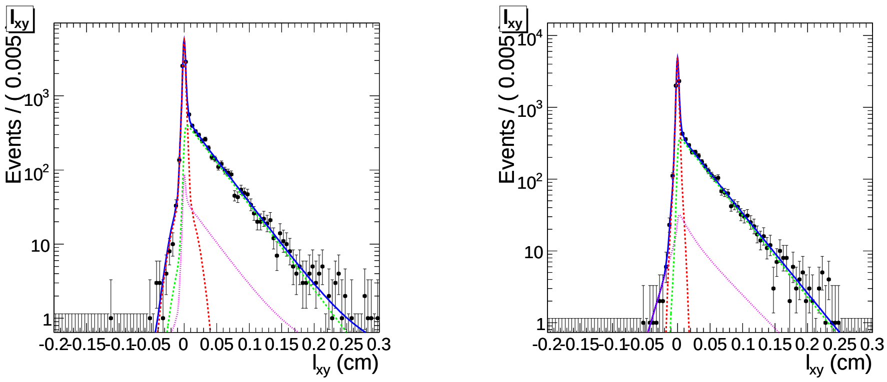

Figure 11.14: Pseudo-proper decay length fitting in the range of 15 GeV/c < $p_T^{J/\psi}$ < 17 GeV/c (left) and 17 GeV/c < $p_T^{J/\psi}$ < 20 GeV/c (right), with triple Gaussian resolution function.

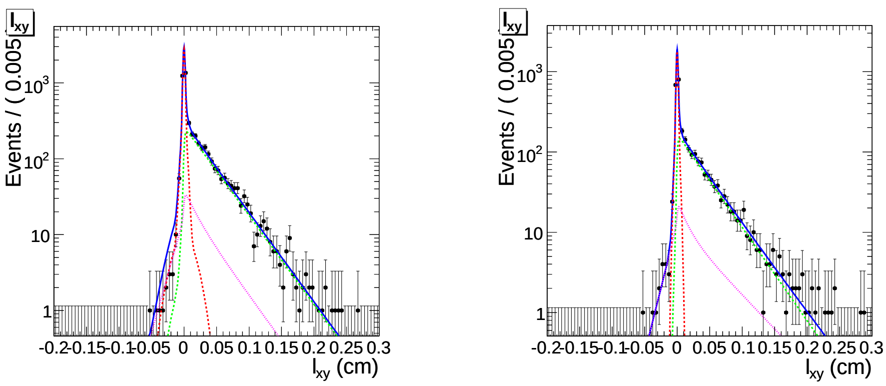

Figure 11.15: Pseudo-proper decay length fitting in the range of 20 GeV/c < $p_T^{J/\psi}$ < 24 GeV/c (left) and 24 GeV/c < $p_T^{J/\psi}$ < 30 GeV/c (right), with triple Gaussian resolution function.

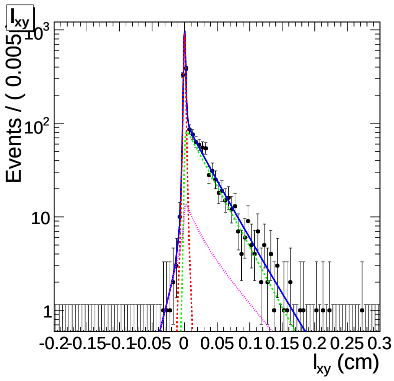

Figure 11.16: Pseudo-proper decay length fitting in the range of 30 GeV/c $< p_T^{J/\psi} <$ 40 GeV/c, with triple Gaussian resolution function.

Bibliography

[1] D. Griffiths. *Introduction to Elementary Particles*, WILLEY-VCH, (Weinheim, 2004).

[2] C. Amsler *et al.*, *Review of Particle Physics*, Phys. Lett. B **667**, (2006) 1.

[3] C. Quigg, *Realizing the Potential of Quarkonium*, FERMILAB-CONF-97-266-T (1997).

[4] I. Hinchliffe, *Quantum Chromodynamics, in Review of Particle Physics*, Phys. Lett. B **592**, (2004).

[5] E. Braaten, T.C. Yuan, *Gluon Fragmentation into Heavy Quarkonium*, Phys. Rev. Lett. **71**, (1993) 1673.

[6] R.K. Ellis, W.J. Stirling , B.R. Webber, *QCD and Collider Physics*, Cambridge University Press, (1996) 347-384.

[7] H. Fritzsch, Phys. Lett. B **67**, (1977) 217.

[8] F. Halzen, Phys. Lett. B **69** (1977) 105.

[9] J.F Amundson, O.J.P. Eboli, E.M. Gregores, F. Halzen, Phys. Lett. B **372** (1996) 127

[10] J.F Amundson et al., Phys. Lett. B **390** (1997) 323.

[11] E. L. Berger and D. Jones, Phys. Rev. D **23**, 1521 (1981).

[12] E. Braaten and T. Yuan, Phys. Rev. Lett. **71**, (1993) 1673.

[13] E. Braaten and T. Yuan, Phys. Rev. D **52**, (1995) 6627.

[14] G. T. Bodwin, E. Braaten and G. P. Lepage, Phys. Rev. D **46**, (1992) 1914.

[15] G. T. Bodwin, E. Braaten and G. P. Lepage, Phys. Rev. D **51**, (1995) 1125; Erratum-ibid D**55**, (1997) 5853.

[16] W.E. Caswell , G.P. Lepage, *Effective Lagrangians for Bound State Problems in QED, QCD, and Other Field Theories*, Phys. Lett. B **167**, 1986) 437.

[17] M. Neubert, Phys. Rept. **245**, (1994) 259.

[18] A. Manohar, *Effective Field Theories*, in "Schladming 1996, Perturbative and nonperturbative aspects of quantum field theory" (1996).

[19] P. Cho and A.K. Leibovich, Phys. Rev. D **53**, (1996) 150.

[20] P. Cho and A.K. Leibovich, Phys. Rev. D **53**, (1996) 6203.

[21] F. Abe *et al.* [CDF Collaboration], Phys. Rev. Lett. **79** (1997) 572.

[22] F. Abe *et al.* [CDF Collaboration], Phys. Rev. Lett. **79** (1997) 578.

[23] CDF Collaboration, Phys. Rev. D **71**, (2005) 032001.

[24] A. A. Affolder *et al.* [CDF Collaboration], Phys. Rev. Lett. **84** (2000) 2094

[25] D. Acosta *et al.* [CDF Collaboration], Phys. Rev. Lett. **88** (2002) 161802.

[26] M. Krämer, Prog. Part. Nucl. Phys. **47**, (2001) 141.

[27] M. Beneke and M. Krämer, Phys. Rev. D **55**, (1997) 5269.

[28] W. Buchmüller and S. H. Tye, Phys. Rev. D **24**, (1981) 132.

[29] E. J. Eichten and C. Quigg, Phys. Rev. D **52**, (1995) 1726.

[30] H. L. Lai *et al.* [CTEQ Collaboration], Eur. Phys. J. C **12**, (2000) 375.

[31] B. A. Kniehl and L. Zwirner, Nucl. Phys. B 621, 337 (2002).

[32] A. Abulencia *et al.* [CDF Collaboration], Phys. Rev. Lett. **99** (2007) 132001.

[33] D0 Collaboration, Preliminary Result, Conference Note 5089-CONF, July 2007.

[34] S. P. Baranov, Phys. Rev. D 66, (2002) 114003 .

[35] T. H. Chang et al. [FNAL E866/NuSea collaboration], Phys. Rev. Lett. 91, (2003) 211801.

[36] C. N. Brown et al. [FNAL E866 Collaboration], Phys. Rev. Lett. 86, (2001) 2529.

[37] J. Campbell, F. Maltoni, F. Tramontano, Phys. Rev. Lett. **98** (2007) 252002.

[38] P. Artoisenet, J. P. Lansberg, F. Maltoni, Phys. Lett. B **653** (2007) 60.

[39] H. Haberzettl , J. P. Lansberg, Phys. Rev. Lett. **100** (2008) 032006.

[40] P. Artoisenet, J. Campbell, J.P. Lansberg, F. Maltoni, F. Tramontano, Phys. Rev. Lett. 101, (2008) 152001.

[41] J. P. Lansberg, 2009 [arXiv.org:hep-ph/0901.4777].

[42] J. P. Lansberg, J. R. Cudell and Yu. L. Kalinovsky, Phys. Lett. B **633** (2006) 301.

[43] N. Brambilla *et al*, CERN Yellow Report, CERN-2005-005, e-Print: hep-ph/0412158.

[44] M. Krämer, Nucl. Phys. B **459** (1996) 3 [hep-ph/9508409].

[45] C. Adloff *et al.* [H1 Collaboration], Eur. Phys. J. C **25** (2002) 25 [hep-ex/0205064].

[46] S. Chekanov *et al.* [ZEUS Collaboration], Eur. Phys. J. C **27** (2003) 173 [hep-ex/0211011].

[47] Homepage of the Quarkonium Working Group, http://www.qwg.to.infn.it/

[48] J. P. Lansberg, Int. J. Mod. Phys. A **21** (2006) 3857.

[49] H. Evans, invited talk in XXIV Physics in Collision", Boston, MA June 28, 2004.

[50] A.C. Kraan, CMS AN-2007/042 and CMS AN-2008/010.

[51] The LHC Study Group, The Large Hadron Collider Conceptual Design, CERN/AC 95-05 (1995).

[52] O. S. Brüning *et al.* LHC Design Report, CERN-2004-003 (2004).

[53] Lyndon Evans and Philip Bryant (editors), LHC Machine, 2008 JINST 3 S08001.

[54] G. Aad *et al.* [The ATLAS Collaboration], 2008 JINST 3 S08003.

[55] S. Chatrchyan *et al.* [The CMS Collaboration], 2008 JINST 3 S08004

[56] K Aamodt *et al.* [The ALICE Collaboration], 2008 JINST 3 S08002

[57] A Augusto Alves Jr *et al.* [The LHCb Collaboration], 2008 JINST 3 S08005

[58] G. Anelli *et al.* [The TOTEM Collaboration], 2008 JINST 3 S08007

[59] CERN Workshop on Standard Model Physics (and more) at the LHC, CERN Yellow Report 2000-004.

[60] The LEP ElectroweakWorking Group, http://lepewwg.web.cern.ch/LEPEWWG/ (May 2007).

[61] M. Spira and P. M. Zerwas, Electroweak symmetry breaking and Higgs physics, CERN-TH/97-379 (1997). hep-ph/9803257.

[62] The CMS Collaboration, Technical Proposal, CERN/LHCC 94-38, LHCC/P1 (1994).

[63] The CMS Collaboration, CMS Technical Design Report Volume 1, CERN/LHCC 2006-001 (2006).

[64] The CMS Collaboration, The Magnet Project: Technical Design Report, CERN/LHCC 97-10, CMS TDR 1 (1997).

[65] The CMS Collaboration, The Tracker Project: Technical Design Report, CERN/LHCC 98-6, CMS TDR 5 (1998).

[66] The CMS Collaboration, Addendum to the CMS Tracker Technical Design Report, CERN/LHCC 2000-016, CMS TDR 5 Addendum 1 (2000).

[67] The CMS Collaboration, The Electromagnetic Calorimeter Project: Technical Design Report, CERN/LHCC 97-33, CMS TDR 4 (1997).

[68] The CMS Collaboration, The Hadronic Calorimeter: Technical Design Report, CERN/LHCC 97-31, CMS TDR 2 (1997).

[69] The CMS Collaboration, The CMS muon project Technical Design Report. CERN/LHCC-97-32, CMS-TDR-003, (1997).

[70] The CMS Collaboration, The TriDAS Project Technical Design Report, Volume 1: The Trigger Systems, CERN/LHCC 2000-038, CMS TDR 6.1 (2000).

[71] The CMS Collaboration, The TriDAS Project Technical Design Report, Volume 2: Data Acquisition and High-Level Trigger, CERN/LHCC 2002- 26, CMS TDR 6.2 (2002).

[72] C.-E. Wulz, "Concept of the First Level Global Trigger for the CMS Experiment at LHC," Nucl. Instr. Meth., A473 , p. 231, 2001.

[73] C. Eck et al., LHC computing Grid Technical Design Report, LCG TDR 1, CERN LHCC 2005/024.

[74] The CMS Collaboration, CMS Computing Technical Design Report. CERN/LHCC-2005-023, 2005. Submitted on 31 May 2005.

[75] CMSSW, CMSSW application framework, http://cmsdoc.cern.ch/cms/cpt/Software/html/General/

[76] R. Brun et al., ROOT, An Object-Oriented Data Analysis Framework, http://root.cern.ch/.

[77] T. Sjöstrand, S. Mrenna, P. Skands, JHEP 0605:026,2006.

[78] The original implementation was done by S. Wolf in 2000, but it was never included officially. In 2005 it was officially integrated by T. Sjöstrand, and in 2006 tuned by M. Bargiotti [83].

[79] T. Sjöstrand and M. van Zijl, Phys. Rev. D **36** (1987) 2019.

[80] T. Sjöstrand and P. Skands, Eur. Phys. J. C **39** (2005) 129.

[81] http://www.phys.ufl.edu/ rfield/ (homepage Rick Field)

[82] P. Bartalini etal, CMS NOTE-2006/067.

[83] M. Bargiotti and V. Vagnoni, LHCb-2007-042.

[84] https://twiki.cern.ch/twiki/bin/view/CMS/MBUETuning.

[85] hltnote) The CMS Collaboration, CMS High Level Trigger, CMS Note 2007/009 (2007).

[86] R. E. Kalman, "A new approach to linear filtering and prediction problems", Transaction of the ASME - Journal of Basic Engineering, vol. 35, 1960.

[87] The Trigger Studies Group, https://twiki.cern.ch/twiki/bin/view/CMS/TriggerStudies

[88] http://lhc-commissioning.web.cern.ch/lhc-commissioning/

[89] Z. Yang and S. Qian, CMS NOTE-2007/017.

[90] R. Frühwirth, Application of Kalman filtering to track and vertex fitting, Nucl. Instrum. Meth. A262 (1987) 444.

[91] T. Speer, K. Prokofiev, R. Fruhwirth, CMS IN-2003/008.

[92] N. Adam *et al.* CMS AN-2007/031.

[93] https://twiki.cern.ch/twiki/bin/view/CMS/MuonPOG

[94] D. Acosta *et al.*, CMS NOTE-2006/060.

[95] https://twiki.cern.ch/twiki/bin/view/CMS/LumiWikiHome.

[96] B. Aubert et al. (BABAR Collaboration), Phys. Rev. D 67, 032002 (2003).

北京大学学位论文原创性声明和使用授权说明

原创性声明

本人郑重声明：所呈交的学位论文，是本人在导师的指导下，独立进行研究工作所取得的成果。除文中已经注明引用的内容外，本论文不含任何其他个人或集体已经发表或撰写过的作品或成果。对本文的研究做出重要贡献的个人和集体，均已在文中以明确方式标明。本声明的法律结果由本人承担。

论文作者签名：　　　　　　日期：　　年　　月　　日

学位论文使用授权说明

（必须装订在提交学校图书馆的印刷本）

本人完全了解北京大学关于收集、保存、使用学位论文的规定，即：

- 按照学校要求提交学位论文的印刷本和电子版本；
- 学校有权保存学位论文的印刷本和电子版，并提供目录检索与阅览服务，在校园网上提供服务；
- 学校可以采用影印、缩印、数字化或其它复制手段保存论文；
- 因某种特殊原因需要延迟发布学位论文电子版，授权学校☐一年/☐两年/☐三年以后，在校园网上全文发布。

（保密论文在解密后遵守此规定）

论文作者签名：　　　　　　导师签名：

日期：　　年　　月　　日